Faculty of Physics, Astronomy and Applied Computer Science of the Jagiellonian University

Galactic magnetized plasma exposed to winds and tidal interactions

Robert Tomasz Drzazga

A thesis written under the supervision of dr hab. Krzysztof Chyży, submitted to the Jagiellonian University for the degree of Doctor of Philosophy

Kraków 2014

To my parents and memory of my grandmother Józefa

Abstract

There is still very little known about the influence of galactic winds and tidal interactions on generation and properties of magnetic fields in galaxies. Three galaxies NGC 2976, IC 10, and M 81 were investigated in this thesis in order to provide more insight into that matter. These objects were further supplemented with the data for five galaxies from the WSRT-SINGS survey, making up a comparison sample. For the purpose of the study, radio polarimetric observations with VLA, Effelsberg, WSRT, and JVLA instruments were performed. For NGC 2976, M 81 and five WSRT-SINGS objects, a novel method of data analysis, the rotation measure (RM) synthesis, was used. A new weighting scheme was proposed for this method which resulted in an improvement of the signal-to-noise ratio in the Faraday depth space.

In the investigated objects a clear influence of galactic winds or tidal interactions on the magnetic field structure can be discerned, in contrast to the comparison sample of galaxies. In particular, in NGC 2976, a southern polarized ridge and the northern polarized extension are signatures of tidally/ram pressure modified magnetic field, generated by large-scale dynamo (possibly CR-driven). The same is indicated by a high regularity of the field (of about 0.46), similar to spiral galaxies, and by the coherent pattern of magnetic field within the optical disk and outside of it.

In a tiny starbursting dwarf IC 10, a huge and highly symmetric synchrotron envelope is discovered at 1.43 GHz. On the largest scales, the magnetic field exhibits a global "X-shape" morphology, with dominating radial component. Such structures are often observed in the edge-on spiral galaxies with high star formation activity. The X-shaped magnetic structure and the radio envelope imply an action of galactic scale winds, pulling out magnetic fields with outflows from massive stars and supernova explosions. Estimations of the scale height of the thick disk and the synchrotron cooling time imply the bulk speed of cosmic rays in the galaxy halo of about 150-300 km s^{-1}. Such values are much larger than the gas escape velocity and indicate the galactic-scale wind. The strong magnetic field in IC 10 (of about 14 μG) is probably generated by a small-scale dynamo only, since the rotation measure data and calculations of the dynamo number do not promote a large-scale dynamo.

M 81 seems to possess a complicated morphology of magnetic field. For some regions in the galaxy, the RM Synthesis data even reveal multiple (or an extended) components in the Faraday spectrum. With the available data, it was not possible to confirm that the morphology of magnetic field in this object is dominated by a bisymmetric dynamo mode. Possibly, the field structure in M 81 could have been modified by tidal interactions with other galaxies of the M 81 group. Galactic winds and tidal interactions are therefore crucial in shaping morphology of magnetic fields in the investigated galaxies.

It is also evident that NGC 2976 and IC 10 are good candidates for magnetization of the intergalactic space. Despite their different linear sizes, they are both able to provide ordered magnetic fields far out of their main disks (up to a distance of about 5 kpc). The plasma ejected by galactic wind from IC 10 and by gravitational interactions from NGC 2976 gives us a precious possibility to study feedback processes expected to be common in the early Universe. This does not pertain to M 81, for which no signatures of pulling out magnetic field have been found.

Contents

1

List of Figures

3

List of Tables

Chapter 1

Introduction

1.1 Magnetic fields in galaxies

It is a well-established fact that space is filled with magnetic fields of various scale and strength (Parker 2007). Particularly on galactic scales, magnetic fields can play a key role in a number of astrophysical processes, e.g. providing cosmic-ray confinement, taking part in the galactic disk pressure balance (Beck 2007), and modulating the local gas dynamics through magneto-Jeans instabilities (Kim *et al.* 2002). Understanding the effects of magnetic fields in the interstellar medium (ISM) requires a good knowledge of origin, structure, and evolution of magnetic fields in various types of galaxies.

In the spirals, observations of polarized radio emission and Faraday rotation reveal strong (of about 5μG), large-scale magnetic fields (Beck 2005), usually aligned with density waves, even if perturbed by weak gravitational interactions (cf. Fig. 1.1, left side). In order to explain the origin of such regular magnetic structures, a theory of large-scale dynamo has been proposed (e.g. Widrow 2002), which assumes amplification of magnetic fields by helical turbulent motions (α – effect) as well as galactic differential rotation (ω – effect), see Fig. 1.2 and its caption. Recent observations indicate that even in galaxies of early Hubble morphology, devoid of density waves, large-scale magnetic fields are readily generated (Chyży & Buta 2008, see Fig.1.1, right side).

In the low-mass dwarf objects, the conditions and efficiency of magnetic field generation process are still not too well understood (see, e.g. Chyży *et al.* 2011). In such galaxies, the influence of magnetic fields on the ISM is expected to be of even more importance, because of their smaller gravitational potential and possibility of gas escaping via galactic winds. On the other hand, the dwarf galaxies are more weakly rotating with more disorderly motions, providing for a weak ω – effect. Therefore, there could be no large-scale dynamo at work in some dwarfs at all, as they are below the dynamo efficiency threshold (Gressel *et al.* 2008). In such objects, random magnetic fields could be produced by a small-scale dynamo action (Zeldovich *et al.* 1990, Widrow 2002).

Only several dwarf galaxies have been observed to date with respect to magnetic fields for which the dynamo concepts could be tested. As it could be expected, in the very small and low-mass dwarfs IC 10 and NGC 6822 (linear size of 1 and 2 kpc, respectively) no large-scale magnetic fields have been detected to date (Chyży *et al.* 2003, Chyży *et al.* 2011, Heesen *et al.* 2011), indicating that these objects are below the efficiency threshold of the large-scale dynamo. In more massive and larger dwarfs NGC 4449 as well as in the Large Magellanic Cloud (of 7 and 10 kpc size, respectively), regular magnetic fields (of 8 and 1 μG, respectively) with fragments of some large-scale spiral structure, as evident signatures of large-scale $\alpha - \omega$
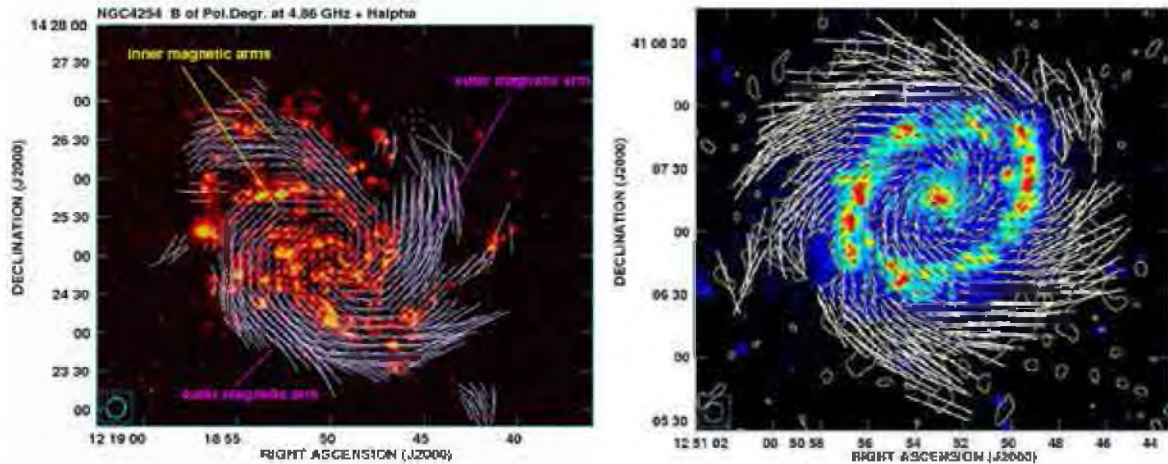
Figure 1.1: Left: Actual (Faraday-free) structure of magnetic field vectors in NGC 4254 obtained from the combined VLA and single-dish (Effelsberg) polarized data at 8.46 GHz and 4.86 GHz. The lengths of vectors are proportional to the degree of polarization at 4.86 GHz. The regions with inner and outer magnetic arms are designated. Overlaid (in colours) is the Hα image (from Knapen *et al.* 2004). Right: The polarized intensity contour map of NGC 4736 at 8.46 GHz and 8.6" × 8.6" resolution with observed magnetic field vectors of the polarization degree overlaid upon the Hα image (from Knapen *et al.* 2003). The contours are at 21, 42, 84 µJy/beam area. The vector of 10" corresponds to the polarization degree of 25%. Both images and captions were taken from Chyży (2008) and Chyży & Buta (2008), respectively.

dynamo, were observed (Chyży *et al.* 2000, Gaensler *et al.* 2005). Some regular fields (of about 1 µG) were also found in the Small Magellanic Cloud (of 6 kpc size), but in this case, the field structure did not resemble any large-scale dynamo (Mao *et al.* 2008). However, as these three large dwarfs show distinct signs of strong tidal interactions, it is not clear whether and how gravitational interactions influenced the set-up of the large-scale dynamo process and which conditions are appropriate for an efficient dynamo to occur in dwarfs.

1.2 Galactic winds and tidal interactions – the thesis aims

One of the crucial problems of the present-day astrophysics is to understand the link between gas and magnetic field in galaxies. The natural phenomena where such effects can be directly observed are galactic winds and tidal interactions. In this thesis, I explore to which degree these processes can modify structures of galactic magnetic fields and to which degree they take part in their generation. Furthermore, it is also suspected that galactic winds and tidal interactions are crucial agents responsible for magnetization of the inter galactic medium (IGM; e.g. Chyży *et al.* 2011, Drzazga *et al.* 2011). Here, I am also going to verify these statements. As it was presented above, magnetic fields in dwarf galaxies are still little explored, mainly due to the small sample of the objects of this type observed up to date. In this thesis, I will increase a number of dwarfs for which magnetic field properties, including field strength and its structure, have been determined. The special attention will be paid to the problem of efficiency of generation of large-scale magnetic fields in such a type of galaxies.

Galactic winds are most readily observed in the edge-on galaxies. There are two basic mechanisms responsible for their production: massive stars (through star winds and supernovae) residing in the galactic disk and active galactic nuclei (e.g. Veilleux *et al.* 2005). It is

9
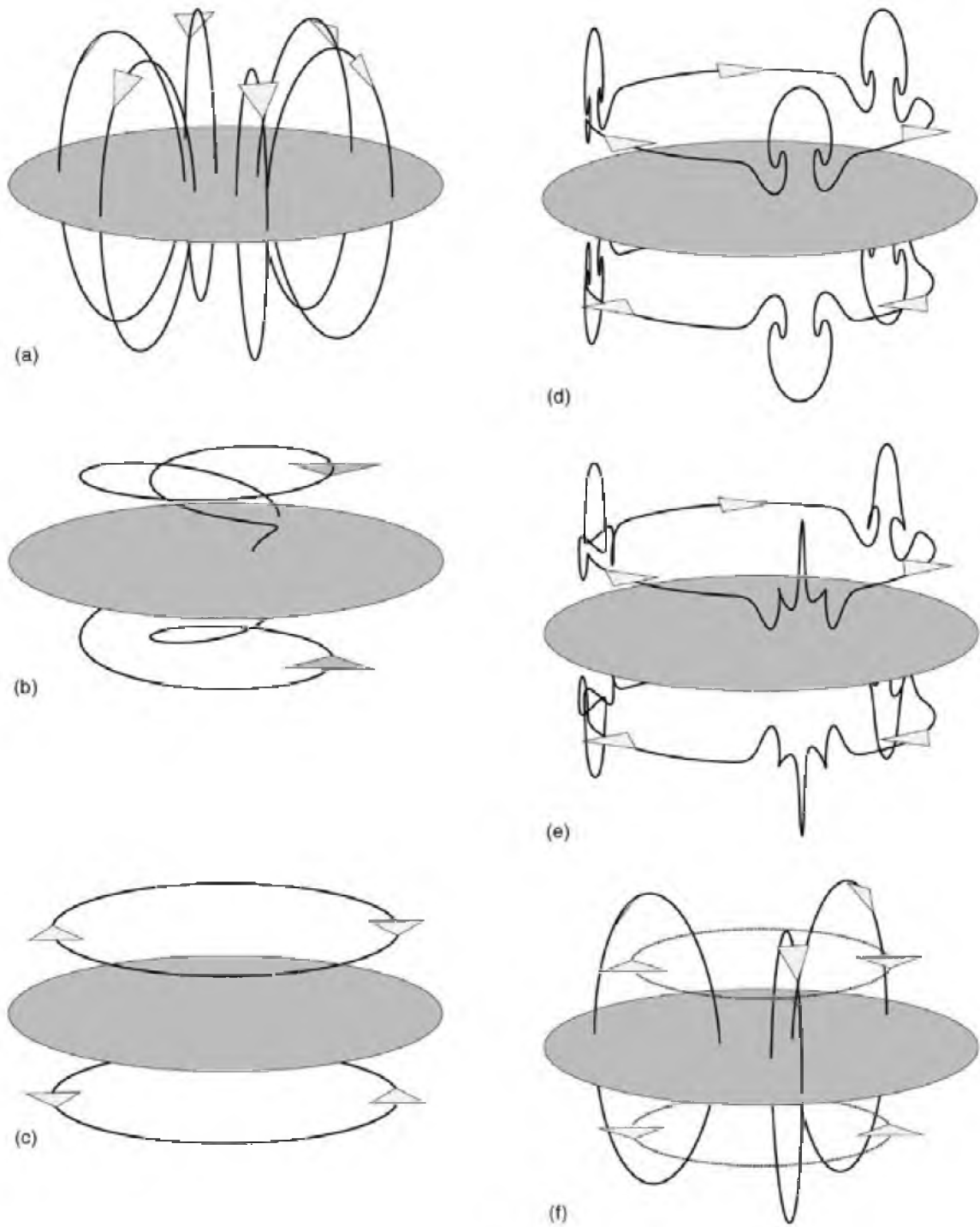
Figure 1.2: Sequence of events illustrating an axisymmetric, odd-parity (A0) $\alpha - \omega$ dynamo: (a) dipole-like poloidal (A0) field; (b) single field line from (a) after it has been stretched by differential rotation; (c) toroidal component from (b) assuming that turbulent diffusion and/or reconnection have decoupled field in the upper and lower hemispheres; (d) plumes created from the toroidal field by cyclonic events; (e) field loops from (d) twisted by the Coriolis effect; (f) poloidal loops created from those shown in (e). The figure and its caption were taken from Widrow (2002).

10

believed that the galactic-scale winds are important for understanding the observed X-shape magnetic fields in galaxies (Beck 2009; Soida *et al.* 2011). This is apparently supported by numerical simulations involving dynamo models with galactic winds (Brandenburg *et al.* 1993; Moss *et al.* 2010) in reproducing the observations. Similarly as winds, also tidal interactions influence structures of magnetic field within galaxies. In the merging objects, like the Antennae, the gas flows resulting from tidal forces leave clear imprints on the magnetic field structure, particularly well visible in the magnetic field stretched along the tidal tail. There are only some small fragments of the original field structure left – a relic of the magnetic spiral that survived the collision (Chyży & Beck 2004). Signatures of tidal interactions in magnetic field morphologies are also found in galaxies which are in less advanced stages of interactions. For instance, in NGC 2207, there is an outflow of magnetized plasma visible in its southern part (Drzazga *et al.* 2011). Perhaps the interactions are also responsible for the unusual, bisymmetric field morphology in M 81 (Moss *et al.* 1993).

For the purpose of the investigations presented in this thesis, I carefully selected three galaxies: NGC 2976, IC 10 and M 81. NGC 2976 is a galaxy of dwarfish pure-disk morphology, located within a galaxy group. The object was not strongly disturbed for a long time, which along with its dynamical simplicity makes it a suitable laboratory for studying efficiency of large-scale dynamo generation process and evolution of magnetic field exposed to gravitational interactions in the past. IC 10 is a low-mass dwarf known to be in a phase of intensive star formation, thus making an excellent candidate to possess magnetized galactic winds which could influence its radio emission and magnetic field; and finally, M 81 – subject to tidal interactions within a group of galaxies, which imprints are found in the morphology of HI surrounding the object, providing an excellent arena for investigation of influence of gravitational interactions on morphology of magnetic field. Furthermore, I supplemented the sample with five comparison spiral galaxies from the WSRT-SINGS survey, possessing a similar type and inclination angle as NGC 2976.

In the next section, an overview of observational methods used in this thesis is given. Then, in chapter 2 I present the observations and results obtained for NGC 2976 and five WSRT-SINGS galaxies. Chapter 3 includes an analysis of the data for the starbursting dwarf IC 10. Chapter 4 reports investigations of the spiral galaxy M 81. In the last chapter, the summary as well as prospects for further study are presented.

1.3   Radio polarimetric methods of observations of magnetic fields in galaxies

The crucial observables describing magnetic field is its strength and structure. Methods of their determination are given below.

1.3.1   Derivation of magnetic field strengths

The strengths of the total B_{tot} and ordered B_{ord} magnetic field are calculated from the nonthermal (synchrotron) intensity I_n and nonthermal degree of linear polarization P_{nth}. When one assumes an equipartition between the energy densities of magnetic field and cosmic rays, the total magnetic field is given by (Beck & Krause 2005):

$$B_{tot} = \left[\frac{4\pi(2\alpha_n + 1)(K_0 + 1)I_n E_p^{1-2\alpha_n}\left(\frac{\nu}{2c_1}\right)^{\alpha_n}}{(2\alpha_n - 1)c_2\alpha_n L c_3} \right]^{\frac{1}{\alpha_n+3}} \tag{1.1}$$

where α_n is nonthermal spectral index, K_0 is the ratio of proton-to-electron number densities, L is the path length through the synchrotron-emitting medium, E_p is the rest energy of the proton, and

$$c_1 = \frac{3e}{4\pi m_e^3 c^5} = 6.2648 \times 10^{18} \mathrm{erg}^{-2}\mathrm{s}^{-1}\mathrm{G}^{-1}, \tag{1.2}$$

$$c_2(\alpha_n) = \frac{1}{4}c_3 \frac{(\alpha_n + \frac{5}{3})}{(\alpha_n + 1)} \Gamma\left[\frac{(3\alpha_n + 1)}{6}\right] \times \Gamma\left[\frac{(3\alpha_n + 5)}{6}\right]. \tag{1.3}$$

The c_2 and c_3 constants are geometrical corrections that depend on the magnetic field orientation. In the case where the field is totally regular and has a constant inclination $incl$ with respect to the sky plane, $c_3 = (\cos incl)^{\alpha_n + 1}$. Alternatively, for a completely turbulent field, $c_3 = (2/3)^{(\alpha_n+1)/2}$, while in the case where synchrotron intensity is averaged over a large volume, such as an entire galaxy, the value of c_3 is replaced by its average over all occurring values of inclination angles.

The strength of the mean ordered magnetic field in the galaxy can be obtained from the estimated nonthermal degree of polarization in the following way (Segalovitz *et al.* 1976):

$$P_{nth} = \left(\frac{3\gamma + 3}{3\gamma + 7}\right) \times \left[1 + \frac{(1-q)\pi^{\frac{1}{2}}\Gamma[(\gamma+5)/4]}{2q\Gamma[(\gamma+7)/4]F(incl)}\right]^{-1}, \tag{1.4}$$

where

$$F(incl) = \frac{1}{2\pi}\int_0^{2\pi}(1 - \sin^2 incl \sin^2\theta)^{(\gamma+1)/4}\mathrm{d}\theta, \tag{1.5}$$

$q^{1/(1+\alpha_n)} = B_{ord}/B_{ran}$, θ is the azimuthal angle, and B_{ran} is the random component of the magnetic field.

1.3.2 "Classic" radio polarimetry

Polarimetry at radio wavelengths is a powerful tool enabling studies of structure of ordered and regular magnetic fields in galaxies (e.g. Beck & Wielebinski 2013). An origin of such a field, if it is dynamo-generated or is just an effect of ordered gas motions, can only be distinguished basing on information concerning the so-called rotation measure (RM) in the object under investigation, which is a slope of straight line fitted to the relation of position angle of polarization vector (PA) versus wavelength squared (λ^2). There are in fact two methods of obtaining this observable, both described below.

Classic method of obtaining of rotation measure distribution consists in taking polarization angle maps at (at least) two separate frequencies and using the following formulae:

$$RM = \frac{PA_1 - PA_2}{\lambda_1^2 - \lambda_2^2} \tag{1.6}$$

In practice, two wavelengths are usually used in studies of galaxies, most commonly 3 and 6 cm (e.g. Chyży *et al.* 2000, Chyży *et al.* 2007b, Soida *et al.* 2011). Note that in order to properly determine the RM at least three frequencies are needed, due to $n\pi$ ambiguity problem. Moreover, in the classic method all information from the whole line of sight is summed up, which makes interpretation of RM distribution maps much difficult. These problems are overcome (at least partly) by the new method of analysis of polarimetric data - the rotation measure synthesis.
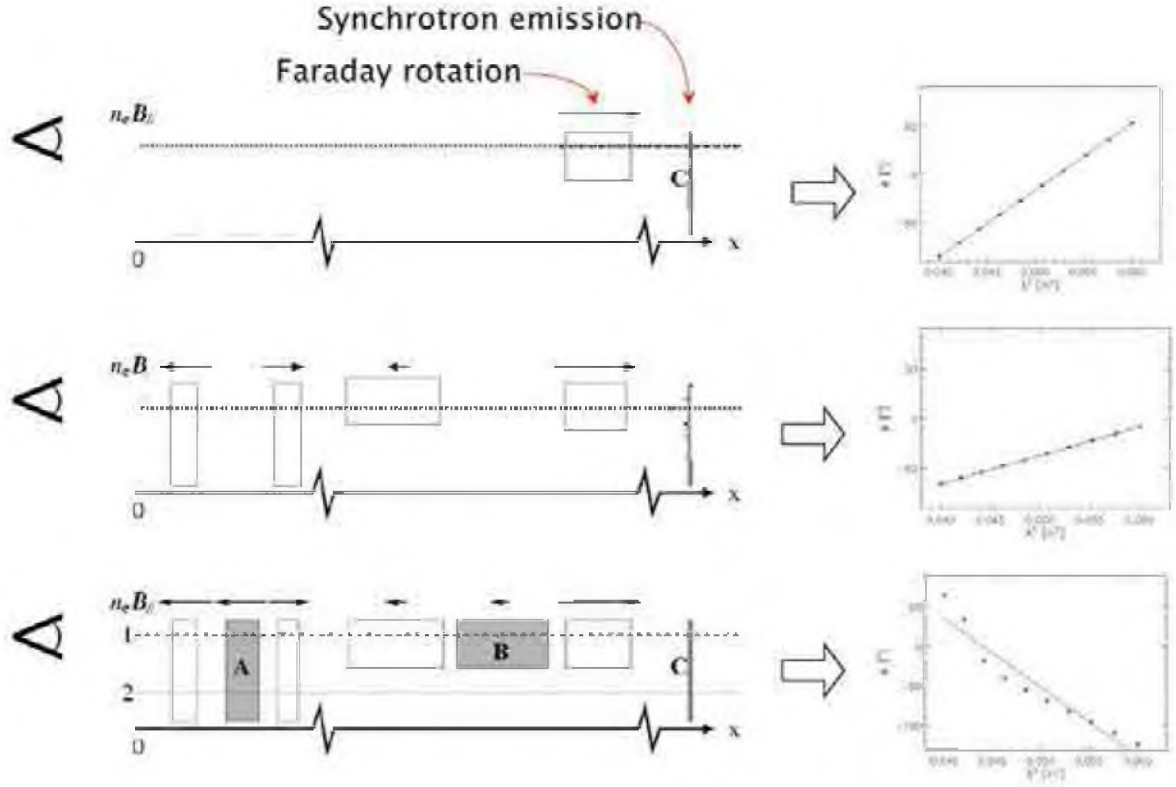
Figure 1.3: Sketch representing comparison of the RM Synthesis technique (left images) and the traditional method of obtaining of information about rotation measure (right images). On the left, the white boxes represent the so-called Faraday screens – objects along line of sight which are responsible only for rotation of polarized electromagnetic waves (Faraday rotation). On the image, x-axis denotes a physical distance to a given source; the arrows above the sources represent the product of density of thermal electrons and strength of magnetic field component parallel to the line of sight, which along with the spatial extension of the source determine the magnitude of rotation measure; the observer is marked on the left. The black boxes represent synchrotron emission with (sources denoted as A and B) and without (source C) simultaneous Faraday rotation (extended and narrow boxes, respectively). The plots on the right show the traditional method of obtaining RM value for the physical situations shown on the left. The top and middle pictures represent the case where there is just a single synchrotron emitting source (without internal Faraday rotation) and between it and the observer some Faraday screens are present – in such a case, the fitted relation can be directly interpreted as an RM value. The bottom picture shows a more realistic situation where synchrotron-emitting and internally rotating sources are mixed with rotating-only objects – the classical method gives us here only information about non-linearity of PA vs. λ^2 relation. Thus, the slope obtained in this way cannot be regarded as a reliable value of rotation measure. Such a physical situation can only be properly recognized (and interpreted) using the RM Synthesis method – it enables us to recover the distribution of emitting and rotating objects along the line of sight. Source: Marike Haverkorn (ASTRON, Netherlands), http://www.astron.nl/sites/astron.nl/
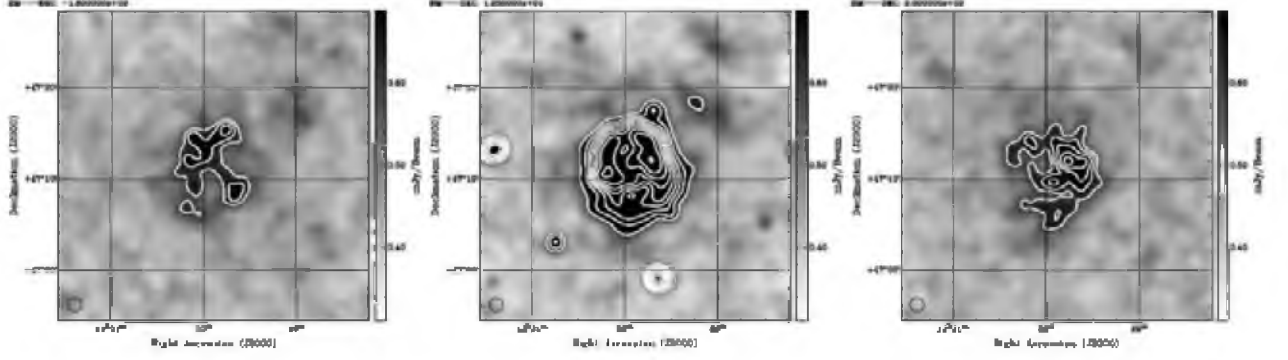
Figure 1.4: Polarized intensity at different Faraday depths towards NGC 5194. The dominant Faraday depth component, centred near +13 rad m^{-2} is shown in the central panel, while the two secondary components near −180 and +200 rad m^{-2} are shown on the left and right. The greyscale varies as indicated. The contours begin at 0.6 mJy beam^{-1} and increase by factor of 1.1 for the secondary components and 1.3 for the primary component. This image and its caption are from Braun *et al.* (2010).

1.3.3 Spectro-polarimetry and rotation measure synthesis

The rotation measure synthesis (RM Synthesis) is a non-standard technique exploiting multi-channel polarimetric observations transformed from λ^2 to the Faraday depth domain. The transformation is performed according to the following formulae (Brentjens & de Bruyn 2005):

$$\tilde{F}(\phi) = F(\phi) * R(\phi) \approx \sum_{j=1}^{N} \tilde{P}_j e^{-2i\phi(\lambda_j^2 - \lambda_0^2)} \tag{1.7}$$

where $\tilde{F}(\phi)$ is the Faraday dispersion function. The Faraday depth is integrated along the distance between the observer and the source emitting polarized radiation

$$\phi[\frac{rad}{m^2}] = 8.1 \times 10^5 \int_0^{L[pc]} n_e[cm^{-3}] \mathbf{B}[Gauss] \cdot dl[pc] \tag{1.8}$$

and depends on the magnetic field component parallel to the line of sight and density of thermal gas n_e. $\tilde{P}_j(\lambda_j^2) = w_j P_j(\lambda_j^2)$ is the observed polarized intensity for a given wavelength (i.e. it is a complex polarized intensity multiplied by the weights which are set to 1 for all the observed wavelengths and 0 otherwise), λ_0^2 is a weighted average of the observed λ^2. In the above equation

$$R(\phi) \approx K \sum_{j=1}^{N} w_j e^{-2i\phi(\lambda_j^2 - \lambda_0^2)} \tag{1.9}$$

is a rotation measure transfer function (RMTF), known also as rotation measure spread function (RMSF). The RMTF is an equivalent of the synthesized beam in the aperture synthesis. $K = (\sum_{j=1}^{N} w_j)^{-1}$ is an inverse sum of all weights.

Contrary to the classic method described above, the rotation measure synthesis allows to separate the polarized emission related to the different zones along the line of sight as well as to precisely determine the distribution of Faraday rotation, see for details Fig. 1.3 as well as Fig. 1.4 and their captions.

There is some analogy between the RM Synthesis and the radio interferometry (with some exceptions, for details, see Brentjens & de Bruyn 2005). Analogically, like a synthesized beam,

a width of RMTF can be estimated taking a "distance" (width) between the lowest and the highest measured λ^2 in the following way:

$$\delta\phi \approx \frac{2\sqrt{3}}{\Delta\lambda^2} \tag{1.10}$$

The maximum extended Faraday depth to which our observations are sensitive can be estimated using the formula

$$max - scale \approx \frac{\pi}{\lambda^2_{min}} \tag{1.11}$$

where λ^2_{min} is the shortest measured λ^2. In turn, the largest Faraday depth to which we are sensitive (in analogy to the field of view in interferometry) can be estimated with

$$\|\phi_{max}\| \approx \frac{\sqrt{3}}{\delta\lambda^2} \tag{1.12}$$

where $\delta\lambda^2$ is a width of a data channel.

In the era of powerful multi-channel correlators, enabling spectro-polarimetric observations, the RM Synthesis has become much popular. Recently, a number of improvements have been proposed for this method, including the wavelet-based rotation measure synthesis (Frick *et al.* 2010; Beck *et al.* 2012) as well as sophisticated methods of deconvolution of Faraday spectra (Li *et al.* 2011; Andrecut *et al.* 2012; Andrecut 2013). In this thesis, I also propose a small improvement for the RM Synthesis method, consisting a more accurate determination of frequency channel weights by taking into account quality of the observed data (see Appendix B for more details). This approach is used in chapters 2 and 4 for NGC 2976 and M 81.

Chapter 2

NGC2976

2.1 Introduction

The generation and evolution of magnetic fields in the low-mass galaxies is still poorly understood. In order to shed a new light on this problem, a multi-frequency, sensitive radio polarimetric observations of a dwarf galaxy NGC 2976 were performed. It is a dynamically simple, bulgeless, pure-disk object, with no discernible spiral arms (Simon *et al.* 2003; Fig 2.1 and 2.2) of SAc type (De Vaucouleurs *et al.* 1991). This galaxy seems to be a scaled version of the class of larger pure-disk spirals (e.g. Gallagher & Matthews 2002, Matthews & van Driel 2000). The unique characteristics of NGC 2976 – morphology of a typical spiral galaxy but its linear size and mass corresponding to those of dwarfs – makes it an ideal laboratory to study magnetic field generation processes in low-mass galaxies. The total power radio emission of NGC 2976 was observed i.a. at 1.4 GHz with the Very Large Array (VLA; Condon 1987, NVSS survey; Fig. 2.1). This galaxy was also included in the WSRT-SINGS polarimetric survey (Heald *et al.* 2009; Braun *et al.* 2010), within which deep and high-resolution observations were performed using the WSRT. *However, the relatively small mass and the dwarf-like rather than spiral character of NGC 2976 went unnoticed in the previous studies.*

Although it rotates with the velocity of about 70 km s^{-1}, several times smaller than that of typical spirals, it is still faster than the low-mass galaxies NGC 4449 and the SMC (50 and 60 km s^{-1}, respectively). As the rotation of the disk in NGC 2976 is also more regular than in the SMC and NGC 4449, it can be expected that the large-scale dynamo process can operate in this object. The rotation curve for NGC 2976 pretty well follows the Brandt law, which leads to a shear rate of 40 Gyr. This is just the limiting value for the dynamo to work, as indicated by the direct MHD simulations of supernovae-driven turbulence in the ISM (Gressel *et al.* 2008).

NGC 2976 is a member of M 81 galaxy group, located close to its centre (see, Fig. 2.3). However, unlike the Magellanic Clouds and NGC 4449, NGC 2976 has probably not been disturbed in any stronger manner for a long time, as it shows very regular U, B, and V isophotes in the outer disk (Bronkalla *et al.* 1992, Fig. 2.1), its HI velocity field is undistorted, and velocity dispersion is small (11 km s^{-1}, Stil & Israel 2002b). Hence, the conditions for the magnetic field generation process (e.g. galactic dynamics, size, mass, star formation rate, etc.) can be constrained for this object without strong influence of gravitational or ram-pressure interactions. Such well-established dynamo conditions are of primary significance in building up theoretical concepts of the dynamo theory (Brandenburg & Subramanian 2005) as well as in explaining magnetic structures that have been observed in the dwarfs.

With the linear size of about 6 kpc and HI mass of 1.5×10^8 M$_\odot$ (Stil & Israel 2002a, Table 2.1), NGC 2976 is several times less massive than SMC and NGC 4449 and could set the
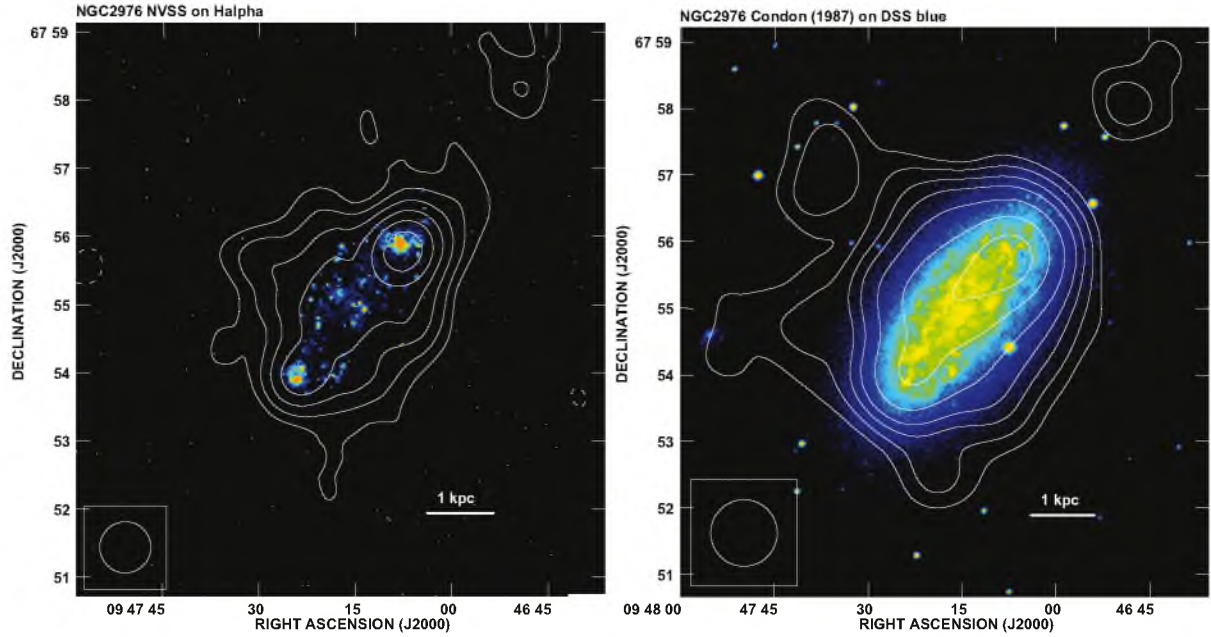
Figure 2.1: Total power contours of NGC 2976 from NVSS (left panel) and (Condon 1987; right panel) superimposed on Hα and DSS blue images respectively. The contours are (3, 5, 8, 12, 17, 23) × 0.35 mJy/beam for NVSS map and (3, 5, 8, 12, 20, 35, 55) × 0.17 mJy/beam for Condon's map.

lowest-mass threshold for a large-scale dynamo to work. Due to its small distance (of 3.6 Mpc), it is an excellent object from the local universe to study magnetic field generation processes in low-mass and pure-disk dwarfs. The disk of NGC 2976 exhibits no strong density waves (see Fig. 2.1, 2.2), so contrary to the typical spiral galaxies, its magnetic fields are not affected by density waves. This could help us to understand the still uncertain interrelation between the dynamo effect and the density waves (Elstner 2005).

Knowledge of properties of magnetic fields in dwarfs is also crucial for explaining magnetization of the IGM. Kronberg *et al.* (1999) suggested in their "boiling universe" concept that the low-mass galaxies were likely sources of primeval fields, because their shallower gravitational potential, as compared to that of more massive spirals, facilitated production of galactic winds and magnetized outflows. However, Chyży *et al.* (2011) argued that for a sample of dwarf galaxies from the Local Group, these objects are rather able to magnetize only their immediate neighbourhood. A similar conclusion was also drawn by Drzazga *et al.* (2011) in their studies of interacting galaxies as potential sources of the IGM's magnetic fields. Thus the question about the origin of the primeval magnetic fields and the role of dwarf galaxies in the magnetization of the Universe remains still open.

An evaluation of contradicting Chyży *et al.* versus Kronberg *et al.* hypotheses about the importance of dwarfs in the IGM magnetization requires studies of a broader class of low-mass galaxies. NGC 2976 with its unique properties constitute an excellent object to supplement the investigated galaxies as it has a low mass but on the other hand, its optical morphology is typical for flocculent, large-mass galaxies, which are known to possess strong and regular magnetic fields (see, Soida *et al.* 2002 and Knapik *et al.* 2000). Accordingly, the objects of this class could be considered to be very efficient generators of magnetic fields and a potential source for seeding the Universe with magnetic fields.

However, the uniqueness of NGC 2976 forces us also to compare the topology of its mag-
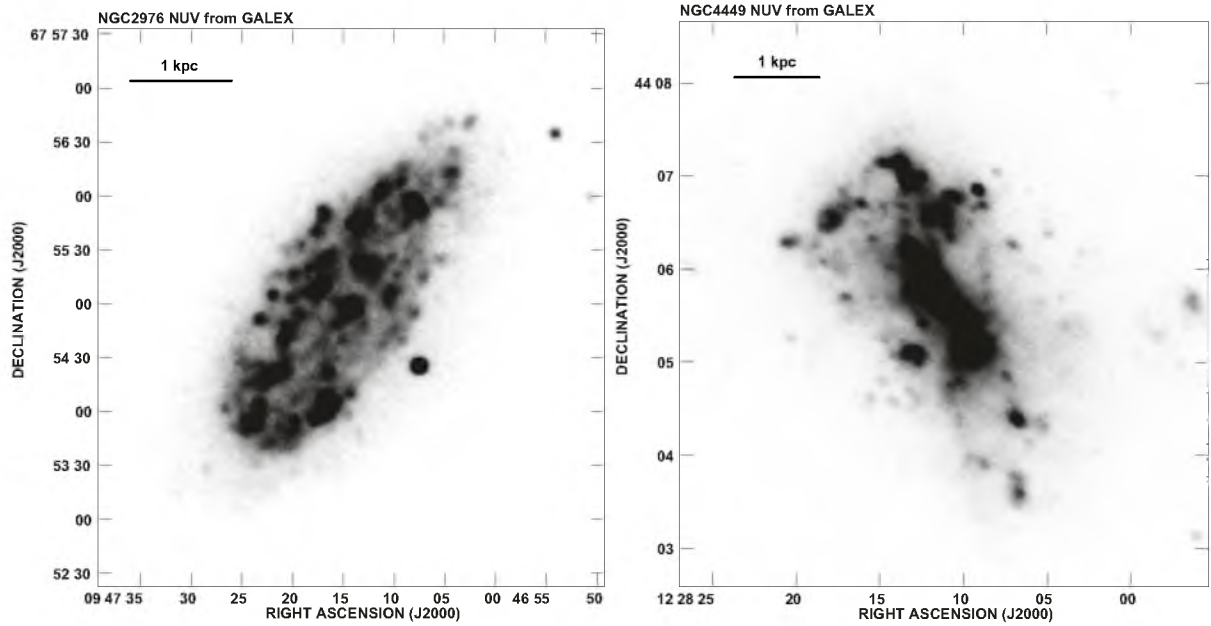
Figure 2.2: A comparison of near UV emission for the pure-disk dwarf NGC 2976 (left) and for the disturbed NGC 4449 (right) from the GALEX data.

netic field with the field topologies of typical (large-mass) spiral galaxies of similar optical morphology and inclination. According to Braun *et al.* (2010), these are crucial observational parameters, influencing determination of signatures of large-scale dynamo in galaxies. Such a consistent comparison, eliminating as much as possible any observational (systematic) effects, should enable us to determine a morphology of the magnetic field in NGC 2976.

The comparison sample of galaxies was selected from the WSRT-SINGS survey[1]. It consists of the five following objects: NGC 925, NGC 2403, NGC 3198, NGC 4559 and NGC 5033 (Fig. 2.4). They are of similar Hubble type to NGC 2976 (Sc or later) and have an inclination of about 60 ($\pm$10) degrees. The basic properties of the sample are given in Table 2.1; a more detailed description of each galaxy can be found in Appendix A.

Studies of magnetic fields in dwarf galaxies are observationally difficult, as these objects are usually radio-weak (e.g. Chyży *et al.* 2011). Hence, I submitted proposals and performed radio observations of NGC 2976 with the most sensitive instruments in the world: the VLA[2] (USA) and 100-meter Effelsberg radiotelescope[3] (Germany). The detailed account of these observations, the data reduction procedure, and the results are presented in the next sections.

2.2 Observations and data reduction

2.2.1 VLA

NGC 2976 was observed with the VLA in L band in C, DnC, and D configurations (Table 2.2). The total on-source time, as calculated from the schedule and dynamic times, was about

---

[1]The data were kindly provided to me by Dr. George Heald (ASTRON, the Netherlands).

[2]The National Radio Astronomy Observatory is a facility of the National Science Foundation operated under cooperative agreement by Associated Universities, Inc.

[3]The 100-m telescope at Effelsberg is operated by the Max-Planck-Institut für Radioastronomie (MPIfR) on behalf of the Max-Planck-Gesellschaft.

18
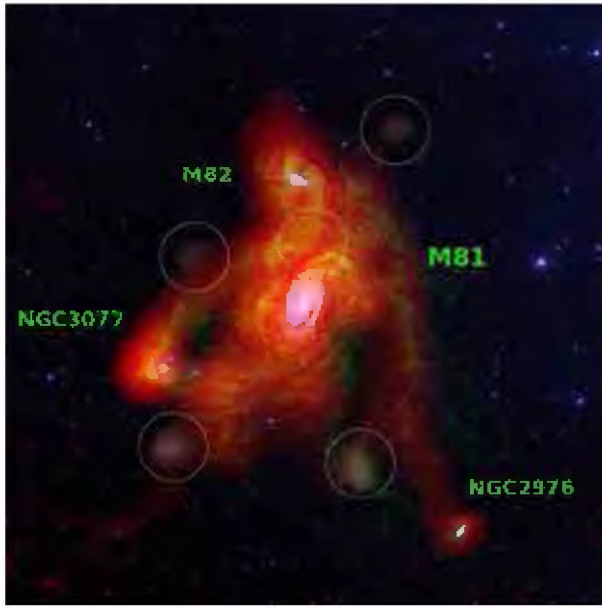
Figure 2.3: Distribution of neutral hydrogen in the central part of the M 81/M 82 galaxy group (Chynoweth *et al.* 2008).
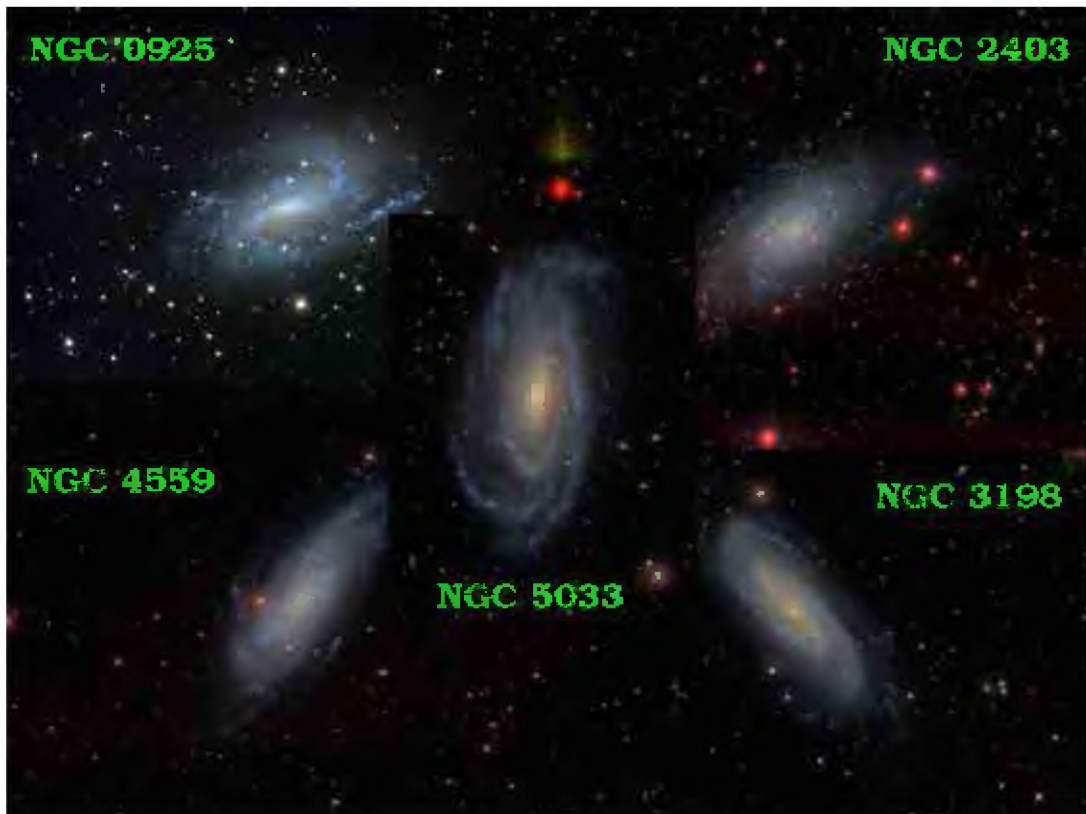
Figure 2.4: The comparison sample of five spiral galaxies selected from the WSRT-SINGS survey. The images were taken from SDSS survey (except for NGC 0925, which image comes from www.mistisoftware.com/astronomy/Galaxies_ngc925.htm)

Table 2.1: Basic properties of NGC 2976 and of the comparison sample of spiral galaxies from the WSRT-SINGS survey.

Name	Hubble [1] Type	Inclination [1] [deg.]	Linear Size [2] [kpc]	HI mass[3] [10^8 M$_\odot$]	SFR [3] [M$_\odot$ / yr]
NGC 2976	**SAc**	**65**	**6**	**1.8 (1.5[4])**	**0.2**
NGC 0925	SABd	66	31	62	2.4
NGC 2403	SABcd	63	12	54	1.3
NGC 3198	SBc	72	24	55	0.85
NGC 4559	SABcd	65	36	112	...
NGC 5033	SAc	66	41	93	2.1

References. 1 - Heald *et al.* (2009), 2 - estimates based on distances taken from Kennicutt *et al.* (2003) and angular sizes (D$_{25}$) from Heald *et al.* (2009), 3 - Kennicutt *et al.* (2003), 4 - Stil & Israel (2002b)

Table 2.2: Parameters of the VLA observations of NGC 2976 at 1.43 GHz.

Type of Obs.	Obs. Date	Configuration	Integr. time [h]	Amp. cal.	Phas. cal.
schedule	28 Aug 2009	C	5.8	0521+166/1331+305	0841+708
dynamic	18 Sep 2009	DnC	0.7	0521+166	0841+708
dynamic	20 Sep 2009	DnC	1.4	0521+166	0841+708
dynamic	21 Sep 2009	DnC	1.6	0521+166	0841+708
dynamic	01 Oct 2009	DnC	1.6	0521+166	0841+708
schedule	31 Oct 2009	D	1.5	1331+305	0841+708
dynamic	06 Nov 2009	D	1.6	1331+305	0841+708
dynamic	11 Nov 2009	D	1.6	0521+166	0841+708

16 hours. The observations were performed in the full polarization mode using two 50 MHz width IFs centred at 1385.100 and 1464.900 MHz. The data were reduced with AIPS package, following the standard procedure. The flux scale and position angle of polarization were calibrated using the amplitude calibrator (0521+166/1331+305). The phase calibrator (0841+708) was used to find gain, phase, and polarization leakage solutions. Each of the datasets specified in Table 2.2 was calibrated in this way separately, and then self-calibrated in phase-only. After checking for consistency between the datasets, they were concatenated and self-calibrated in phase as well as in amplitude and phase. In the final stage, imaging with AIPS task IMAGR was performed for all the Stokes parameters using Briggs' robust weighting of 1 and -5. The obtained Q and U maps were combined within the task COMB to form maps of polarized intensity ($PI = \sqrt{(Q^2 + U^2)}$) and polarization angle ($PA = 0.5 arctg(U/Q)$). The r.m.s. sensitivity (for imaging with robust 1) is 20μJy/beam for the total power intensity (TP), and 9μJy/beam for the polarized intensity (PI).

Table 2.3: Parameters of the Effelsberg observations of NGC 2976 at 4.85 and 8.35 GHz

Obs. Freq. GHz	Obs. Date	Map Size arcmin	Total/Good(TP)/Good(PI) coverages	S_{TP} mJy	S_{PI} mJy	r.m.s. (TP) mJy/beam	r.m.s. (PI) mJy/beam
4.85	May 2009 May 2010 May 2011	35 × 25	24/21/12	30.0 ± 1.4	1.6 ± 0.4	0.45	0.08
8.35	May 2011	21 × 21	66/35/35	19.3 ± 0.9	< 0.8	0.23	0.075

2.2.2 Effelsberg

NGC 2976 was observed with 100-m Effelsberg radiotelescope at 4.85 and 8.35 GHz. At 4.85 GHz, a two-horn secondary focus system with bandwidth of 0.5 GHz was used, recording data in four channels/horn. Two of these channels recorded the total power signal, while the other ones recorded signal in Stokes Q and U. For the object, 24 coverages (maps) in Azi/Alt frame were obtained. However, only 12 of them were suitable for polarization studies (Table 2.3). At 8.35 GHz a 1.1 GHz bandwidth single-horn receiver was used, also recording data in four channels (see above). In this case, 66 coverages in the R.A./Dec. frame were obtained. Unfortunately, nearly half of the data (Table 2.3) were unusable, due to strong RFI-like spikes near the target. At both the observation frequencies, corrections of telescope pointing were made about every 1.5 hour by scanning a nearby strong point radio source.

I performed data reduction in a standard way by applying the NOD2 package (Haslam 1974). First, all coverages at both the frequencies were edited in order to remove any RFI and align baselines to the common level; then the data at 4.85 GHz from the both horns were averaged using the software beam-switching technique (Morsi & Reich 1986) and transformed to the R.A./Dec. frame (for 8.35 GHz data this step was not necessary, see above). In the next stage of data reduction, all usable coverages (Table 2.3) were combined using the spatial frequency weighting method (Emerson & Gräve 1988). In the final stage, all Stokes parameters maps at both the frequencies were digitally filtered to remove spatial noisy structures lesser than the beam sizes and then transformed to the FITS format. Further processing that included flux scale calibration and formation of Polarized Intensity and Polarization Angle maps was performed in the AIPS package. At both the frequencies the flux scales were calibrated using 3C 286, under assumption that its flux is 7.47 Jy at 4.85 GHz and 5.27 Jy at 8.35 GHz (as estimated in the base of the VLA Calibrator List[4]). The obtained r.m.s. noise levels are given in Table 2.3.

2.3 Results

In the following sections (2.3.1 – 2.3.5) I present the radio images obtained for NGC 2976 and compare them with the distribution of neutral hydrogen and images in other spectral domains: infrared (IR), optical, and UV.

---

[4]https://science.nrao.edu/facilities/vla/observing/callist

2.3.1   1.43 GHz

The sensitive polarimetric VLA observations of NGC 2976 resulted in a discovery of some very extended radio emission surrounding the object (Fig. 2.5). Such a radio image of the galaxy was not known earlier, as previously only a total power emission closely related to its optical disk was obtained (Condon 1987; Niklas *et al.* 1995; Stil & Israel 2002a; Heald *et al.* 2009). In the low-resolution total power map (Fig. 2.5), the brightest emission coincides with the sharpened disk of the NGC 2976, and the maximum is well correlated with two bright HII regions located at the edges of the disk. This is even more visible in the high resolution (of about 0.26 kpc) map (Fig. 2.6) superimposed on the 24 μm far-infrared image from Spitzer (Kennicutt *et al.* 2003). There is a good correspondence between images in both wavelengths in the southern part of the disk, which is not the case in the northern part of the object, where radio emission is shifted to the south. This poses some problem for the hypothesis that there is a bar in NGC 2976 (Spekkens & Sellwood 2007).

Beside the stellar disk, the total power radio emission (in the lower resolution map) extends in the north-eastern direction (Fig. 2.5), where a low-brightness signal of about 60 μJy/beam (3 × r.m.s. noise level) resides. The radio emission at the similar level is also observed in the southern part of the galaxy. However, an elongated emission in the south-western part of the image is smaller and brighter than in the opposite direction. The total power radiation of NGC 2976 corresponds well to its HI distribution (Fig. 2.5) in the NE and SW elongations. No such correlation is to be seen in the southern region, where HI is shifted to the north.

The distribution of polarized intensity in NGC 2976 (Fig. 2.7) is even more surprising than the TP one. Most of the observed polarized emission (more than 60%) comes from the south-western part of the object, where the polarization degree reaches 50%. It should be noted that this number does not take into account the regions within the object (close to the total power intensity at the level of 3×r.m.s.) where the polarization degree has unphysical values as high as 100%. This is due to higher sensitivity of the polarized intensity map, which is not bounded by the confusion limit. The brightest southern PI region was also detected by Heald *et al.* (2009) in their high resolution WSRT-SINGS survey (see also Sec. 2.3.5). The B-vectors (magnetic field vectors not corrected for rotation measure) are here mostly perpendicular to the galaxy's disk. The polarized signal is weaker in the disk, and appears only in its southern part. In the northern part of NGC 2976, the distribution of polarized signal forms a "ringed" structure with B-vectors aligned with it. Convolution of the PI map to the lower resolution of 45" (Fig. 2.8) enabled us to detect also a polarized extension in the southern part of the object with the directions of B-vectors coincident with those observed in the south-western blob.

Confrontation of the polarized intensity map of NGC 2976 with its Hα emission (Fig. 2.7) reveals that the PI distribution of the object is quite unusual as compared to the other low-mass galaxies for which polarimetric observations were performed. Typically for dwarfs, the polarized signal is closely related to the regions where massive stars are formed. Such findings were made in NGC 4449, where the emission follows a part of the massive arm actively forming stars (Chyży *et al.* 2000); IC10, in which only a polarized blob near the giant HII region was detected (Chyży *et al.* 2003; but see also Chap. 3); NGC 1569, where multi-wavelength radio observations reveal PI features associated with Hα bubbles – outside the stellar disk (Kepley *et al.* 2010). However, in NGC 2976 the polarized emission resides mostly very far from HII regions, located only within the galactic disk. Even trying to increase the signal-to-noise ratio in Hα map by convolving it to the resolution of radio data does not reveal any extraplanar emission[5]. This is in agreement with Thilker *et al.* (2007), where the galaxy was classified as

---

[5] The same is true for the map in far-UV, which is also a tracer of star formation.

NGC2976 VLA 1.43GHz TP+B PI-vect. on THINGS HI
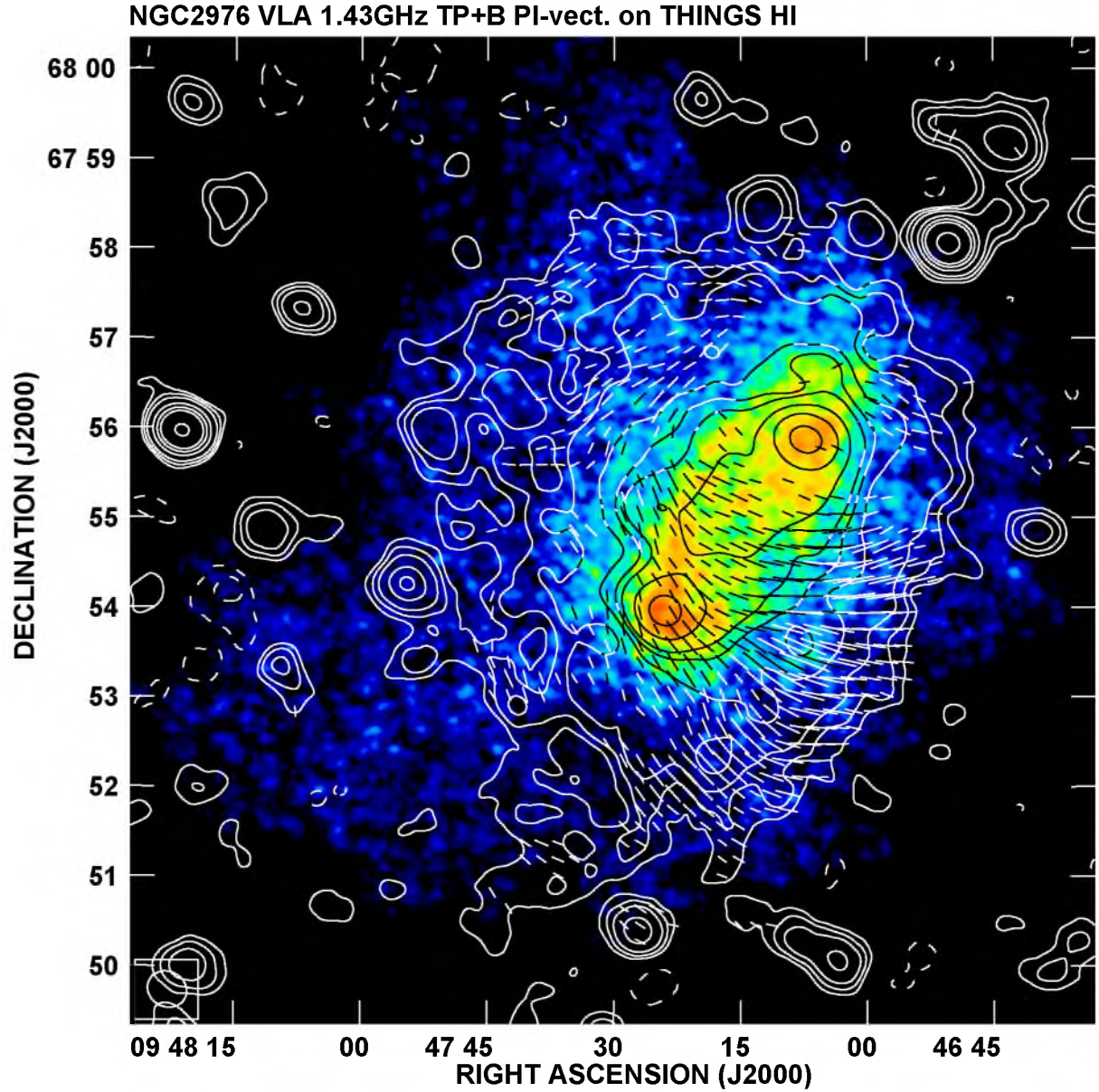
Figure 2.5: Total-power contours and B-vectors of polarized intensity of NGC 2976 (obtained with Robust=1 weighting) at 1.43 GHz superimposed on the HI map (form THINGS survey, Walter *et al.* 2008) shown in a logarithmic scale. The contours levels are (-5, -3, 3, 5, 8, 16, 24, 32, 64, 128, 256) × 20μJy/beam. A vector of 10" length corresponds to the polarized intensity of about 42 μJy/beam. The map resolution is 26.8" × 23.5" HPBW, while the beam position angle is 62 degrees.
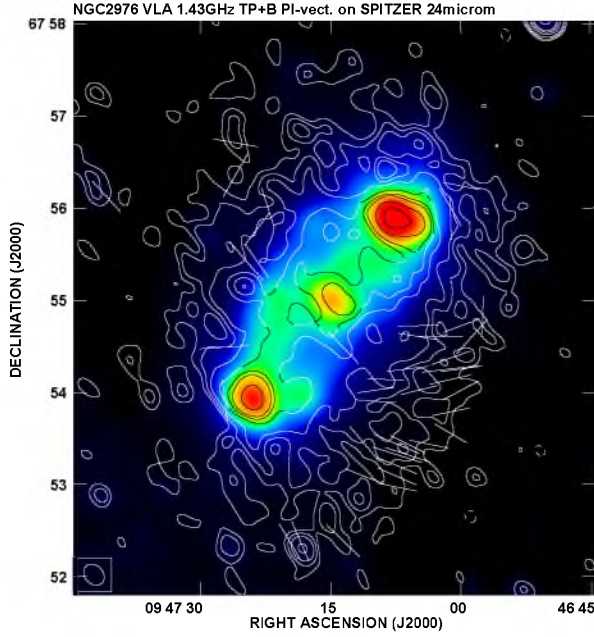
Figure 2.6: Total-power contours and B-vectors of polarized intensity of NGC 2976 (obtained with Robust=-5 weighting) at 1.43 GHz superimposed on the Spitzer 24μm image (Kennicutt *et al.* 2003), shown in logarithmic scale and convolved to the resolution of radio data. The contours levels are (-5, -3, 3, 5, 8, 16, 24, 32, 64, 128) × 20μJy/beam. A vector of 10" length corresponds to the polarized intensity of 20 μJy/beam. The map resolution is 15.1" × 11.9" HPBW, while the beam position angle is 42 degrees.
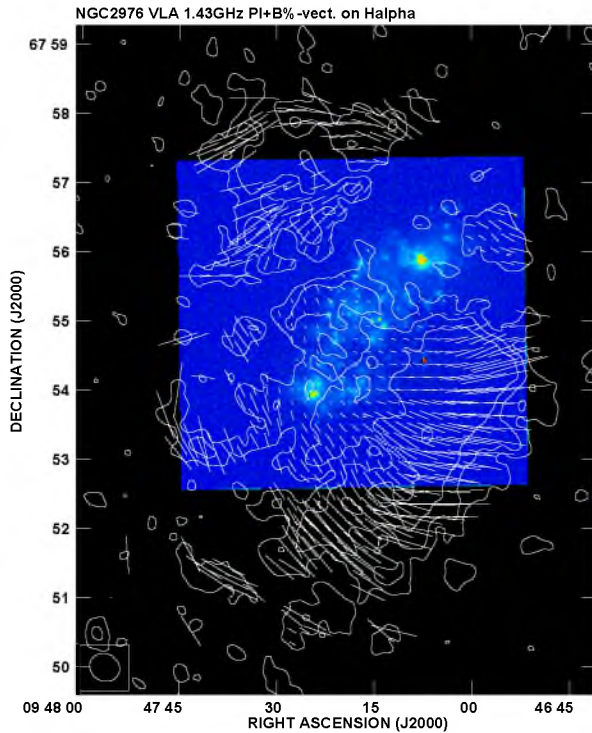
Figure 2.7: Contours of polarized intensity and B-vectors of polarization degree of NGC 2976 (obtained with Robust=1 weighting) at 1.43 GHz superimposed on the Hα image (Dale *et al.* 2009). The contour levels are (3, 5, 8) × 9μJy/beam. A vector of 10" length corresponds to the polarization degree of 12.5%. The map resolution is 26.8" × 23.5" HPBW, while the beam position angle is 62 degrees.
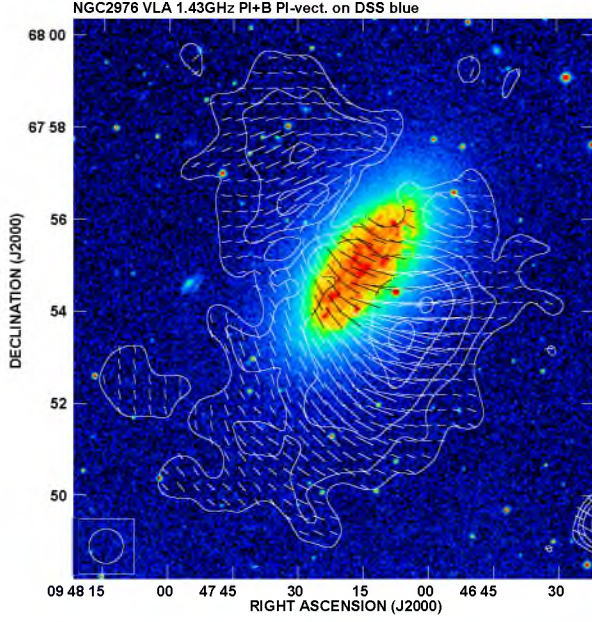
Figure 2.8: Contours and B-vectors of polarized intensity of NGC 2976 at 1.43 GHz convolved to the resolution of 45" superimposed on the DSS blue image. The contour levels are $(3, 5, 8, 16, 24) \times 13 \mu$Jy/beam. The vector of 10" length corresponds to the polarized intensity of about 42 μJy/beam.

not having an extended UV disk.

Basing on the WSRT-SINGS survey, Heald *et al.* (2009) found that in normal galaxies their receding side is significantly depolarized at long wavelengths (of about 20 cm), due to a longer way the polarized waves travel through the magneto-ionic medium. From the HI velocity field observations of NGC 2976 (publicly available within the THINGS survey, Walter *et al.* 2008) I found that the northern part of the object has a receding major axis. This implies that this side of the galaxy should exhibit a less polarized emission as compared to the opposite side. This effect is actually observed for the disk and the SE polarized region (Fig. 2.7), but not for the NW one.

The total power flux measured at 1.43 GHz for NGC 2976 is 65.7 $\pm$ 2.8 mJy, while the polarized intensity flux is 7.8 $\pm$ 0.8 mJy, which gives a total polarization degree of 12 $\pm$ 2%. Such values are typically observed in normal galaxies (Beck *et al.* 1996).

2.3.2 4.85 and 8.35 GHz

In Figure (2.9), a total power emission at 4.85 GHz from the Effelsberg telescope is presented. Its resolution is much lower (152") than in the VLA observations. In this map, similarly to the high-resolution data, the TP signal has a maximum shifted to the north part of galaxy's disk, where one of the giant HII regions is located. The low-level emission of 1.35 - 2.25 mJy/beam is elongated in the NE direction, but there is no such elongation to SE. A similar asymmetry was observed in the 1.43 GHz data (Fig. 2.5). The elongation in NW direction seems to be correlated with a source visible also at 1.43 GHz. The total power flux of NGC 2976 measured at 4.85 GHz is 30.0 $\pm$ 1.4 mJy (Table 2.3), which is in excellent agreement with the radio flux determined at the same frequency by Gregory & Condon (1991).

The morphology of polarized intensity at 4.85 GHz (Fig. 2.9) closely resembles that at 1.43 GHz. Here also most of the polarized flux (about 80%) comes from the southern part of the disk and the southern extension. Only some small polarized blobs have been detected in northern direction. The narrow emission from the disk is located close to the galaxy centre, while at 1.43 GHz it is shifted to the south.

In order to eliminate the beam depolarization effect and compare polarization degrees at both the frequencies, I convolved the VLA 1.43 GHz Q and U Stokes maps to the resolution of
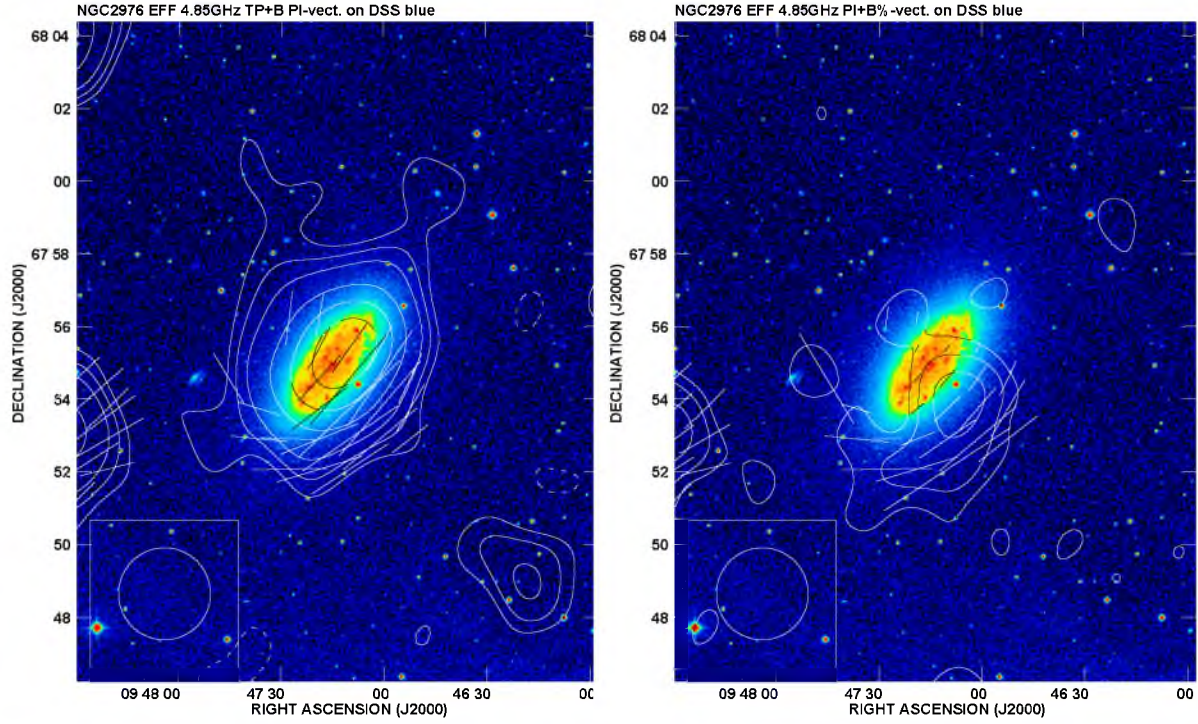
Figure 2.9: Left: Total-power contours and B-vectors of polarized intensity of NGC 2976 at 4.85 GHz superimposed on the DSS blue image. The contours levels are (-5, -3, 3, 5, 8, 16, 24, 32) × 450μJy/beam. The vector of 10" length corresponds to the polarized intensity of 33 μJy/beam. Right: Contours of polarized intensity and B-vectors of polarization degree of NGC 2976 at 4.85 GHz superimposed on the DSS blue image. The contour levels are (3, 5, 8) × 80μJy/beam. The vector of 10" length corresponds to the polarization degree of 1.3%. The maps resolution is 152" × 152" HPBW.

the Effelsberg data (152"). In effect, polarization degrees of about 9% at 1.43 GHz and about 5% at 4.85 GHz were obtained (the polarized flux at 4.85 GHz is 1.6 ± 0.4 mJy, Table 2.3). This is quite a surprising result, as at shorter wavelengths, a lower depolarization due to Faraday effects (Faraday dispersion and differential rotation) is expected (Beck *et al.* 1996). Usually there is a significant depolarization observed in the nearby galaxies at 20 cm (as compared to 6 cm data). A good example of this phenomenon can be found in NGC 4254 (Chyży *et al.* 2007a) or even more distinctly in the observations of the low-mass galaxy NGC 1569 (Kepley *et al.* 2010). It should be noted that the difference in polarization degrees found in NGC 2976 cannot be simply accounted for by the nature of radio emission, which intensity depends on observational frequency. The only explanation could be a difference in sensitivities of the data presented. On the other hand, it could mean that depolarization effects in the investigated object are small.

The noticeable difference in the polarized emission between 4.85 GHz and 1.43 GHz is related to orientations of B-vectors. At 4.85 GHz, the vectors are nearly perpendicular to those observed at the lower frequency. As the Faraday effects are smaller at shorter wavelengths, we can expect that the directions of B-vectors observed at 4.85 GHz are close to the intrinsic directions of magnetic field vectors.

The total power emission of NGC 2976 at 8.35 GHz is presented in Fig. 2.10. It is closely related to the optical disk. There is no radio emission extension to the NE direction seen at lower frequencies, as it should be expected for a steep-spectrum radiation.
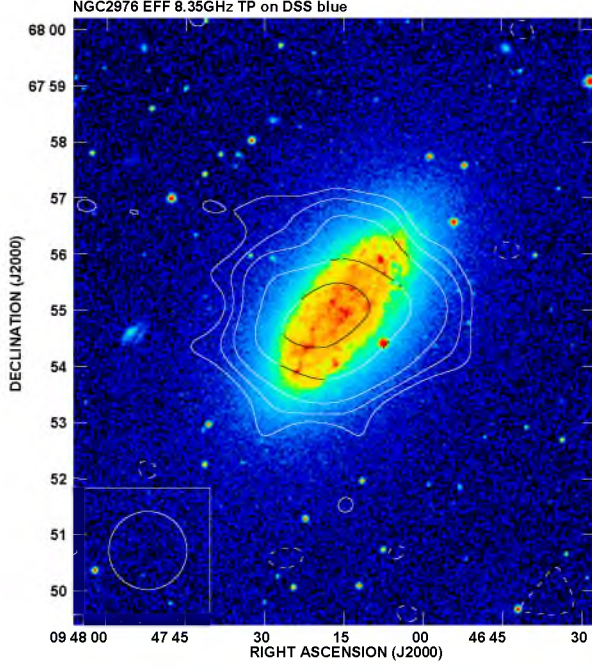
Figure 2.10: Total-power contours of NGC 2976 at 8.35 GHz superimposed on the DSS blue image. The contours levels are (-5, -3, 3, 5, 8, 16, 24) × 230μJy/beam. The map resolution is 84" × 84" HPBW.

Total power flux measured for this frequency is 19.3 ± 0.9 mJy (Table 2.3). For the polarized intensity, only an upper limit of flux could be estimated, which at 2.5 × r.m.s. noise level (of 75μJy/beam) within the optical disk is < 0.8 mJy (Table 2.3). This implies an upper limit of polarization degree of < 4%.

2.3.3 Spectral index distribution

The spectral index provides an important clue about possible mechanisms underlying generation of radiation in galaxies. In normal spirals, there are two main processes responsible for the observed emission at radio wavelengths – synchrotron and thermal radiation. Each of these mechanisms produces its respective shape of the spectrum. For synchrotron emission, the spectral indices are about -0.5 (S $\propto \nu^{\alpha}$) for relativistic electrons at the site of their acceleration (in supernovae remnants) and get lower as the particles age in magnetic fields. The expected spectral index for the thermal component of radio emission produced by free-free radiation of (thermal) electrons is -0.1.

The map of spectral index distribution shown in figure 2.11 was computed for NGC 2976 using the maps at 1.43 GHz and 4.85 GHz, after convolving them to a common resolution. Despite the low resolution of the map, one of the large HII regions in the northern part of the disk, where the spectral index reaches values as high as -0.4 – -0.5, is visible. In the rest of the disk, the spectral index of about -0.6 – -0.7 is observed. Such values are normally encountered in spiral arms of galaxies (see, e.g. Chyży *et al.* 2007a). This can mean that the emission from the optical disk is dominated by the radiation of young relativistic electrons spiralling in magnetic field with some small contribution from thermal emission (see, Sec. 2.4.1). Outside the disk, the spectrum steepens sharply, reaching values of about -0.9, apparently due to aging of relativistic particles there. A similar effect was found e.g. for NGC 1569 (Kepley *et al.* 2010).
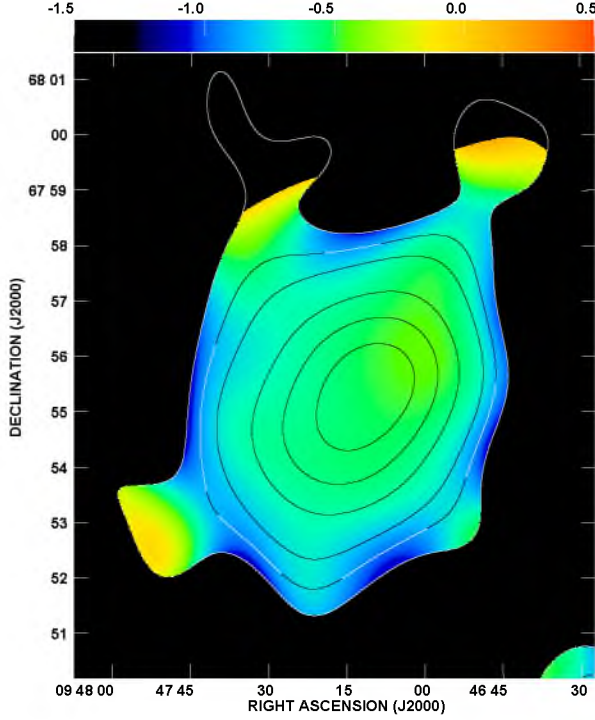
Figure 2.11: Radio spectral index distribution between 4.85 and 1.43 GHz in NGC 2976 (colours). The both maps of total intensity were convolved to a common beam of 152" (the beam is not shown). The contours represent the total power map at 4.85 GHz, their levels are: (-5, -3, 3, 5, 8, 16, 24, 32) × 450μJy/beam.

2.3.4 Distribution of rotation measure and depolarization

In Fig. 2.12 distribution of rotation measure (see, Sec. 1.3.2 for definition) is shown. It was calculated in a "classic" way on a pixel-by-pixel basis, using the polarization angle maps available at two frequencies of 1.43 and 4.85 GHz. It can be noted from this map that rotation measure observed for NGC 2976 is mostly negative (a small region of positive RMs in the north does not seem to be real). The values of RM change smoothly from the north to the south-western direction. In the north part of the object, RM has a value of about -35 rad m^{-2}. In going to the south, the rotation measure grows from -30 to -23 rad m^{-2}, taking a value of about -13 rad m^{-2} in the galaxy's SE part.

The negative RM observed for the entire object could suggest that the component of magnetic field along the line of sight is directed away from the observer. However, when analysing data on rotation measure, the contribution from the Milky Way should be taken into account. One of the most standard ways to determine this contribution consists in using some nearby polarized background sources. In case of the NGC 2976, such a suitable source is located at R.A.(J2000.0): 09^{h}48^{m}35^s, Dec(J2000.0): 67°53′10". Assuming that its internal RM is negligible, the foreground rotation measure for this source is about -35 rad m^{-2}. This is in an excellent agreement with the foreground rotation measure in the direction of NGC 2976 reported by Heald *et al.* (2009) basing on their WSRT-SINGS data. This foreground RM also roughly agrees with the all-sky map published by Johnston-Hollitt *et al.* (2004).

Thus, taking into account the Milky Way rotation measure, one obtains that within NGC 2976 actually magnetic field directed towards the observer can be seen. After correcting for the foreground RM, they range from 0 in the north to +22 rad m^{-2} in the south-east. These values are almost an order of magnitude lower than rotation measures typically observed in normal galaxies at high frequencies (of about ± 100 rad m^{-2}, Beck & Wielebinski 2013) and some dwarf galaxies e.g. NGC 4449 (Chyży *et al.* 2000) and NGC 1569 (Kepley *et al.* 2010). The rather low value of rotation measure found in NGC 2976 could imply that the regular magnetic fields are weak in the object. Other possible explanations are that there is a low content of thermal
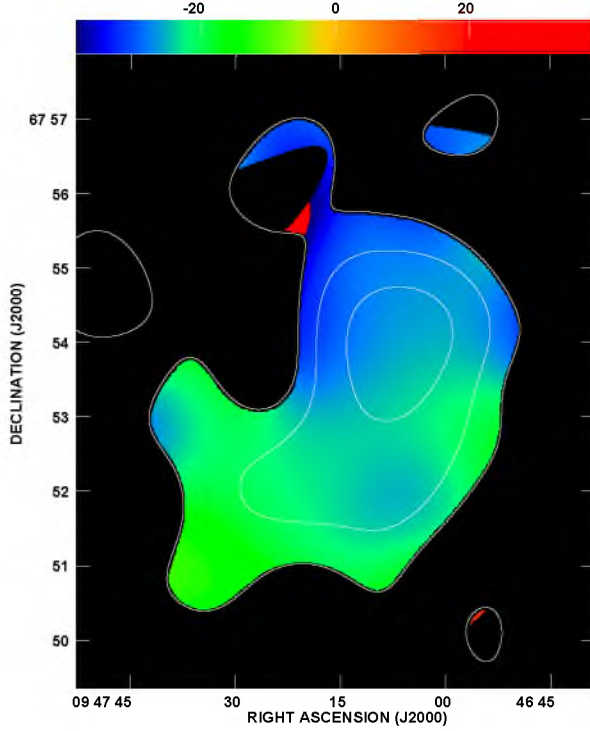
Figure 2.12: Distribution of Faraday rotation measure (in rad m^{-2}, not corrected for the foreground RM) from the data at 4.85 and 1.43 GHz in NGC 2976 (colours). The contours represent the polarized intensity map at 4.85 GHz, the levels are: (3, 5, 8) × 80μJy/beam. The map resolution is 152".

electrons (which also affect rotation measure) in the regions from which polarized intensity comes or that the magnetic field in NGC 2976 is aligned mainly in the sky plane.

For the object investigated, it was also possible to calculate distribution of Faraday depolarization (Fig. 2.13) defined as DP = $p_{1.43GHz}$/$p_{4.85GHz}$, where $p_{1.43GHz}$ is the degree of polarization at 1.43 GHz and $p_{4.85GHz}$ is the degree of polarization at 4.85 GHz – both obtained from the same angular resolution data. Faraday depolarization typically leads to decreasing polarized intensity with lowering observational frequency. In the most general case, it is caused by differential Faraday rotation (related to the regular magnetic fields), Faraday dispersion (related to the turbulent component of magnetic field), and RM gradients (due to systematic variations of regular component of magnetic field).

The depolarization determined for NGC 2976 is very low. The highest DP values, ranging from 0.7 to 1.0, are found in the parts of galaxy extended furthest to the south and the north as well as at the position coincident with the region of brightest polarized intensity (at 4.85 GHz, see Fig. 2.9). In the other regions detected in PI, the depolarizations are lower, which confirms the distribution of rotation measure mentioned above, implying that the Faraday effects in NGC 2976 are relatively small.

2.3.5 RM Synthesis

For NGC 2976, spectro-polarimetric observations with the WSRT were performed as well and analysed using the RM Synthesis method (Heald *et al.* 2009) but with very high spatial resolution and low sensitivity to extended radio structures. After accessing those data with permission of the authors and re-analysing them (see Appendix A for details), it was possible to discover polarized intensity structures (Fig. 2.14), not seen previously in the radio maps published by Heald *et al.* (2009). A comparison of the new WSRT-SINGS and VLA (cf. Fig. 2.8) polarized intensity images reveals that the distributions of PI in both the datasets are in very close agreement. Similarly like in the VLA, also in the WSRT image a characteristic southern bright PI region and an extension to the north are visible. Furthermore, these new data confirm ex-
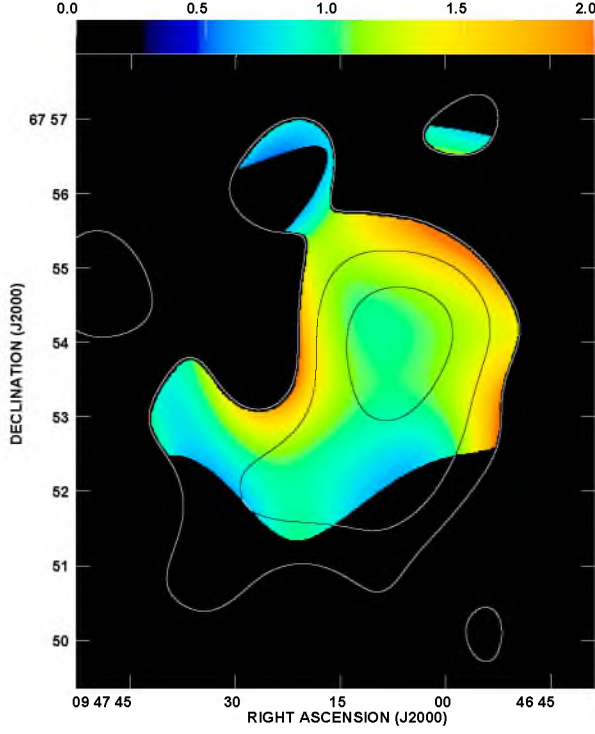
Figure 2.13: Distribution of Faraday depolarization between 4.85 and 1.43 GHz in NGC 2976 (colours). The contours represent the polarized intensity map at 4.85 GHz, their levels are: $(3, 5, 8) \times 80\mu$Jy/beam. The map resolution is 152".

istence of the polarized emission in the SE direction, which was seen after convolution of the VLA image to the lower resolution of 45". The only noticeable difference concerns the PI, which in the WSRT map extends far to the west, while in the VLA image the extension is much smaller. It is a matter of debate if this structure is real at all. Whether it is detected (in WSRT data) or not (in VLA data) can be caused by some imaging artifacts related to the bright source located at R.A.(J2000.0): $09^h48^m35^s$, Dec(J2000.0): $67°53'10"$. Beside the PI emission, also orientations of B-vectors agree well between both the observations[6].

Scanning through the RM Cube along the Faraday depth reveals that the polarized emission coming from NGC 2976 is mostly point-like in this domain. It is in an agreement with the findings of Heald *et al.* (2009). In Fig. 2.15, the slice from the cube (at the depth of -25 rad m^{-2}) is shown, where most of detected polarized signal can be seen.

Taking into account that there is only one point-like Faraday component in the cube, it was possible to construct a rotation measure map for the object (Fig. 2.16). The distribution of RM as shown in the image was cut off at the $3 \times$ r.m.s. (of 25 μJy/beam) noise level. Note that, according to Brentjens & de Bruyn (2005), in order to determine reliable rotation measures using the RM Synthesis method, a total S/N greater than 4 is needed (this is marked in the image by the first PI contour). Comparison of the high resolution (48.6" $\times$ 45", cf. Table A.1) RM map obtained with RM Synthesis technique to the low resolution RM map (Fig. 2.12) obtained by the "classical method" shows that they are similar. Particularly noticeable are the negative RMs found in the strongly polarized SW region (this region shows RMs of about -25 rad m^{-2}). In the northern, south-eastern, and western parts of the galaxy, where signal-to-noise ratio is lower, RM distribution is more chaotic.

---

[6]The central frequencies between the datasets differ slightly; for WSRT, it is about 1.5 GHz, while for VLA, it is 1.43 GHz, so the B-vectors orientations are actually a bit different.
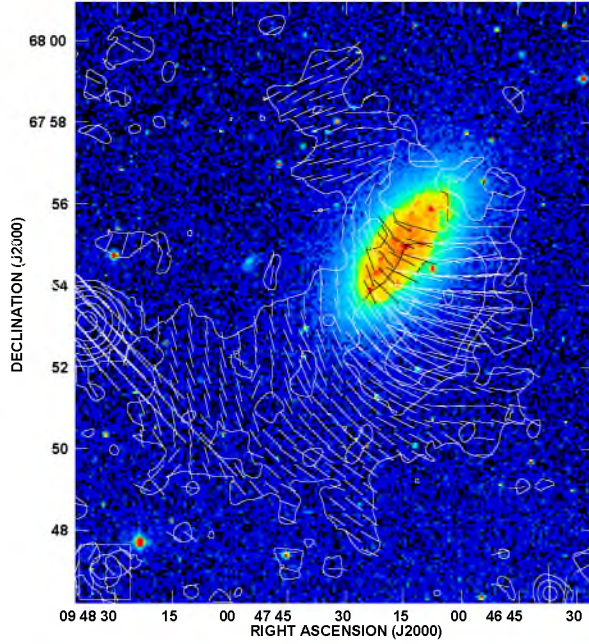
Figure 2.14: Contours and B-vectors of polarized intensity of NGC 2976 from the WSRT-SINGS data superimposed on the DSS blue image. The contour levels are (3, 5, 8, 16, 32, 64) × 25μJy/beam. The vector of 10" length corresponds to the polarized intensity of about 31.3 μJy/beam. The map resolution is 48.6" × 45.0" HPBW.
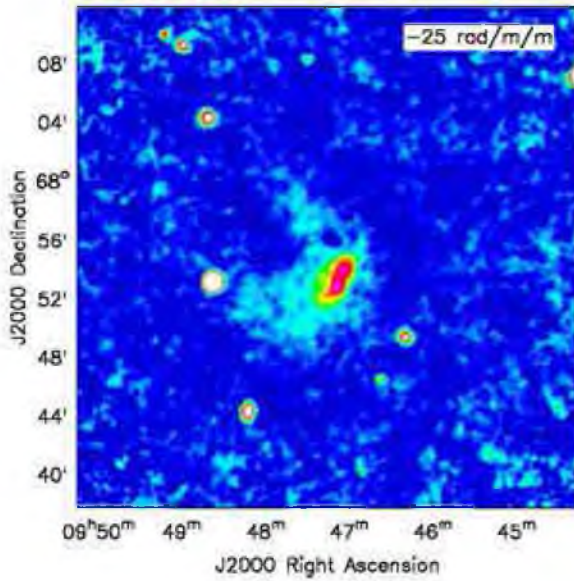
Figure 2.15: The particular Faraday depth of -25 rad m^{-2} for which most of polarized emission from NGC 2976 was detected.

31
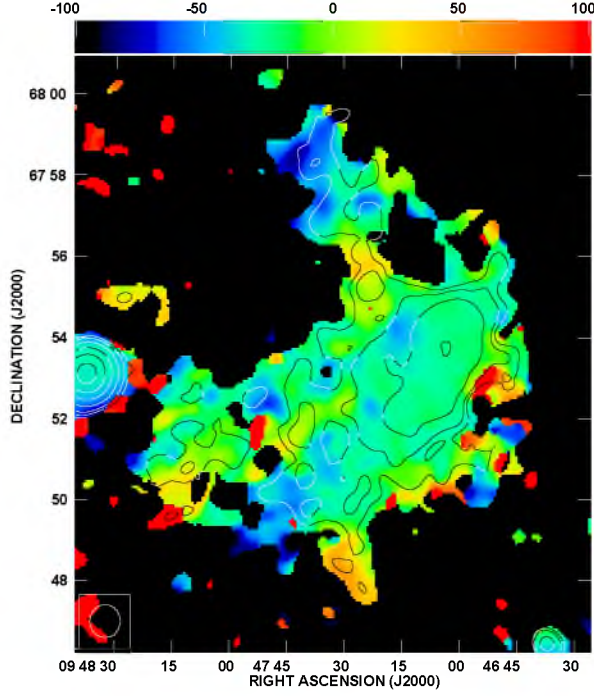
Figure 2.16: Distribution of Faraday depths (in rad m^{-2}) for the maximum of polarized intensity signal for NGC 2976 (see text for details). The contour levels representing the polarized intensity are: $(4, 5, 8, 16, 32, 64) \times 25\mu$Jy/beam. The map resolution is 48.6" $\times$ 45.0" HPBW.

2.4 Discussion

2.4.1 Thermal fraction

Radio emission of normal galaxies has thermal and non-thermal components. In order to be able to estimate the magnetic field strength, which is directly related to the non-thermal radio emission, both these components must first be properly separated. The best method of their separation consists in fitting a simple model of thin optical disk to the radio data (Niklas *et al.* 1997). The model is described by the following equation:

$$\left(\frac{S_\nu}{S_{\nu_0}}\right) = f_{th}(\nu_0)\left(\frac{\nu}{\nu_0}\right)^{-0.1} + (1 - f_{th}(\nu_0))\left(\frac{\nu}{\nu_0}\right)^{-\alpha_{nth}} \tag{2.1}$$

where S_ν and S_{ν_0} are radio fluxes for a given frequency and the frequency for which the separation will be performed. $f_{th}(\nu_0)$ is the so-called thermal fraction, being a ratio of thermal and total radio fluxes, and α_{nth} is the non-thermal spectral index. For the thermal emission, a spectral index of -0.1 (based on the theoretical considerations) is assumed. In the case of NGC 2976, it was possible to use this method as the radio observations were performed at three frequencies. Moreover, as it was pointed out in Sec. 2.3, this galaxy was also observed in the 2.8 cm survey of Shapley-Ames galaxies (Niklas *et al.* 1995). Thus, four measurement points (Fig. 2.17) are available, which is a minimum enabling to fit the above model and get the desired thermal fraction and non-thermal spectral index. The thermal fraction obtained in this way f_{th} is 0.16 +/- 0.12 at 1.43 GHz, while α_{nth} is -0.82 +/- 0.20. However, it should be noted that the highest frequency data point in the spectrum (from Niklas *et al.*) seems to be shifted upwards from the fit and should be regarded with caution. After discarding it, the thermal fraction is 0.12 +/- 0.02 at 1.43 GHz (assuming a typical non-thermal spectral index value of -0.8).

An alternative method of separation of thermal and non-thermal emission (independent of the non-thermal spectral index) consists in estimation of thermal radio flux using the star formation tracers, for instance, Hα emission (see e.g. Niklas *et al.* 1997; Chyży *et al.* 2007a). It should be stressed, however, that Hα is affected by internal extinction, usually little known (if

32
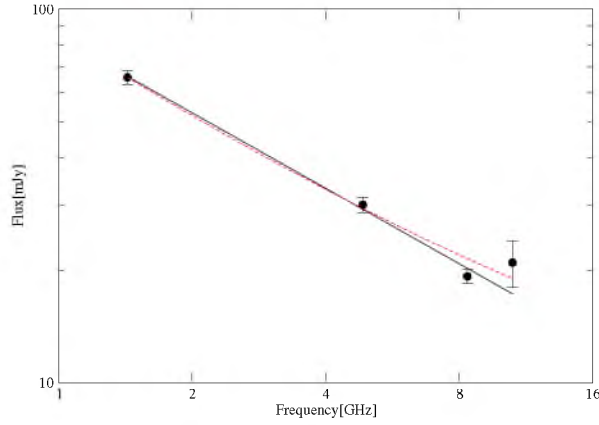
Figure 2.17: Radio spectrum of NGC 2976. The point at the highest frequency is from Niklas *et al.* (1995). The solid black line represents a power-law model fitted to the data. The red dashed line represents the fitted model of a thin disk, in which f_{th} = 0.16 and α_{nth} = -0.82 (see text for details).

at all), which makes this method less effective. The extinction uncertainty is more problematic for the large well-evolved spiral galaxies than for the low-metalicity dwarfs. According to the recent studies, it is possible to estimate this effect by taking into account also data on infrared emission (Calzetti *et al.* 2007; Kennicutt & Evans 2012). By inserting the Hα and infrared emission into the classical formula of thermal flux estimation (Niklas *et al.* 1997), I have obtained the radio thermal flux at frequency ν:

$$S_\nu[mJy] = 2.238 \times 10^{\varsigma} \left(\frac{S_{H\alpha} + 0.020\nu_{IR}S_{IR}}{erg\ s^{-1}\ cm^{-2}} \right) \times \left(\frac{T_e}{K} \right)^{0.42} \times \left[ln\left(\frac{0.04995}{\nu[GHz]} \right) + 1.5ln\left(\frac{T_e}{K} \right) \right]$$
(2.2)

where, $S_{H\alpha}$ and $\nu_{IR}S_{IR}$ are Hα and IR (multiplied by the IR frequency) fluxes, respectively. For NGC 2976 the Hα, flux was taken from Kennicutt *et al.* (2008), while the IR, 24μ flux was taken from the Spitzer satellite observations (Dale *et al.* 2009). T_e was assumed to be 10^4 K. The thermal fraction obtained in this way is 0.17 ± 0.02 at 1.43 GHz, in an excellent agreement with the results of the fitting method.

This is quite unexpected indeed, as such thermal fractions and non-thermal spectral indices are typically observed for normal spiral galaxies, much more massive than NGC 2976. Niklas *et al.* (1997) determined the mean f_{th} of 0.08 ± 0.01 (at 1 GHz) and an average α_{nth} of 0.83 ± 0.02 for a sample of 74 galaxies of various morphological type. For the dwarfs, much higher thermal fractions were found; Chyży *et al.* (2003) estimated that for IC 10 f_{th} reaches level of 0.6 and for NGC 6822, it is even as high as 0.8-0.9 at 10.45 GHz (the thermal fraction of NGC 2976 at this frequency would be only about 0.45). Even higher f_{th} were obtained for three late-type galaxies characterized by low star-formation activity (Chyży *et al.* 2007a). In the same sense as thermal fraction, also the global spectral index of NGC 2976 (0.67 ± 0.03) follows the value of 0.74 ± 0.12 found for a sample of normal galaxies (Gioia *et al.* 1982).

2.4.2 Magnetic field strength

After separating the thermal and non-thermal emissions, it was possible to estimate the strength of magnetic field (cf. Sec. 1.3.1) in the investigated object. The formulas given by Beck & Krause (2005) were used for this purpose with the assumption of energy-density equipartition between the total field and cosmic rays (CR). A typical disk thickness (corrected for the projection effects) of 1 kpc and the proton-to-electron ratio of 100 were assumed in the calculations (using the non-thermal spectral index of 0.83 from Niklas *et al.*). The mean non-thermal surface brightness was measured in the area determined by the requirement of radio emission being at

the level of at least 3σ noise level at 1.43 GHz (see Sec. 2.3), giving the total magnetic field strength B_{tot} of $6.6 \pm 1.8\,\mu G$.

The total magnetic field strength obtained is higher than the mean value of $< 4.2 \pm 1.8\,\mu G$ found for a sample of the Local Group dwarfs (Chyży *et al.* 2011), but lower than the average value of $9 \pm 2\,\mu G$ estimated for a sample of 74 galaxies of various morphological type (Niklas 1995). However, it should be noted that the Niklas sample included also interacting objects, which are usually characterized by higher magnetic fields strengths than those in normal galaxies (Drzazga *et al.* 2011). In spiral galaxies with moderate star formation activity, e.g. in M 31 and M 33, thus more similar in this sense to NGC 2976 (for which SFR ≈ 0.12 M⊙/yr), the field strengths of only about $6\,\mu G$ were found (Beck & Wielebinski 2013).

Another important parameter to describe galactic magnetic field properties is field regularity, defined as a ratio of the ordered (B_{ord}) and random (B_{ran}) magnetic field components. It is a useful measure of net production of ordered field. The B_{ord} estimated from the data about polarized flux for NGC 2976 is $2.8 \pm 0.8\,\mu G$. This is a typical value for the spirals, in which ordered fields in the range of $1 - 5\mu G$ are observed (Beck & Wielebinski 2013). Along with the random field component (which for NGC 2976 is $B_{ran} = 6.0 \pm 1.6\,\mu G$), this gives a very high value of field regularity of 0.46 ± 0.17. Consequently, with respect to the strength of magnetic field components, NGC 2976 resembles well-defined spiral galaxies rather than dwarfs.

2.4.3 Generation of magnetic field

As it was shown in Section 2.3, non-zero rotation measures were found for NGC 2976, which can suggest that this object hosts a large-scale partially regular magnetic field. One of the mechanisms to explain generation of such field is a large-scale magnetohydrodynamic dynamo (see Sec. 1.1). In order to investigate if this process can be at work in this galaxy, one can estimate its efficiency, usually described by a dynamo number (Shukurov 2007):

$$D \approx 9\frac{h_0^2}{u_0^2}s\omega\frac{\partial\omega}{\partial s} \tag{2.3}$$

where, h_0 is the vertical-scale height of the galactic disk, u_0 is the velocity of turbulent motions, s is the radial distance from the centre of the galaxy, ω is the angular velocity and $s\frac{\partial\omega}{\partial s}$ is the shear ratio. To estimate this number for NGC 2976, I assumed a scale height of 0.5 kpc, typical for dwarf galaxies (e.g. Chyży *et al.* 2011) and u_0 of 11 km s^{-1} (Stil & Israel 2002b). The dynamo number was computed for a radius of 2.0 kpc, within which the rotation curve can be approximated as flat (as it was suggested by Stil & Israel 2002b, but questioned by de Blok *et al.* 2008). At this distance, the rotation velocity reaches a value of about 71 km s^{-1} (Stil & Israel 2002b). This gives a shear ratio of about 36 km s^{-1} kpc^{-1} and the absolute value of the dynamo number of about 23, which is comparable to the dynamo number (of about 20) obtained for the Milky Way at the distance of the Sun (Shukurov 2007). It exceeds the critical limit $|D_{critical}| \sim 8 - 10$, below which the large-scale dynamo is inefficient (Shukurov 2007). Such a value does not seem to be typical for dwarf galaxies, for which mostly subcritical dynamo numbers were obtained (Chyży *et al.* 2011; Mao *et al.* 2008). Even for the Large Magellanic Cloud (LMC), which is much larger and more massive than NGC 2976, Mao *et al.* (2012) estimated $|D|$ as ~ 10 only.

Application of the classical mean $\alpha - \omega$ dynamo theory to the galaxies is problematic, due to its long growth timescale, being of an order of 10^9 years (see, e.g. Shukurov 2007). Even worse is the situation for the low-mass objects, which rotate slower and more chaotically than spirals. For the LMC Mao *et al.* (2012) estimated time of amplification of magnetic field of

about 2.7 Gyr. However, a new and much more efficient large-scale dynamo mechanism has been proposed – the so-called cosmic-ray driven dynamo (Hanasz et $al.$ 2009). In this kind of dynamo process, supernova explosions produce cosmic rays, which pressure leads to increased efficiency of the α effect, responsible for generating the poloidal component of magnetic field (see also Sec. 1.1). It was successfully applied to date in simulations of magnetic fields in spiral (Hanasz et $al.$ 2009) and barred galaxies (Kulpa-Dybeł et $al.$ 2011), yielding dynamo growth timescales of 270 Myr and 300 Myr respectively. Also for dwarfs, the CR dynamo is considered to be a particularly attractive mechanism able to account for their regular magnetic fields (Gaensler et $al.$ 2005; Kepley et $al.$ 2010, Mao et $al.$ 2012). This explanation is further supported by the recent global numerical simulations of dwarfs performed by Siejkowski (2012), who found that magnetic field can be amplified in low-mass objects only if their rotational velocity exceeds 40 km s^{-1}, However, a velocity of at least 60 km s^{-1} is needed for efficient generation of magnetic field, and for such fast rotators, their dynamo action depends mainly on rotational velocity.

By confronting the maximum rotational velocity of NGC 2976 with these results, one can see that the cosmic-ray driven dynamo is actually able to operate efficiently in this object with e-folding amplification time not greater than 400 Myr (cf. Siejkowski's models with $v_{rot} \geq$ 60 km s^{-1}). Furthermore, the strength of magnetic field in NGC 2976 (Sec. 2.4.2) is in rough agreement with the simulations, where for the fast rotating models it is at the level of a few μG.

2.4.4 Magnetic field morphology of NGC 2976 – comparison with subsample of the other WSRT-SINGS galaxies

Apart form the field strength, also its morphology is crucial in discussing the large-scale dynamo process. In Fig. 2.18a, a distribution of magnetic field orientations (B-vectors corrected for Faraday rotation) is presented for NGC 2976. The map was computed only for the regions where signal-to-noise ratio was high enough (see, Brentjens & de Bruyn 2005). The most surprising are the almost azimuthal directions of the field in the southern part of the object, where the maximum of polarized intensity is observed. Hence, we can suspect that the magnetic field in NGC 2976 could not be generated by the galactic-scale dynamo action alone, since then a spiral morphology of magnetic fields would have arisen. So far, such a field was observed most clearly in the ring galaxy NGC 4736 (Chyży & Buta 2008), not exhibiting, like NGC 2976, any strong density waves. This either cannot be accounted for by the fact that the observations were made at long wavelengths as the observed field morphology does not fit the model of Braun et $al.$ (2010, see Sec. 2.3). The nearly azimuthal magnetic field in the south, along with the enhanced polarized intensity and no corresponding enhancement of total power emission (cf. Fig. 2.5 and Fig. 2.7) imply strong field compression in this part of the galaxy. The field regularity of 114 ± 48 % estimated for this area is actually very high, as it is 2.5 times higher than the average value (Sec. 2.4.2). Also the field with mostly radial directions found in the northern part of the object is not typical for the dynamo action. It can be a signature of field stretching, observed e.g. in the gravitationally interacting Antennae galaxies (Chyży & Beck 2004) and in the NGC 2207/IC 2163 galaxy pair (Drzazga et $al.$ 2011, see below).

As NGC 2976 is representative for the pure-disk dwarf objects studied for the first time in the aspect of characteristics of its magnetic field, I compare it here with other galaxies of similar inclination angle and Hubble-type, selected from the WSRT-SINGS survey (Sec. 2.1 and Appendix A). The inclination of these objects favours detection of the magnetic field structure in the disk and possibly in the halo as well. It is known that the field morphologies in these two regions are much different. In galactic disks, usually spiral fields are observed (characterized
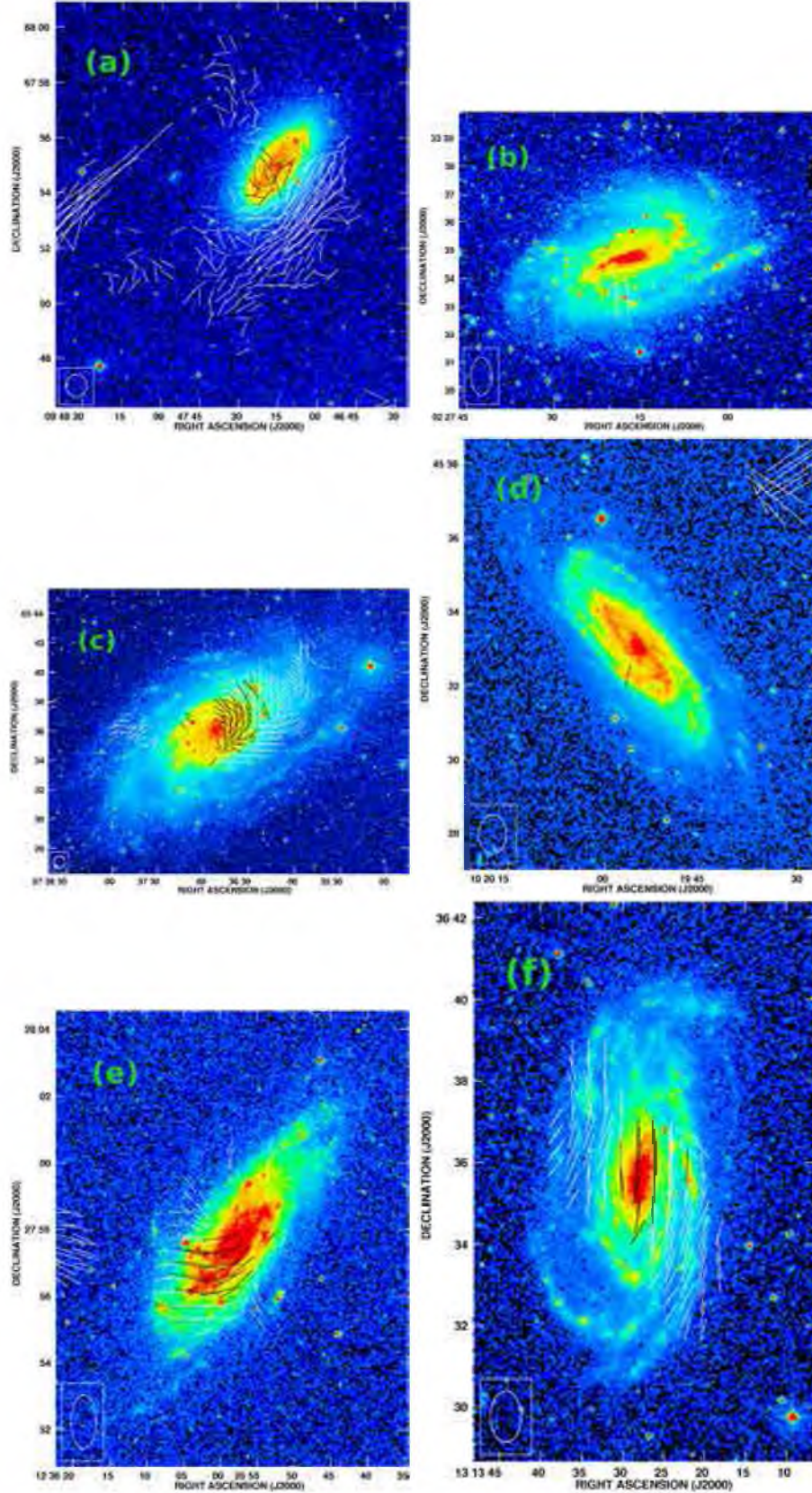
Figure 2.18: Orientations of magnetic field vectors for NGC 2976(a), NGC 0925(b), NGC 2403(c), NGC 3198(d), NGC 4559(e), NGC 5033(f) from the reprocessed WSRT-SINGS data superimposed on the DSS blue images. For all the images the vector of 10" length corresponds to the polarized intensity of about 31.3 μJy/beam.

by various axial symmetries), while in halos, dipolar or quadrupolar morphologies of magnetic field are to be expected (Widrow 2002, see Sec. 1.1).

The immediate conclusion from this comparison is that, despite of similar inclinations and Hubble types of all the objects considered, their field morphologies differ significantly (Fig. 2.18). In particular, hardly any polarized emission was detected in the galaxies NGC 0925 (Fig. 2.18b, Sec. A.1) and NGC 3198 (Fig. 2.18d, Sec. A.3). Their diameters are of 31 and 24 kpc and SFRs of 2.4 and 0.85 $M_\odot$/yr, respectively (Table 2.1). This can suggest that these objects have no strong (detectable with the available sensitivity) regular or even ordered magnetic fields. In the galaxy NGC 2403 (Fig. 2.18c, Sec. A.2), which is most similar to NGC 2976 (a diameter of about 12 kpc, but a higher mass, cf. Table 2.1), a part of a magnetic spiral structure can be easily seen. As it is mentioned in Appendix A.2, the distribution of polarized emission in this object agrees well with the model of magnetic field proposed by Braun *et al.* (2010), which indicates that the large-scale dynamo is at work in it. NGC 4559 (Fig. 2.18e, Sec. A.4) is the only high-mass object (with a HI mass of about 112×10^8 $M_\odot$) studied here for which some extraplanar polarized emission was detected. In NGC 5033, with a linear size of 41 kpc (Fig. 2.18f, Sec. A.5), a distinct spiral magnetic field can be observed. From the distribution of maximum Faraday depth, one can deduce signatures of the large-scale dynamo action in this galaxy. Thus, the magnetic field structure we observe in NGC 2976 does not resemble any of the objects presented. It is also far from that observed typically in dwarf galaxies (cf. Sec. 2.3.1).

2.4.5 Tidal interactions or ram pressure?

The tidal interactions are one of possibilities to account for the magnetic field structure of NGC 2976 discussed above. It is supposed that the object could have been influenced by M 81 in the past, during its passage close to the group centre. At present, NGC 2976 is located south-west of the M 81 group's core. Such an interaction between M 81 and NGC 2976 could have occured more than 1.3 Gyr ago, as it was crudely estimated by Williams *et al.* (2010), assuming that both the galaxies are separated by 148 kpc and their relative velocity is close to the dispersion velocity of the group (of about 110 km s^{-1}). In the high sensitivity maps of distribution of neutral hydrogen, a long strip of HI connecting the object with the group centre, was detected (cf. Fig. 2.3). Hence, some tidal interactions actually could have taken place (Appleton *et al.* 1981, Appleton & van der Hulst 1988, Chynoweth *et al.* 2008). However, there are also some problems with attributing the unusual structure of magnetic field of NGC 2976 to the tidal forces. One of them is its ideally symmetric stellar disk and halo, which can be an apparent indication that the galaxy has not been disturbed for a long time (Bronkalla *et al.* 1992). This makes the tidal interactions scenario more doubtful, yet not impossible, since when considering a structure of magnetic field, one has to keep in mind that it can involve a quite long "memory" of the past events (even from 1 Gyr, see Soida *et al.* 2002 and ref. therein). This memory is longer when compared to the other components of the ISM and the stars. The best instance of a mismatch between a structure of the stellar disk and a structure of the field has been found to date in a flocculent galaxy NGC 4414 (Soida *et al.* 2002). In this high-mass and isolated object, like NGC 2976, a symmetric flocculent disk can be seen, suggesting that it has been in no strong way affected recently. However, the magnetic field contradicts this altogether, since it shows a complicated morphology as well as a strong "RM jump" in the southern part of the object, not expected to occur in non-disturbed galaxies (Soida *et al.* 2002). Usually, the field regularity is regarded as an observable feature to indicate tidal interactions, since it is statistically lower for the interacting objects than for the non-interacting ones (Drzazga *et al.*

2011). However, this is not the case for NGC 2976, for which the field regularity mentioned above (Sec. 2.4.2) has a value found typically in the non-interacting galaxies. It is not too surprising, as there are known obviously interacting galaxies, e.g. NGC 4254, for which field regularity is similar to those observed in the normal objects (Chyży 2008).

These potential difficulties with the tidal interactions scenario suggest that in NGC 2976, ram pressure could also play some role. It constitutes another commonly found mechanism that can lead to a considerable modification of structure of magnetic field in galaxies, while its imprint on magnetic fields differs from that produced by tidal interactions. This mechanism is most often observed in clusters of galaxies e.g. in the Virgo cluster (see, e.g. Vollmer *et al.* 2013). In the galaxy groups, the relative speed of the objects with respect to the surrounding medium and its density (the quantities that the ram pressure depends on) are usually one order of magnitude lower than for the clusters. Recently, Bureau & Carignan (2002) considered the influence of ram pressure on the galaxy Holl, located about 0.5 Mpc from the core of the M 81 group. They argued that for this low-mass object, the density of ambient medium of the M 81 group and its relative velocity are high enough to cause its gas stripping. Thus, Bureau & Carignan argumentation is all the more valid for NGC 2976, which distance to the group centre is lower (and was supposedly even more so in the past). The ram pressure affects only the gaseous component (hence the magnetic field frozen into the plasma), leaving the stellar disk untouched. It also leads to formation of a comet-like distribution of HI in galaxies, as found e.g. in Holl (Bureau & Carignan 2002). In the polarized emission, usually a compressed field is observed at the windward side, forming a polarized ridge and a diffuse extension in the opposite side of galactic disk (see, e.g. Vollmer *et al.* 2010, Vollmer *et al.* 2013). Such an effect could explain the case of NGC 2976, as in fact the structure of its magnetic field resembles much that observed in some of the Virgo cluster spirals, particularly in NGC 4501 (Vollmer *et al.* 2008), which has a similar inclination to the galaxy investigated. Moreover, the distribution of polarized intensity observed in the southern part of NGC 2976 fits well its HI distribution in this region (Fig. 2.19). Such a compatibility was recognized by Vollmer *et al.* (2010) as a true signature of ram pressure.

The ram pressure effect causing stripping of halo gas and/or radial inflow of gas induced by tidal interactions was also considered by Williams *et al.* (2010) to account for the outside-in truncation of star formation, specific for NGC 2976. As shearing motions and compression are both associated with gas inflow, hence like ram pressure, they are able to produce an ordered magnetic field from its random component, while not disturbing the stellar disk. From the spectral index distribution, conclusions concerning the strength of the ram pressure process can be derived. In the galaxy NGC 4522, Vollmer *et al.* (2004) observed a spectral index flattening in the region of maximum of polarized emission caused by interaction with the ICM environment, as well as accelerated particles at this site. Some recent investigations of a sample of 19 Virgo cluster galaxies show that the index flattening is actually observed only in the case of very strong ram pressure (Vollmer *et al.* 2013). Since no such index flattening is to be seen in NGC 2976 (Sec. 2.3.3), this can mean that if there is any ram pressure at all, it must be relatively weak.

The hypothesis of ram-pressure effect in NGC 2976 also has some weak points to be discussed. One of them is the morphology of neutral hydrogen in the southern part of NGC 2976. While being coincident with the PI maximum, it is not so clearly defined as in the other galaxies known to be stripped, e.g. in the Virgo spirals NGC 4501 (Vollmer *et al.* 2008) and NGC 4654 (Soida *et al.* 2006). Also the gas compression in Holl (Bureau & Carignan 2002) seems to be more pronounced than in NGC 2976. Taking into account the present location of NGC 2976 with respect to the group core, it is quite plausible that this object is already past the peak of
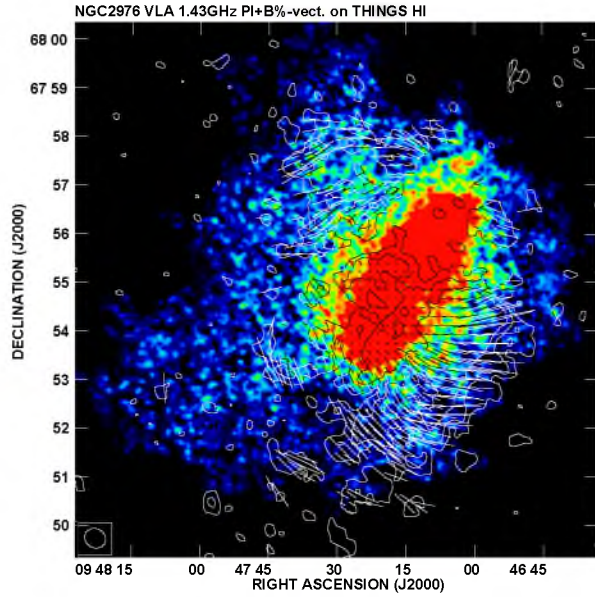
Figure 2.19: Contours of polarized intensity and B-vectors of polarization degree of NGC 2976 at 1.43 GHz (obtained with Robust=1 weighting) superimposed on the HI map (form the THINGS survey, Walter *et al.* 2008). The contour levels are (3, 5, 8) × 9 μJy/beam. The vector of 10" length corresponds to the polarization degree of 12.5%. The polarized intensity map resolution is 26.8" × 23.5" HPBW (the beam position angle is 62 degrees). The HI map resolution is 7.4" × 6.4" HPBW (the beam position angle is 72 degrees).

ram pressure. In fact, Otmianowska-Mazur & Vollmer (2003) define two stages related to the ram-pressure, i.e. a proper stage of ram-pressure and a stage of re-accretion, when gas falls back onto the galactic disk. In their simulations, in the early phases of gas re-accretion the polarized intensity is also enhanced. Moreover, maxima of the gas distribution outside of the disk should occur in this stage, which is actually observed in the case of NGC 2976.

Recent studies of nearby low-mass galaxies show that NGC 2976 fits into the general trend of radio-infrared correlation determined for more massive spirals (Jurusik *et al.* 2014). For Virgo Cluster galaxies exhibiting ram pressure stripping, deviations from the correlation were observed (Murphy *et al.* 2009; Vollmer *et al.* 2013), which can be accounted for by an enhanced radio emission due to ram-pressure induced gas compression. Therefore, in the case of NGC 2976, ram-pressure effects must be weak, not to cause any deviations from the radio-infrared relation, which again suggests the process of gas re-accretion at work.

From the discussion presented above, a following scenario reasonably explaining the structure of magnetic field in NGC 2976 can be proposed. More than 1 Gyr ago the galaxy took part in the gravitational interactions between galaxies in the group centre. At this time, a tidal stripping of the gas occurred, leading to the sharp optical disk observed. This agrees well with the SFH of the object (Williams *et al.* 2010). At present, the remnants of this process can be seen in the form of HI bridges and envelope with possible gas re-accretion. The observed anomalies in the magnetic field configuration result from the "memory" of the past interaction events, further modified by the ram pressure of re-accreting HI gas and magnetized plasma. These processes seem to well account for the compression of magnetic field as well as its azimuthal direction in the southern part of the galaxy (Fig. 2.19a). Detailed 3-D numerical MHD simulations are required to evaluate this scenario. NGC 2976 is a quite suitable object for such simulations, as it does not exhibit any strong density waves to influence the structure of its magnetic field. Moreover, from the observational point of view, sensitive X-ray data are needed to detect hot gas halo around this object. Such a halo, if any, could have a significant impact on effectiveness of the ram pressure process in NGC 2976 and could help to verify the proposed scenario.

2.4.6 Pure dwarf galaxies as a potential sources ot the IGM magnetic fields

The magnetization of intergalactic space is still an open problem in modern astrophysics. Various objects were considered as potential sources of the IGM's magnetic fields. Among them were also dwarf galaxies, which are supposed to have been very numerous in the early Universe. Kronberg *et al.* (1999) within the concept of "boiling universe" suggested that the low-mass galaxies could have efficiently magnetized the IGM, due to their shallow gravitational potential as compared to the typical spirals, hence a lower escape velocity, enabling galactic winds and outflows. This hypothesis was analyzed by Chyży *et al.* (2011) in their investigations of a sample of the Local Group dwarf galaxies. They calculated that the typical dwarfs observed in the nearby Universe could magnetize their surrounding only to the distance of 5 kpc, while not being able to efficiently magnetize any larger volume of the IGM. But how do the pure-disk dwarf galaxies fit these considerations?

As it was shown in Sec. 2.3 NGC 2976 exhibits a strong TP radio emission, extending up to 4.5 kpc (without correction for the inclination angle), thus in a general agreement with Chyży *et al.* predictions based on the assumption that the star formation was continuous, which is also the case for NGC 2976 (Williams *et al.* 2010). While this is not enough to regard NGC 2976 as an effective provider of magnetic field into the IGM, it is worthwhile to note that this galaxy shows also an extended polarized emission of similar extension as the total power one (5 kpc, if measured in the higher sensitivity map, Fig. 2.8). Thus, apart from the random component of magnetic field, NGC 2976 can provide also well-ordered fields, at least within its closest neighbourhood. Moreover, the calculations presented above show that this object is not only able to host a large-scale dynamo but does create favourable conditions to its acting at the level to be typically found in spiral galaxies. This, along with its low mass, makes NGC 2976 one of the best known instances of providers of regular (not just ordered) intergalactic magnetic field. Even in the galaxy NGC 1569, of HI mass similar to NGC 2976, with a huge radio halo extending up to 4 kpc (as estimated in Fig. 1 from Kepley *et al.* 2010), no highly polarized signal was detected at 1.4 GHz (at higher frequencies, a stronger PI is visible, but it is less extended). Therefore, this object is as efficient as NGC 2976 in providing random fields to its neighbourhood, but it is much less efficient in providing ordered and regular fields.

Hence, in order to efficiently magnetize the whole M 81 group with the radius of about 211 kpc (Karachentsev 2005), or at least its central part, more objects from the pure-disk dwarf class are needed. However, finding objects like NGC 2976 is difficult, because its morphology seems to be unique. It does not look like any other known nearby galaxy, featuring a bright sharply-edged disk, which is perhaps just a short-lived stage within its entire evolution (Williams *et al.* 2010). In fact, within the M81 group consisting of 29 galaxies (Karachentsev 2005; or 36 according to Karachentsev & Kaisin 2007), only one galaxy similar to NGC 2976 can be found, i.e. NGC 4605 (Karachentsev & Kaisin 2007). This galaxy also has a well-defined stellar disk and is only slightly larger (with its disk of about 8 kpc) than NGC 2976[7]. In short, the small number of the galaxies of this type makes their significant role for the group's magnetization process rather doubtful. It should be stressed here that this conclusion is based on the observed 1.43 GHz radio envelope only. If to assume that magnetic field of NGC 2976 extends at least to the distance where its HI emission is visible (cf. Fig. 2.3), the volume which the object could effectively magnetize would be much larger. In order to detect the full

---

[7]It should be noted that NGC 4605 was not classified as the M 81 group member in the Karachentsev (2005) work. However, in a later paper Karachentsev & Kaisin (2007) it was included into the sample of the group galaxies studied in Hα.

envelope of synchrotron emission related to such a field, a new generation of radiotelescopes are needed. LOFAR is one of the best suited instruments for this task as it can observe at low frequencies within the range of $30 - 240$ MHz. Thus, it would be able to detect weak magnetic field highlighted by low-energy electrons leaving the disk of NGC 2976.

2.5 Conclusions

For NGC 2976, a pure-disk dwarf galaxy, deep polarimetric observations at 1.43 GHz, 4.85 and 8.35 GHz were performed and then supplemented with re-imaged WSRT-SINGS data for the object and five other comparison galaxies of similar Hubble type and inclination. The radio images obtained were compared with data in other spectral domains, which led to the following conclusions:

- A large total-power and polarized radio envelope surrounding the object was discovered. The thermal fraction estimated using two different methods (giving the complementary results) is about 0.17 (at 1.43 GHz), which is similar to that found in typical spiral galaxies. Also the total magnetic field strength (of about 7μG), its regular component (of about 3μG), and field regularity (of about 0.46) are typical for spiral galaxies, despite low mass of NGC 2976.

- The analysis of rotation measure distribution reveals a coherent, large-scale dynamo-generated magnetic field. The dynamo number calculated for this low-mass galaxy much exceeds the critical value, indicating that in this object, a large-scale $\alpha - \omega$ dynamo can indeed work efficiently. This is quite a surprising result, as for the other dwarf galaxies studied to date usually sub-critical dynamo numbers were obtained.

- Re-imaging of the WSRT-SINGS data for NGC 2976 reveals a much more polarized signal than in the Heald *et al.* (2009) work, which is compatible with the sensitive VLA 1.43 GHz observations. The performed RM Synthesis shows a single point component in the Faraday depth space. It confirms an RM distribution obtained by the classical radio polarimetry from the two frequencies (1.43 GHz and 4.85 GHz). Re-analysis of the sample of five WSRT-SINGS galaxies with Hubble classification (SAc) and inclination (of about 60°), similar to NGC 2976, again enabled to detect much more polarized signal coming from the objects than it was shown by Heald *et al.* (2009). The galaxies under study, while similar to each other, have a wide range of observed morphologies of magnetic fields: from no polarized intensity detected for NGC 0925 and NGC 3198, through extraplanar emission (NGC 4559), to spiral magnetic fields for NGC 2403 and NGC 5033, confirming in general the global field model proposed by Braun *et al.* (2010). However, none of them have magnetic field structure similar to NGC 2976.

- The morphology of magnetic field found in NGC 2976 does not resemble one expected for the pure dynamo action. It features a polarized ridge in the south and a radial extension in the north. This, along with an undisturbed optical appearance of the object, suggests that its magnetic field "remembers" the past tidal interactions with M 81 galaxy (or the centre group galaxies). It is also possible that ram-pressure could have had some impact on the morphology of magnetic field observed in NGC 2976.

- The number of galaxies with a morphology similar to NGC 2976 in the M 81 group is not enough to consider these objects an efficient source of magnetization of the intra-group

41

medium. Such galaxies (taking into account only the extension of their radio emission) can provide ordered (or even regular) magnetic field to their neighbourhood up to distance of 5 kpc.

Chapter 3

IC10

3.1 Introduction

The role of magnetic fields in galactic-scale plasma processes is still poorly known. One of issues not fully understood yet is a generation of large-scale magnetic fields in galaxies by MHD dynamo. While we have already learned quite a lot about the spirals, we do know rather little about the dwarfs (see Sec. 2.1). In particular, the large-scale dynamo efficiency in conditions involving chaotic gas motions and slow rotation, which occur in low-mass galaxies, needs to be investigated.

IC 10 is one of the most interesting objects among such low-mass galaxies. It is the nearest blue compact dwarf (BCD; Richer *et al.* 2001), a member of the Local Group. The object is known to be in a starburst phase, including a lot of Wolf-Rayet stars (Massey & Holmes 2002), which makes for excellent conditions to support a small-scale dynamo action in IC 10 (Chyży *et al.* 2003). However, recognizing conditions required for an effective operation of large-scale dynamo in this galaxy is quite a challenging task, (Siejkowski 2012) due to its relatively small size (of about 1.6 kpc, assuming the distance of 830 kpc, Sanna *et al.* 2008) and a small velocity of rotation (of about 30 km s^{-1}; Wilcots & Miller 1998).

The high star formation activity and low mass of IC 10 favour occurring of galactic-scale winds in this object. There is ever growing evidence that galactic winds could have had a crucial impact on creation of X-shaped extraplanar magnetic field structures found in spiral galaxies seen edge-on (e.g. Tüllmann *et al.* 2000 Soida *et al.* 2011). The question arises if we can expect an analogical field morphology in systems with so simple dynamics as dwarf galaxies? Galactic winds are also of crucial importance when considering the low-mass objects as IGM magnetization sources (see Sec. 2.4.6).

IC 10 has been extensively investigated in a wide range of spectral bands, including the radio domain. The first polarimetric study of the object was performed by Chyży *et al.* (2003). In their high-frequency (10.45 GHz) and low-resolution (73") data they found a mysterious distinct polarized blob in the southern part of the galaxy. The rest of the disk of IC 10 was devoid of polarized signal. Furthermore, it turned out that IC 10 hosted a very strong, mostly random, magnetic field of about 14 μG (Chyży *et al.* 2003). Recently, these low-resolution studies of magnetism of IC 10 were followed up by the high-resolution C band JVLA observations of Heesen *et al.* (2011), which revealed that the polarized blob coincides with a large nonthermal bubble that can be seen in the galaxy (Yang & Skillman 1993).

But despite these detailed studies (Chyży *et al.* 2003; Heesen *et al.* 2011), a number of fundamental questions remain still unresolved. The most important one among them is that of origin of the ordered component of magnetic field discovered in IC 10. In order to address

Table 3.1: Parameters of the VLA observations of IC 10

Band	Obs. Date	Configuration	Integr. time [h]	r.m.s. (TP) μJy/beam	r.m.s. (PI) μJy/beam
L	27 Mar 2004	C	5	28^a	15^a
L	15 Aug 2004	D	4.3		
C	4,28,31 Dec 2001	D	24.2	17^b	6.5^b
X	9,10,14 Feb / 11,12,27 Apr 2003 / 18 Aug 2004	D	37.1	10^b	3.5^b

a - final r.m.s. noise level for the concatenated data from C and D configurations. b - r.m.s. noise levels for the merged VLA and Effelsberg data (see below).

this one as well as the other questions, sensitive multi-band polarimetric observations of IC 10 with the VLA and Effelsberg telescopes were performed. In the next sections I present data reduction procedures and the results obtained, to be further discussed and summarized.

3.2 Observations and data reduction

3.2.1 VLA

IC 10 was observed with VLA in L, C, and X frequency bands (Table 3.1). The observations were performed in the full polarimetric mode using a standard correlator setup. As a phase calibrator source, 0059+581 was used for all configurations and bands. Alternative scanning of 0134+329 or 0518+165 served as an amplitude and polarization angle calibrator. The data reduction was performed in the analogical way as for the galaxy NGC 2976 (see Sec. 2.2.1 for details). The observations in all bands and configurations were first edited and calibrated using calibrators, and then self-calibrated when needed. In the final stage, the data from all the observational sessions for a particular frequency band were combined and self-calibrated again. The obtained r.m.s. noise levels for TP and PI signals are given in Table 3.1.

3.2.2 Effelsberg

IC 10 was also observed with Effelsberg telescope at 4.85 and 8.35 GHz. The observing and data reduction procedures were exactly the same as for NGC 2976 (see Sec. 2.2.2 for details). The procedure of data reduction included editing of individual coverages and then combining them into the final map. All details related to the observations as wel as the obtained r.m.s. noise levels are given in Table 3.2.

As IC 10 has a relatively large angular size (of about $7'$), interferometric observations lead to the missing large-scale structure and underestimated total flux for it. In order to eliminate this effect, I merged data from VLA and Effelsberg at 4.86 and 8.46 GHz. The merging was performed within the Miriad package (Sault *et al.* 1995, task IMMERGE), following the procedures described by Stanimirović (2002). The radio maps obtained in this way for I, Q and U Stokes parameters were used in the further analysis (Sec. 3.3).

Table 3.2: Parameters of the Effelsberg observations of IC 10 at 4.85 and 8.35 GHz

Obs. Freq. GHz	Obs. Date	Num. of col/rows	Total/Good coverages	S_{TP} mJy	S_{PI} mJy	r.m.s. (TP) mJy/beam	r.m.s. (PI) mJy/beam
4.85	2001	51×41	10/8	221.9 ± 2.8	6.3 ± 0.4	0.80	0.14
8.35	2003	33×33	22/18	183.0 ± 3.9	2.5 ± 0.5	0.50	0.072
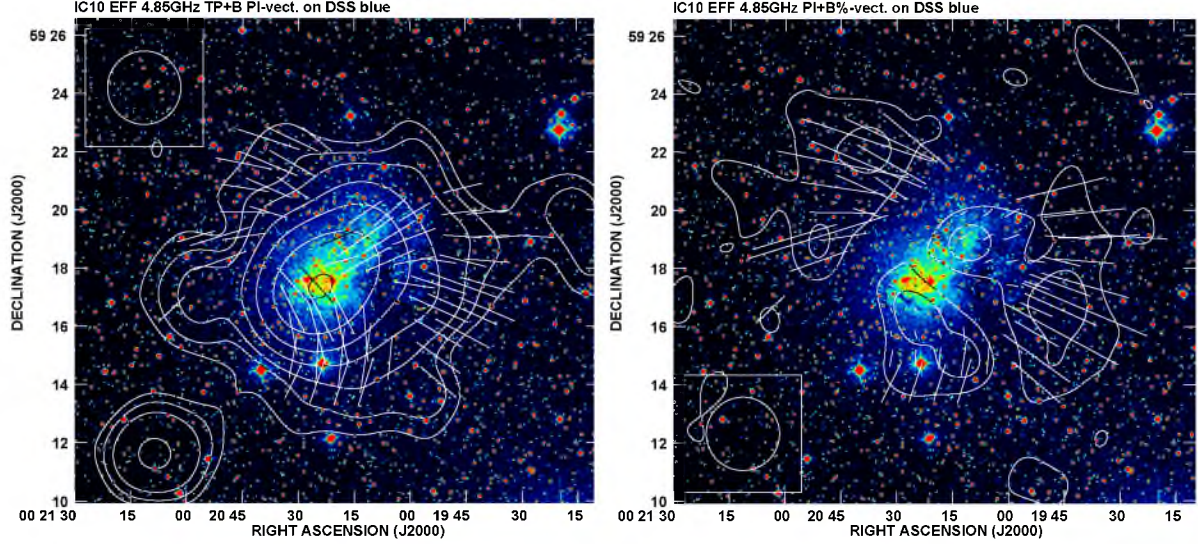
Figure 3.1: Left: Total-power contours and B-vectors of polarized intensity of IC 10 at 4.85 GHz superimposed on the DSS blue image. The contours levels are (-5, -3, 3, 5, 8, 16, 32, 64, 128) × 800μJy/beam. A vector of 10" length corresponds to the polarized intensity of 59 μJy/beam. Right: Contours of polarized intensity and B-vectors of polarization degree of IC 10 at 4.85 GHz superimposed on the DSS blue image. The contour levels are (3, 5) × 140μJy/beam. A vector of 10" length corresponds to the polarization degree of 1%. The map resolution is 151" × 151" HPBW.

3.3 Results

3.3.1 Low resolution data

In figure 3.1 I present the total power map of IC 10 from the Effelsberg observations at 4.85 GHz. The maximum of radio emission corresponds to the bright HII region, well visible in the blue image. Noticeable is also a bright TP emission following the optical disk of the object. The low-level emission (at 3 – 5 noise level) extends far away from the galaxy's body in each direction. The two furthest elongations of the radio emission are background sources (R.A.(J2000.0) $00^h21^m00.79^s$ Dec.(J2000.0) $59°16'59.0"$ and R.A.(J2000.0) $00^h20^m08.73^s$ Dec.(J2000.0) $59°13'27.4"$) visible in the high-resolution NVSS map.

The polarized intensity (Fig. 3.1) is distributed into four major regions. One of them is coincident with the southern part of the bright HII region. Emission at this place was also observed by Chyży et al. (2003) at 10.45 GHz. The directions of B-vectors in both the data sets are similar. However, in 4.85 GHz data an additional "radial" component can also be seen. Another region of polarized intensity corresponds to the disk, with B-vectors aligned with it. A hint of such magnetic field was found by Heesen et al. (2011) in their C-band JVLA
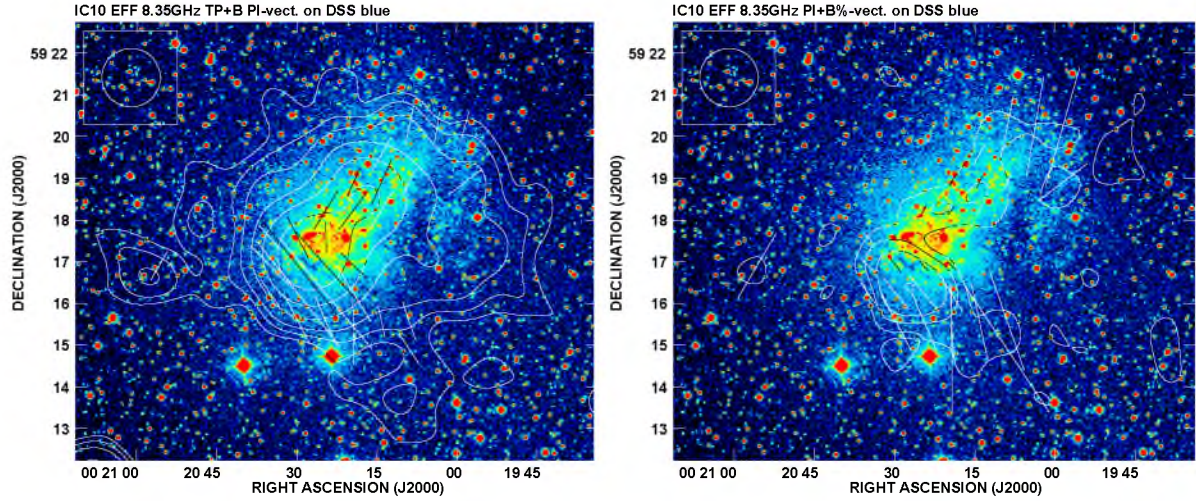
Figure 3.2: Left: Total-power contours and B-vectors of polarized intensity of IC 10 at 8.35 GHz superimposed on the DSS blue image. The contours levels are (-5, -3, 3, 5, 8, 16, 32, 64) × 500μJy/beam. A vector of 10" length corresponds to the polarized intensity of 50 μJy/beam. Right: Contours of polarized intensity and B-vectors of polarization degree of IC 10 at 8.35 GHz superimposed on the DSS blue image. The contour levels are (3, 5, 8, 16) × 72μJy/beam. A vector of 10" length corresponds to the polarization degree of 0.7%. The maps resolution is 84" × 84" HPBW.

observations of IC 10. The last two PI regions are located at the outskirts of the object and have not been known to date. The B-vectors in these regions have mostly radial orientations. The characteristic valley in polarized intensity distribution visible in the eastern part of IC 10 is likely due to the beam depolarization effect.

The total power flux at 4.85 GHz integrated over whole radio extent of the galaxy is 221.9 ± 2.8 mJy (leaving out the two background sources). This is 1.7 times more than the flux measured by Heesen *et al.* (2011) in their interferometric data, not sensitive to extended radio structures. The polarized flux is 6.3 ± 0.4 mJy, which results in a polarization degree of 2.8 ± 0.2 %.

In figure 3.2 a higher resolution (84") TP map of IC 10 from Effelsberg data at 8.35 GHz is shown. Also here the maximum of emission coincides with a bright HII region and the disk of the galaxy. Furthermore, on this map (for which the total power flux measured for IC 10 is 183.0 ± 3.9 mJy) a characteristic, detected by Chyży *et al.* (2003) and Heesen *et al.* (2011), extension of emission to the south-western direction is visible, covering a group of star forming regions. There is no such radio or optical extension on the opposite, northern side of the disk.

In the polarized intensity data (Fig. 3.2) the maximum of emission corresponds to the well-known nonthermal superbubble (Yang & Skillman 1993). The directions of the B-vectors are similar to those observed at 4.85 GHz. Also at 8.35 GHz there is an emission (the polarized flux is 2.5 ± 0.5 mJy) coincident with the optical disk; however, no extraplanar (diffuse) PI signal, such as at 4.85 GHz, is observed here.

3.3.2 High resolution data

The sensitive low-frequency VLA observations of IC 10 at 1.43 GHz reveal a very extended total-power radio emission of the object (Fig. 3.3). The envelope extends to about 1.5 kpc in radius, much further than the optical disk. Note that around the central part of the detected radio

46
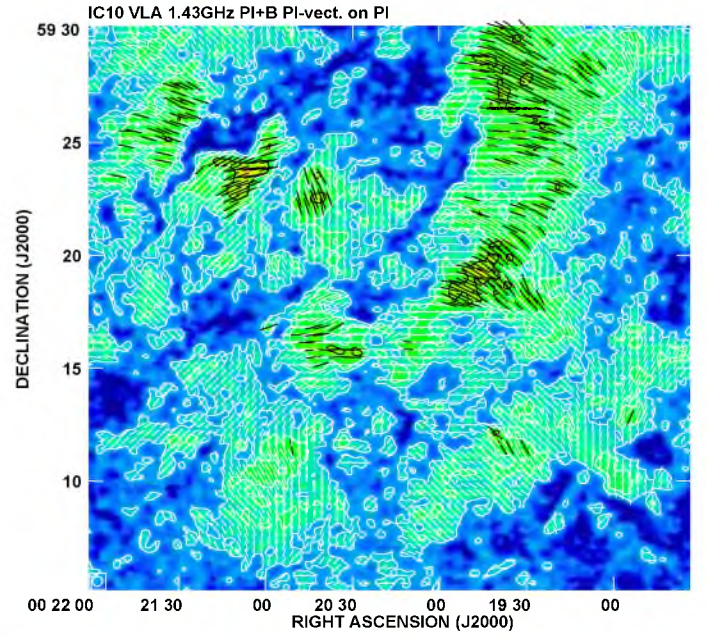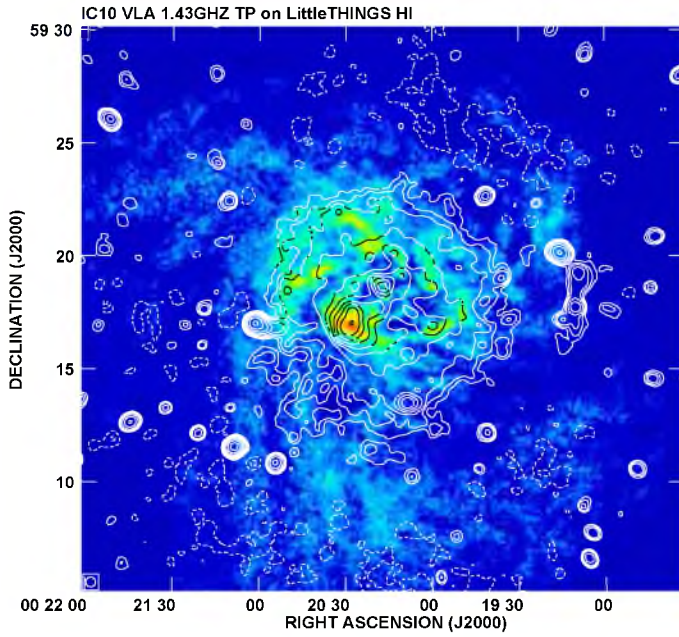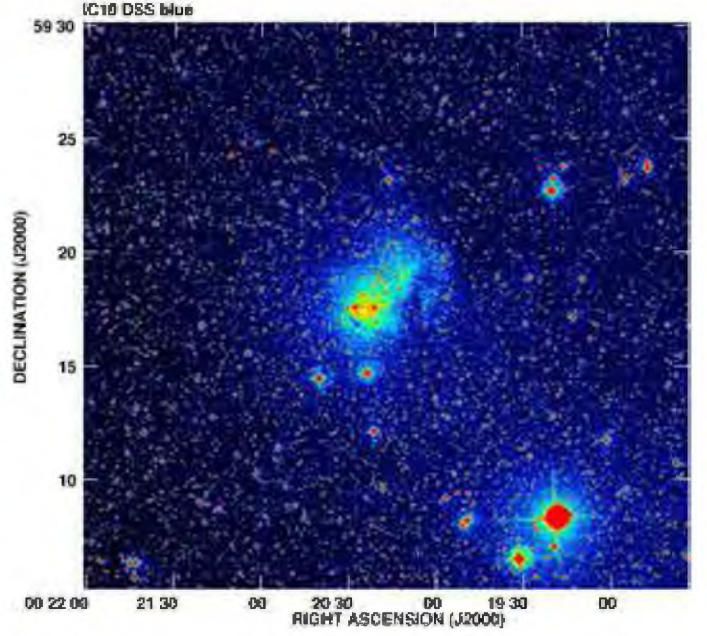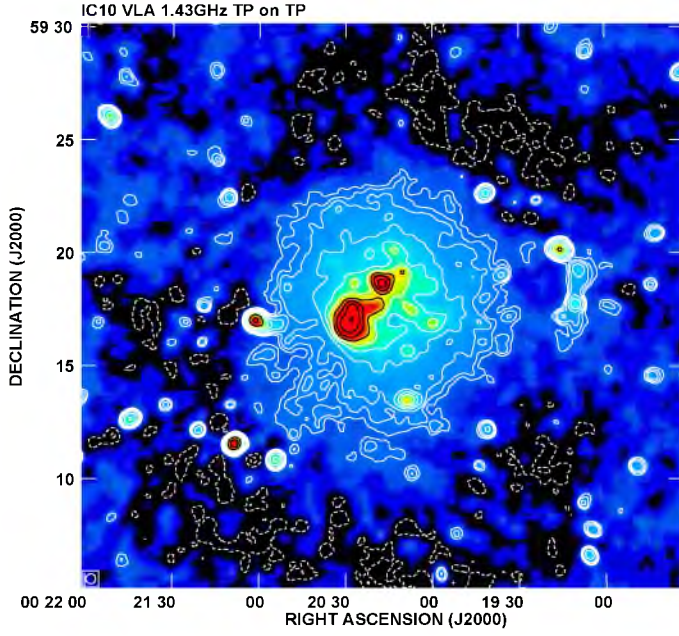
Figure 3.3: Top-Left: Total-power contours of IC 10 at 1.43 GHz superimposed on the total-power image. The contour levels are (-5, -3, 3, 5, 8, 16, 32, 64, 128, 256, 512, 1024) × 28μJy/beam. Top-Right: Blue DSS image of IC 10. Bottom-Left: Total-power contours of IC 10 at 1.43 GHz superimposed on the HI map (Hunter *et al.* 2012). The contour levels are (-5, -3, 3, 5, 8, 16, 32, 64, 128, 256, 512, 1024) × 28μJy/beam. The HI map resolution is 8.44" × 7.45" HPBW, position angle of the beam is 37.38 degrees. Bottom-Right: Contours and B-vectors of polarized intensity of IC 10 at 1.43 GHz superimposed on the polarized intensity map. The contour levels are (3, 5, 8) × 15μJy/beam. A vector of 10" length corresponds to the polarized intensity of 25 μJy/beam. All the images show the same region of the sky. Resolution of 1.43 GHz radio maps is 26.0" × 26.0" HPBW.

47

signal a "negative bowl" is visible, which indicates that due to the so-called missing spacing problem, it is not possible to recover fully the radio flux and structure of the object at this frequency. The total power flux measured at 1.43 GHz for IC 10 is 377.4 ± 6.3 mJy. As there is no optical emission at the distance to which the radio radiation extends, it can be suspected that the observed halo is purely of synchrotron origin. Unlike the high-frequency radio maps (see below), the synchrotron envelope is quite symmetric. In particular, at 1.43 GHz there is no strong emission gradient in the southern part of the giant HII complex. While the synchrotron envelope extends wider than the optical emission, its size is smaller than the extension of neutral hydrogen observed (Fig. 3.3). The HI data reveal some counter-rotating components within the disk as well as a complicated morphology outside of it (Wilcots & Miller 1998). Within the main body of the galaxy the distribution of the radio emission at 1.43 GHz is similar to that of the HI. However, further off the disk, where a network of HI streamers and extensions can be seen, there are no traces of radio signal. Much lower frequency observations are needed (e.g. with LOFAR or WSRT) to determine the full extent of the synchrotron halo in IC 10. Such an emission generated by an old population of CR electrons spiralling along weak magnetic fields cannot be possibly detected by current high-frequency observations.

The distribution of the polarized intensity of IC 10 at 1.43 GHz (Fig. 3.3) is quite unusual. There is a lot of PI emission in the image, but it is not directly related to the object investigated. In fact, the entire primary beam of the telescope is filled with diffuse polarized signal. This, combined with the galactic latitude of IC 10, which is about -3.3 degrees, leads one to suspect that the observed PI possibly comes from the Milky Way. This finding is quite a peculiar one, constituting the strongest manifestation of Milky Way foreground emission in observations of any external galaxy. A hint of additional polarized signal not directly related to the investigated galaxy was found in NGC 7331, which is significantly further off the Milky Way plane (-20.7^o) than IC 10 (Heald et al. 2009). It has been difficult to assess on the basis of the available data if there is actually any PI emission at 1.43 GHz coming from IC 10. New JVLA observations in L-band (1-2 GHz) and application of RM Synthesis method, which for this frequency range would result in a Faraday depth resolution of about 40 rad m^{-2}, could make it possible to address this question.

The total-power high-resolution (18") map from the combined VLA and Effelsberg data at 4.86 GHz superimposed on Hα image is shown in figure 3.4. Comparison of both the images reveals that the TP maxima correspond to the bright HII regions. It can be seen in the south-eastern, central, and western part of the object, where prominent Hα filament is located. Apart from this point-like or barely resolved emission, a more diffuse-like component of radiation is observed in IC 10 as well, filling the entire optical disk of the galaxy and extending further to the north-eastern and south-western directions. However, no such extension is to be seen in the southern part of giant HII region, where the radio emission drops dramatically to the noise level. The point source located around position R.A.(J2000.0): 00^h 20^m 08^s Dec.(J2000.0): 59° $15'$ 42" is likely a background source, to be seen also in the NVSS survey. The TP flux measured in this map is 187.5 ± 2.7 mJy, about 60 mJy higher than the value given by Heesen *et al.* (2011), which can indicate that all the radio emission from the galaxy has been recovered by our observations.

In figure 3.5 a polarized intensity map from the combined VLA and Effelsberg data at 4.86 GHz is presented. The most prominent PI signal found in the object is coincident with the southern part of a giant HII region, where nonthermal blob is located. It was interpreted as a superbubble resulting from about ten supernova (Yang & Skillman 1993) or one hypernova events (Lozinskaya & Moiseev 2007). The B-vectors in this region are oriented perpendicularly to the major axis of the galaxy, subsequently changing to radial orientations. The same could be

IC10 VLA+EFF 4.86GHz TP+B PI-vect. on Halpha

Figure 3.4: Total-power contours and B-vectors of polarized intensity of IC 10 from the combined VLA and Effelsberg data at 4.86 GHz superimposed on the Hα image (Gil de Paz *et al.* 2003). The contour levels are (-5, -3, 3, 5, 8, 16, 32, 64, 128, 256, 512) × 17μJy/beam. A vector of 10" length corresponds to the polarized intensity of about 33μJy/beam. The map resolution is 18.0" × 18.0" HPBW.

IC10 VLA+EFF 4.86GHz PI+B%-vect. on Halpha

Figure 3.5: Contours of polarized intensity and B-vectors of polarization degree of IC 10 from combined VLA and Effelsberg data at 4.86 GHz superimposed on the Hα image (Gil de Paz *et al.* 2003). The contour levels are (3, 5, 8, 16) × 6.5μJy/beam. A vector of 10" length corresponds to the polarization degree of 6.25%. The map resolution is 18.0" × 18.0" HPBW.

observed in the Effelsberg map and in the Heesen *et al.* (2011) data. The degree of polarization is in a range of about 2% to about 25% in this region. The lowest degree of polarization of about 0.5% is coincident with the HII complex. In the rest of the galactic body the polarized intensity distribution is more patchy. Usually these patches are of size of a single beam and they apparently avoid the regions (HII) where massive stars are formed. This is to be expected as the enhanced turbulent motions effectively tangle magnetic field lines in these regions. A similar effect can be observed in galactic spiral arms (e.g. Chyży *et al.* 2007b). The highest degrees of polarization (even as high as 50%) are found where star formation is less enhanced, i.e. at the edges of the galaxy. The polarized flux measured at 4.86 GHz is 4.9 ± 0.6 mJy, which results in the mean polarization degree of 2.6 ± 0.3 %.

In order to obtain a clearer picture of polarized intensity distribution in IC 10, I convolved the PI map presented above to a lower resolution of 45" (Fig. 3.6). Surprisingly enough, it turned out that this galaxy, despite its small linear size, manifests a huge amount of polarized intensity signal, not discovered in the previous studies of the object (Chyży *et al.* 2003; Heesen *et al.* 2011). The detected emission extends far beyond the optical disk. In its furthest extensions, found in the north-eastern and south-western directions, the orientations of B-vectors are radial, suggesting a presence of halo magnetic field, possibly created by some galactic wind (see below). Furthermore, there is also a distinct magnetic field component aligned with op-
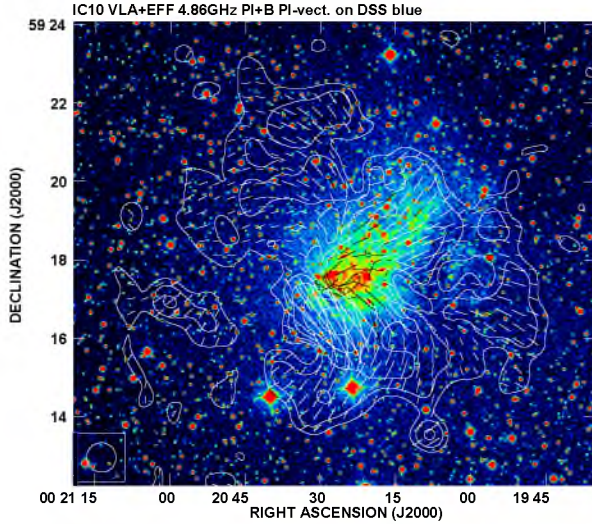
Figure 3.6: Contours and B-vectors of polarized intensity from combined VLA and Effelsberg data of IC 10 at 4.86 GHz convolved to the resolution of 45" and superimposed on the DSS blue image. The contour levels are (3, 5, 8, 16, 32) × 11μJy/beam. A vector of 10" length corresponds to the polarized intensity of about 33 μJy/beam.

tical disk; such a picture is usually to be found in edge-on spiral galaxies (e.g. Soida *et al.* 2011). The distribution of polarized intensity in the neighbourhood of the southern giant HII complex resembles that in the high-resolution image, with the furthest extension of emission to the south-eastern direction.

In figure 3.7 the total-power map of IC 10 at 8.46 GHz is shown. The total-power flux measured at this frequency is 154.0 ± 1.4 mJy. As the map has the highest resolution (about 44 pc) from all the images presented in this chapter, we can see that the multiple signal maxima actually correspond to the individual HII regions. There is also a SW Hα plume, well visible in TP emission, which was observed at the lower frequencies of 1.43 and 4.86 GHz. Apart of the discrete radio sources related directly to the regions where massive stars are formed at the frequency of 8.46 GHz, a more diffuse emission is seen as well. It is much less extended than that observed at 4.86 GHz and mostly related to the southern giant HII complex.

The polarized intensity map of the object at 8.46 GHz (Fig. 3.7) resembles that at 4.86GHz (Fig. 3.5). Here also most of PI signal is found in the region of the nonthermal superbubble. The B-vector orientations in this location roughly agree with those observed at the lower frequency (of 4.86 GHz). They are aligned perpendicularly to the major axis of the galaxy in the northern part and change their direction when passing to the most southern part. The degree of polarization measured in this PI structure ranges from about 2-3% in the N part to about 30% in the S part. So high a degree of polarization can be accounted for by compression related to the superbubble (Heesen *et al.* 2011) or dust feature located to the south from the star-forming region (Chyży *et al.* 2003; see Sec. 3.4.3). Aside from this bright PI signal, also some polarized blobs are observed in the region coincident with the main body of IC 10, with the B-vectors oriented along the object's major axis. The total polarized flux integrated over the entire galaxy at 8.46 GHz is 4.1 ± 0.3 mJy (which gives a mean polarization degree of 2.6 ± 0.2 %). In a similar manner as in the 4.86 GHz data, the PI emission at 8.46 GHz apparently avoids the bright HII regions in the disk. However, not all PI distribution appearing in 8.46 GHz map has its counterpart at 4.86 GHz. An example of such a polarized structure can be found around a position of R.A.(J2000.0): $00^h 20^m 20^s$ Dec.(J2000.0): $59^o 18' 04"$, which indicates that the Faraday depolarization effects can play an important role in IC 10 (see Sec. 3.4.2). The degree of polarization observed in the main body of IC 10 is usually about 10% (or less). Due to the high sensitivity of the presented map at 8.46 GHz (3.5 μJy/beam – which is the highest sensitivity image obtained for this object to date), it is also possible to confirm a real character of the PI structures off the stellar body of the galaxy seen for the first time in the 4.86 GHz
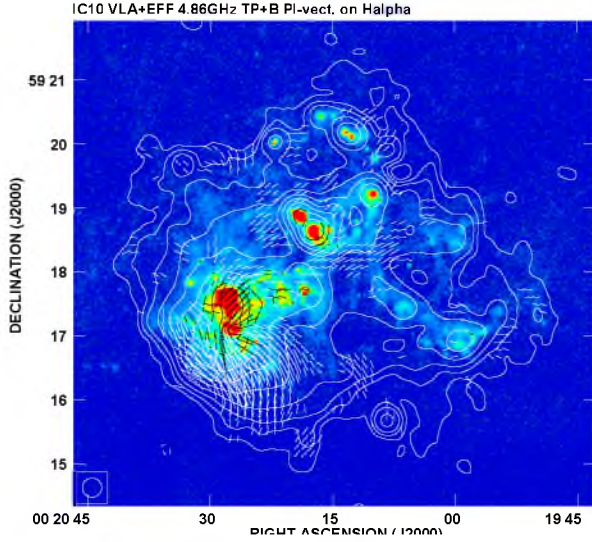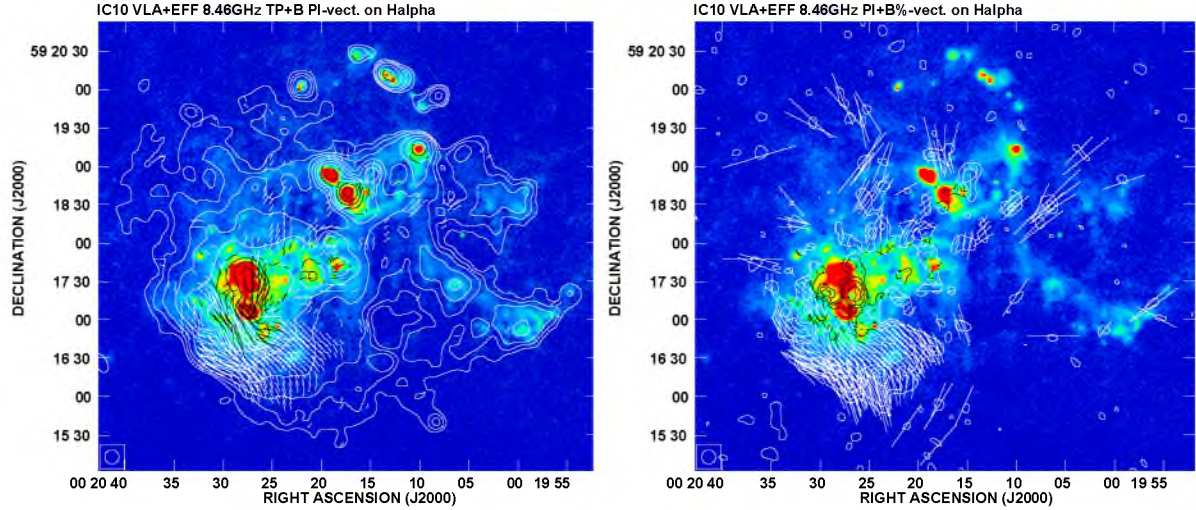
Figure 3.7: Left: Total-power contours and B-vectors of polarized intensity of IC 10 from combined VLA and Effelsberg data at 8.46 GHz superimposed on the Hα image (Gil de Paz *et al.* 2003). The contour levels are (-5, -3, 3, 5, 8, 16, 32, 64, 128, 256, 512, 1024) × 10μJy/beam. A vector of 10" length corresponds to the polarized intensity of about 25μJy/beam (not corrected for the prim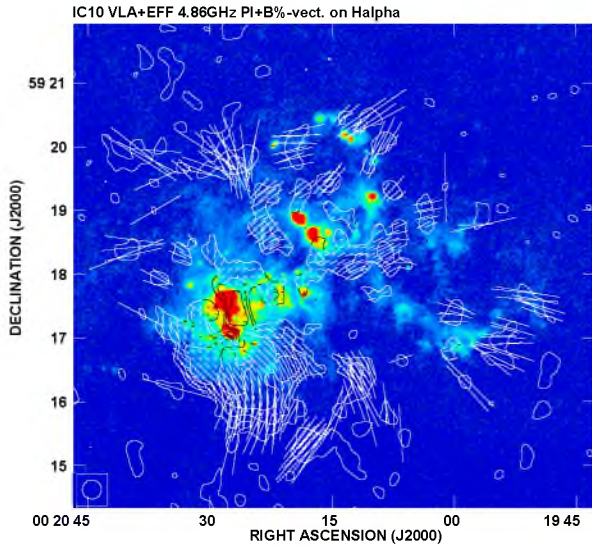ary beam attenuation). The map resolution is 11.0" × 11.0" HPBW. Right: Contours of polarized intensity and B-vectors of polarization degree of IC 10 from combined VLA and Effelsberg data at 8.46 GHz superimposed on the Hα image (Gil de Paz *et al.* 2003). The contour levels are (3, 5, 8, 16) × 3.5μJy/beam. A vector of 10" length corresponds to the polarization degree of about 7.14%. The map resolution is 11.0" × 11.0" HPBW.

data (Fig. 3.5). Despite the fact that the signal is much weaker here, the B-vector orientations roughly agree between both the data sets.

3.3.3 Distribution of spectral index

IC 10 is known to manifest a significant thermal fraction of radio emission (50% at 10.45 GHz; Chyży *et al.* 2003). In figure 3.8 I present a map of spectral index distribution for this object to confirm this statement. The map was computed in a pixel-by-pixel manner between 1.43 GHz (imaged with robust of 0) and 4.86 GHz (from the combined VLA and Effelsberg data). Both the maps were first convolved to the common resolution of 19". As a radio brightness threshold in computations, a somewhat conservative limit of 5 r.m.s. noise levels was used. As it can be seen, small (about -0.1 – -0.2) spectral indices correspond well with the bright and compact HII regions, which can indicate that they are dominated by thermal emission. Similar flat spectra are also observed in a southern Hα plume. Analogical findings were made by Heesen *et al.* (2011) in their high-resolution spectral index map obtained with the multi-frequency synthesis method. However, Heesen *et al.* map was limited just to the galaxy's brightest part. In the spectral index map presented in this chapter for the first time, a more diffuse component of radio emission, located mainly in between star-forming regions, can be discerned, which is characterized by spectral indices of about -0.5, indicating a nonthermal diffuse radiation mixed with thermal emission. When going towards the edges of the galaxy, the spectral index steepens to a value of -1, which means that the relativistic electrons lose their energy there. The same does not apply to the region of the nonthermal superbubble, where the index reaches value of about -0.7, which is in conflict with findings of Heesen *et al.* (2011), who reported values from -1 to -1.2 at this place.
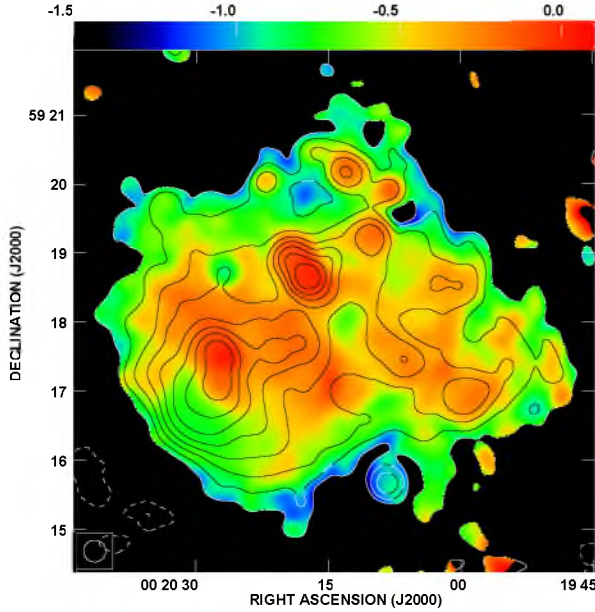
Figure 3.8: Radio spectral index distribution between 1.43 (Robust 0) and 4.86 GHz in IC 10 (colours) from combined VLA and Effelsberg data. Both the maps of total intensity were convolved to a common beam of 19". The contours represent total power map at 4.86 GHz, they levels are: (-5, -3, 5, 8, 16, 32, 64, 128, 256, 512) × 17 μJy/beam.

3.3.4 Distribution of Rotation Measure

In the present study, for the first time, I obtained a map of rotation measure distribution in IC 10 (Fig. 3.9). The map was calculated using the observations at 4.86 GHz and 8.46 GHz convolved to the common beam (18"). The maps of polarization angles at both the frequencies were cut at the level of 4 × r.m.s. in PI. The typical uncertainty of RM for the signal-to-noise ratio of 4 is 67.5 rad m^{-2} (for a higher S/N, the uncertainty gets lower). In the southern polarized region RMs are as high as -200 rad m^{-2}. There can be also discerned a characteristic pattern of approximately N-S oriented "belts", where the rotation measure alternately changes value from minus several to less than -100 rad m^{-2}. In the 18" map not much RM distribution can be seen in the disk. Only a couple of spots with very low RMs (-100 – -300 rad m^{-2}) were detected.

In order to enhance the PI emission from the main galactic body, I computed, in an analogical way as above, also an RM distribution map but with a resolution of 30" (Fig. 3.9). In this map more PI emission from the disk is actually observed and the rotation measures are here lower than those observed in the southern polarized region (the large RMs in the most southern location, Dec(J2000.0) < 16°, are due to the proximity of the primary beam border of the 8.46 GHz data).

Now there arises a question of how much the Milky Way contributes to the RM observed within IC 10? As it has been already mentioned above, the object investigated is located almost in the Galaxy's plane. Unfortunately, there are no nearby polarized point source(s) in the analysed radio data, which could be of help in estimating the Milky Way's RM contribution. From the all-sky rotation measure distribution map (Johnston-Hollitt *et al.* 2004) I found that for the location of IC 10 (Gal. Long.: 119.0^o, Gal. Lat.: -3.3^o), typical RM are larger than -50 rad m^{-2} (likely about -25 rad m^{-2}). The Galaxy's RM estimates show that it possesses non-zero rotation measures, indicating regular magnetic fields oriented mostly away from the observer. The discovery of large regions of systematic Faraday rotation in IC 10 sheds a new light on generation and evolution of magnetic field in this object. It also challenges current interpretations of magnetic field in dwarfs (Chyży *et al.* 2003); this will be further investigated in section 3.4.4. The findings could be confirmed by future spectro-polarimetric observations (preferably at low radio frequencies) with an application of rotation measure synthesis, which would allow to separate PI emission coming from the Milky Way from that of IC 10.
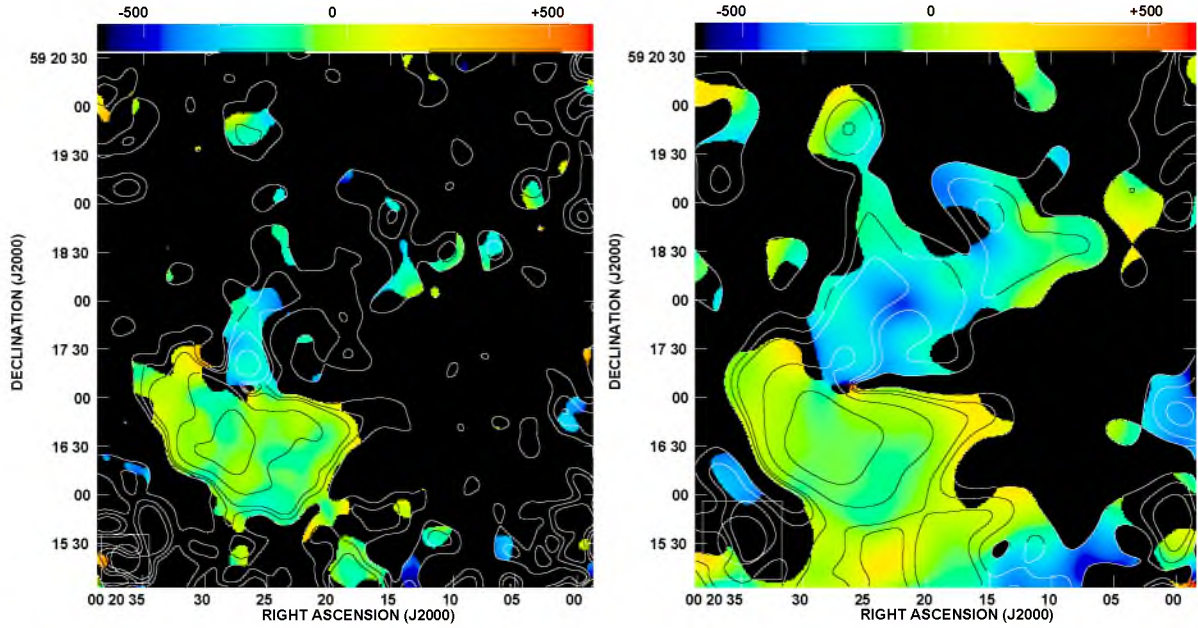
Figure 3.9: Left: Distribution of Faraday rotation measure (in $\mathrm{rad\,m^{-2}}$, not corrected for the foreground RM) in IC 10 (colours) from the data at 4.86 and 8.46 GHz. The contours represent the polarized intensity map at 8.46 GHz, the levels are: $(4, 6, 8, 16, 32) \times 5\mu\mathrm{Jy/beam}$. The map resolution is 18". Right: Distribution of Faraday rotation measure (in $\mathrm{rad\,m^{-2}}$, not corrected for the foreground RM) from the data at 4.86 and 8.46 GHz in IC 10 (colours). The contours represent the polarized intensity map at 8.46 GHz, the levels are: $(4, 6, 8, 16, 32) \times 8\mu\mathrm{Jy/beam}$. The map resolution is 30".

3.4 Discussion

3.4.1 Magnetic field strength

In this section, some estimates of magnetic field strength (cf. Sec. 1.3.1) in IC 10 are presented and analysed. For this purpose, the combined VLA and Effelsberg data at 4.86 GHz were used. The mean total-power radio brightness was determined from the regions of galaxy where S/N ratio was higher that 3. The thermal fraction of radio emission and nonthermal spectral index were taken from Chyży et al. (2003), where $f_{th} = 52\%$ (rescaled to the frequency of 4.86 GHz) and $\alpha_{nth} = 0.55$. The disk thickness, corrected for inclination angle (of 35 degrees[1]), was assumed to be 1 kpc. The calculations of magnetic field strength were performed with the standard assumption of energy equipartition between magnetic field and CRs, and the proton-to-electron ratio of 100 (Beck & Krause 2005), yielding B_{tot} of $13.5 \pm 4.1\,\mu$G (Table 3.3). The obtained value is very similar to the estimations of Chyży et al. (2003), while slightly higher (but still in the range of estimated uncertainty) than 2.64 GHz estimations of Chyży et al. (2011). So strong a total magnetic field is not typical for dwarf galaxies (e.g. Chyży et al. 2011); even in spirals, weaker magnetic fields are usually observed. Only in the galaxies where star formation processes are much enhanced, such field strengths have been found (e.g. Drzazga et al. 2011).

To be able to draw some conclusions about the efficiency of generation of ordered magnetic field in IC 10, I calculated the field regularity (see Sec. 2.4.2 for definition), following

---

[1]This is an average between HyperLeda database (http://leda.univ-lyon1.fr/) and the value given by Hunter et al. (2012).

53

Table 3.3: Magnetic field strengths of IC 10

Region	B_{tot} μG	B_{reg} μG	Field regularity
whole galaxy	13.5 ± 4.1	2.3 ± 0.7	0.17 ± 0.07
northern outskirts	9.1 ± 2.8	3.2 ± 1.0	0.38 ± 0.17
southern outskirts	10.3 ± 3.1	3.0 ± 0.9	0.30 ± 0.13
southern giant HII complex	24.5 ± 7.5	2.2 ± 0.6	0.09 ± 0.04

estimation of ordered and random field components. For B_{ord} I obtained $2.3 \pm 0.7\,\mu$G and $B_{ran} = 13.3 \pm 4.0\,\mu$G. This gives a field regularity of 0.17 ± 0.07 (Table 3.3), which is much lower than the canonical value of 0.5, typically observed in spiral galaxies (cf. Sec. 2.4.2). Again, similarly as in the case of B_{tot}, this value much resembles the mean field regularity of 0.27 ± 0.09, estimated for a sample of interacting galaxies (Drzazga et al. 2011), which can indicate that the total magnetic field in IC 10 is more efficiently produced (by enhanced action of a small-scale dynamo) than in the normal spiral galaxies.

In estimating the mean magnetic field strength above, it was assumed that synchrotron cooling dominates CR electrons energy losses in IC 10. But, is this actually the case for the galaxy's outskirts, where a low-level radio emission is observed? Another process that can be responsible for cooling of relativistic electrons is the inverse Compton scattering, which dominates the synchrotron losses when the total magnetic field strength is weaker than $3.25\,\mu$G $(1+z)^2$ (Beck & Wielebinski 2013). The estimation of mean radio brightness at 4.86 GHz in two low-level radio emission regions (to the north and to the south) of the object using the above assumptions gives magnetic fields strengths of about $10\,\mu$G (Table 3.3), which is well above the limit. For the sake of comparison, the magnetic field in the region of the southern giant HII complex is about $25\,\mu$G (Table 3.3). Both these values, one for the galaxy's outskirts and one for its brightest radio part, are normally found in actively forming massive stars dwarf (Kepley et al. 2010; Kepley et al. 2011) and spiral galaxies (Chyży 2008; Chyży & Buta 2008). One can calculate that to be able to detect the field of $3.25\,\mu$G with the 4.86 GHz data and resolution of 18", a nonthermal brightness as small as $2\,\mu$Jy/beam is needed, which is much below the sensitivity available in this work (Table 3.1).

3.4.2 Distribution of nonthermal emission

Distribution of nonthermal emission is of great importance when investigating magnetic fields in galaxies. Using information about thermal radiation based on the Hα map from Chyży et al. (2003), I calculated the distribution of nonthermal radio emission in frame of IC 10 by subtracting the thermal emission from the total-power one. The calculations were performed for the high-resolution data at 4.86 and 8.46 GHz (Fig. 3.10).

The nonthermal emission fills almost the entire body of the galaxy, similarly as in the spiral galaxies (e.g. Chyży et al. 2007a), clearly dominating in the region of the nonthermal superbubble introduced by Yang & Skillman (1993). There is also a strong pointlike source (presumably a background one) of the nonthermal emission located at the position of R.A.(2000.0): $00^h 20^m 17^s$, Dec.(2000.0): $59^o 18' 40"$. When compared to the total-power emission, the nonthermal radiation is clearly less symmetric. There is an extension visible in the SW direction, following the bright ridge of HII regions, which can suggest that similarly as in spiral galaxies, mostly
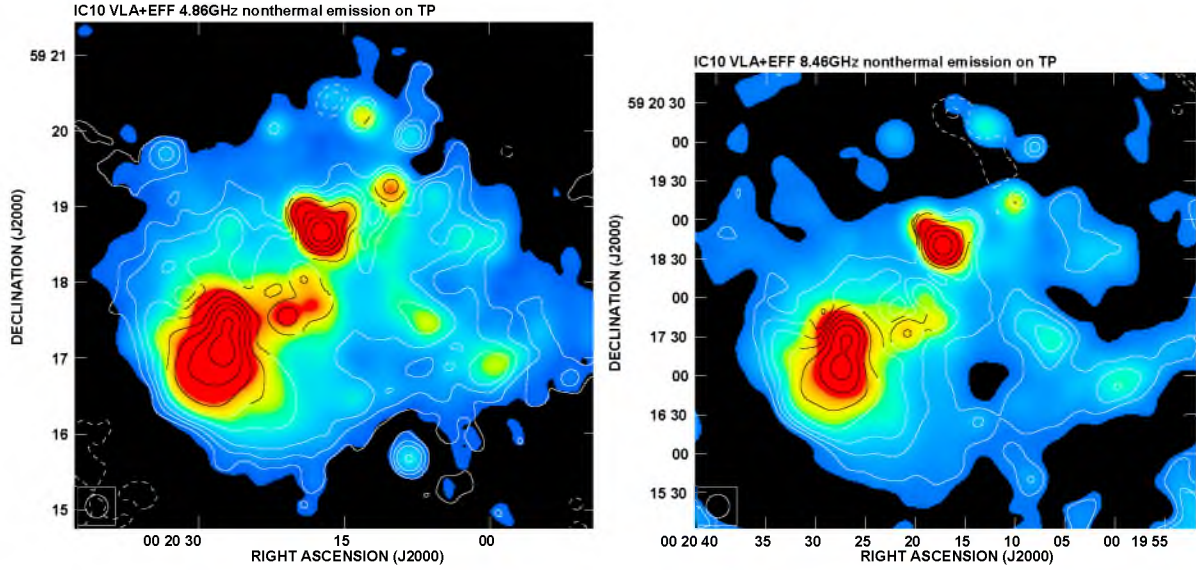
Figure 3.10: Left: Distribution of nonthermal radio emission in contours superimposed on the total power radio emission at 4.86 GHz in IC 10. The contours levels are: (-5, -3, 3, 5, 8, 16, 32, 64, 128, 256) × 25μJy/beam. Right: Distribution of nonthermal radio emission in contours superimposed on the total power radio emission at 8.46 GHz in IC 10. The contours levels are: (-5, -3, 3, 5, 8, 16, 32, 64, 128) × 50μJy/beam. The maps resolution is 18".

random magnetic fields are generated by a small-scale (turbulent) dynamo in these areas (see Table 3.3). Such a correlation between the HII and radio emissions was observed in spiral arms of other galaxies (e.g. Chyży *et al.* 2007a). The NE part of the galaxy is, quite surprisingly, devoid of diffuse nonthermal emission, which is seen at both the radio frequencies discussed here. This can be accounted for by the fact that in this part of galaxy there are less HII regions, and thus less sources able to produce CRs, which in turn indicates an older population of relativistic electrons (coming from the central part of the disk) able to produce radio emission at high frequencies. Note that the 1.43 GHz radio emission dominated by the nonthermal component is more symmetric, which supports this explanation.

Having the distribution of nonthermal emission, it was also possible to calculate a distribution of nonthermal degree of polarization (Fig. 3.11). The values obtained, mostly for the southern polarized region, range from < 1 % to about 55 % at 4.86 GHz. The lowest values (< 10 %) correspond to the giant HII region in the southern part of the object. Similar values are typically observed in spiral arms – sites of massive star formation in spiral galaxies (Beck & Wielebinski 2013). It can be explained by enhanced turbulent motions in such regions. In the rest of polarized blob region, higher degrees of polarizations are found with the maximum (of about 30-40 %) located in its the most southern part. In the galaxy's disk, the typical degree of polarization is around 10-20 %, with its maximum at the outskirts of disk reaching > 40 %.

A similar pattern of distribution of nonthermal degree of polarization (ranging from from < 1 % to about 35 %) can be observed at 8.46 GHz (Fig. 3.11). The differences in polarization degrees between 4.86 and 8.46 GHz could be due to depolarization effects. Aside from the instrumental one, there is also Faraday depolarization defined as $DP = p_{4.86}/p_{8.46}$, where $p_{4.86}$ and $p_{8.46}$ are nonthermal degrees of polarization at 4.86 and 8.46 GHz (see Sec. 2.3.4). Like in the case of degree of polarization, also depolarization has the lowest values in the area roughly coincident with the huge southern HII complex (Fig. 3.12). Outside the complex, the depolarization values are similar as for spirals (see e.g. Chyży 2008); they range from about

55
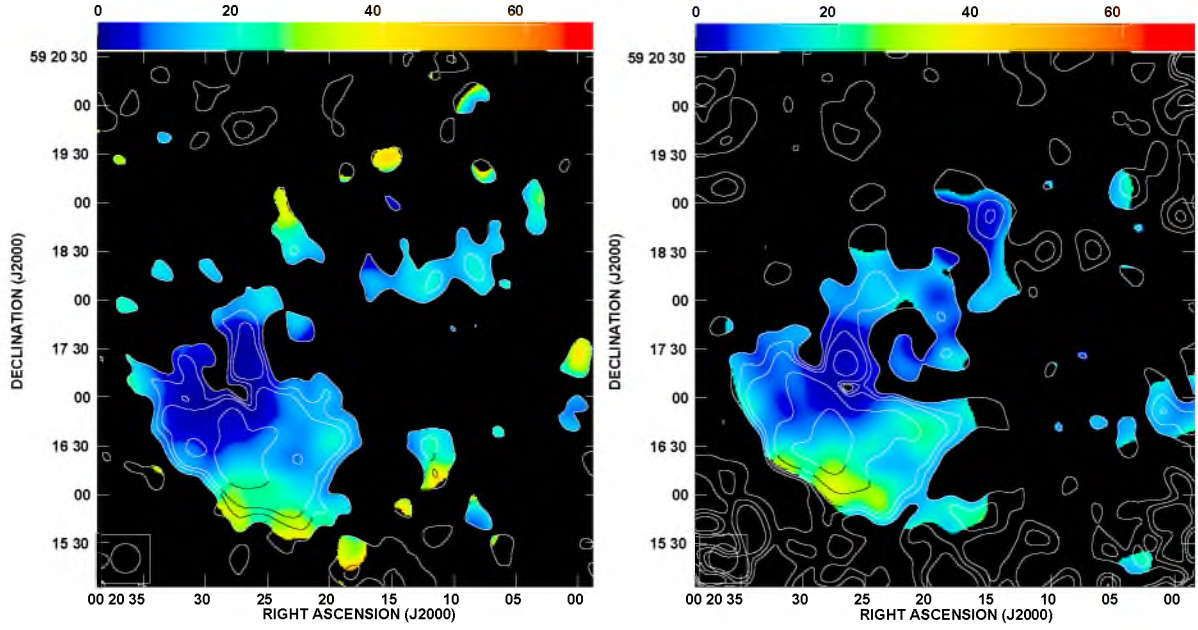
Figure 3.11: Left: Distribution of nonthermal polarization degree (in %) in IC 10 at 4.86 GHz. The contours represent polarized intensity at the same frequency, their levels are: (4, 6, 8, 16) × 6.5μJy/beam. Right: Distribution of nonthermal polarization degree (in %) in IC 10 at 8.46 GHz. The contours represent polarized intensity at the same frequency, their levels are: (4, 6, 8, 16, 32) × 5μJy/beam. The maps resolution is 18".
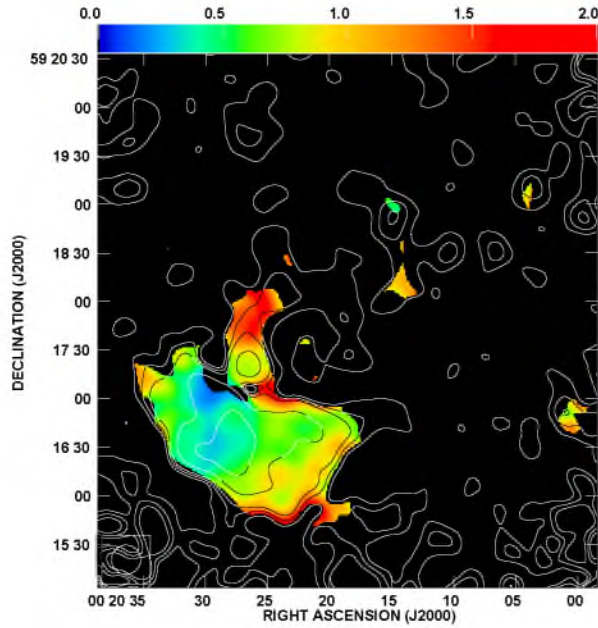
Figure 3.12: Distribution of Faraday depolarization computed between 4.86 and 8.46 GHz for IC 10. The contours represent polarized intensity at 8.46 GHz, their levels are: (4, 6, 8, 16, 32) × 5μJy/beam. The map resolution is 18".

0.6 to about 0.9. It is worthwhile to note that the degree of polarization is also higher off the HII region, which could suggest that we have a Faraday-thin region here. Such Faraday-thin regions were observed e.g. in the southern and western parts of galaxy NGC 4254 (Chyży 2008).

3.4.3 Magnetic field structure

As it was shown in section 3.3, IC 10 manifests a strong polarized signal extending far off its stellar disk (Fig. 3.6). In the NE part of the object, the B-vectors apparently form an elongated and curved structure. A similar field curvature can be seen in the opposite direction. There is also a component of B-vectors closely aligned with the galaxy optical disk. As the vectors orientations at 8.46 GHz (where the Faraday effects are smaller) are generally like these at 4.86 GHz, it can be that they in fact represent closely the true directions of magnetic field. Keeping this in mind, one can notice that the whole B-vectors picture of the outer disk part of IC 10 resembles the X-shape – a magnetic field structure observed commonly for edge-on spiral galaxies (see, e.g. Tüllmann et al. 2000; Soida et al. 2011). It is much surprising, as such a structure is found for the first time in a dwarf galaxy, with no spiral density waves. The X-shape structures observed so far in galaxies are likely due to action of a large-scale dynamo and/or disk outflows (Beck & Wielebinski 2013; Ferriére & Terral 2014, see Sec. 3.4.5). The case of IC 10 shows that this process can occur also in a low-mass starbursting dwarf.

The only polarized structure for which the B-vector directions do not fit exactly into the X-shape picture is the polarized blob in the southern part of the object. In figure 3.13 directions of magnetic field vectors (B-vectors at 4.86 GHz corrected for Faraday rotation computed between 4.86 and 8.46 GHz) are shown. The morphology of B-field could be traced only within this southern polarized blob. The general distribution of orientations of the vectors resembles much the low-resolution and high-frequency results (almost Faraday-free) of Chyży et al. (2003). In the high-resolution data presented here, magnetic field is closely aligned with the characteristic dust lane visible to the south from the HII complex, which confirms earlier suspicions of Chyży et al. (2003). It is possible that RM is significantly different in this region or, more likely, that some additional physical processes are at work there. Quite unclear is also an origin of enhanced polarized emission coming from the blob. Comparing the figures 3.4 and 3.5, one can recognize that the PI and TP maxima do not correlate, thus compression or magnetic field stretching have to take place in this area. These two processes producing a net ordered magnetic field from a random one are common in the interacting galaxies and have been observed e.g. in the Antennae system (Chyży & Beck 2004). In IC 10, field compression by the expanding superbubble was suggested by Heesen et al. (2011) to account for the enhanced PI emission in the southern part of the object. Another process that could lead to field ordering is accretion of primordial gas, proposed to explain the complicated HI morphology of the object (Wilcots & Miller 1998). However, following the most recent investigations of Nidever et al. (2013), IC 10 is likely gravitationally interacting with another dwarf galaxy, which could have resulted in modifying its magnetic field morphology. Spectro-polarimetric observations in a wide range of frequencies are definitely needed to obtain better information on rotation measure (Faraday depth) within the galaxy and thus also on orientations of its magnetic field, which would allow to draw more robust conclusions about any external agents acting in IC 10.
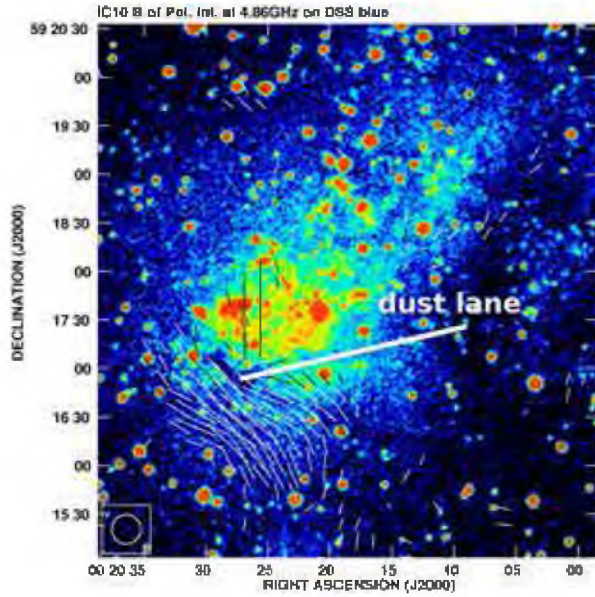
Figure 3.13: Magnetic field vectors of polarized intensity (from the combined VLA and Effelsberg data of 18" resolution) of IC 10 at 4.86 GHz superimposed on the DSS blue image. A vector of 10" length corresponds to the polarized intensity of about $38\,\mu$Jy/beam. The position of strong dust lane is indicated.

3.4.4 Generation of magnetic field

It is possible that IC 10 possesses a regular magnetic field (see Sec. 3.3.4). In order to determine if it could have been generated by the large-scale dynamo, I calculated the dynamo number according to the equation 2.3. In calculations, the velocity of rotation was assumed to be 30 km s^{-1} at a distance of 0.8 kpc, where the rotation curve is flat (Wilcots & Miller 1998), giving a shear ratio of 38 km s^{-1} kpc^{-1}. The other parameter that the dynamo number depends on is the velocity of turbulent motions approximated by the velocity dispersion. However, the velocity dispersion in IC 10 is poorly known. According to Wilcots & Miller (1998), it is about 30–40 km s^{-1} for its central disk part, which yields a dynamo number $|D| \sim 4$. When one assumes (for the sake of comparison) a somewhat less probable value of dispersion velocity of 8 km s^{-1} from Mateo (1998), then the dynamo number will be about 50, which much exceeds the critical dynamo number. Thus these crude estimations (limits) do not provide any conclusive answer.

The recent simulations of CR-dynamo in dwarfs performed by Siejkowski (2012) show that the minimum velocity of rotation needed for efficient dynamo action (at a level comparable to spirals) is about 60 km s^{-1}. For the galaxies rotating with a velocity of about 30 km s^{-1}, their dynamo efficiency depends also (apart from shear) on other parameters like dark matter distribution, gas temperature, and supernova frequency modulation (Siejkowski 2012). Thus, according to these simulations, it cannot be excluded that in IC 10 the CR-dynamo is not at work. However, the time scale for developing large-scale magnetic fields in this case is problematic. Contrary to fast rotating spiral galaxies, the dynamo action is much slower in slowly rotating dwarfs like IC 10 (Arshakian *et al.* 2009). The e-folding time for magnetic field increases to 800-1700 Myr (Siejkowski 2012). For comparison, in NGC 2976 which rotates with a speed higher than 60 km s^{-1}, the e-folding growth time of magnetic field is only about 400 Myr. Therefore, it is not certain if coherent magnetic fields in IC 10 could have had enough time to develop.

3.4.5 Magnetized winds

The morphology of total power and polarized emission presented in section 3.3 suggests that galactic winds can play an important role in IC 10. In order to test this hypothesis, I estimated the bulk speed of CREs (cosmic–ray electrons) transport into the halo and then compared it with

58

the escape velocity of the object. The escape velocity can be approximated by the maximum velocity of galactic rotation: $v_{esc} \cong \sqrt{2} v_{max}$. Taking v_{max} of 30 km s^{-1} (Wilcots & Miller 1998) one gets v_{esc} of 40 km s^{-1}. In estimations of the bulk speed, one of the methods presented by Heesen *et al.* (2009) was used. In this approach, the bulk speed v is defined as ratio of CR electrons' scale height h_e and their lifetime t_e. The value of h_e can be derived from the synchrotron scale height (h_{syn}, see Heesen *et al.* 2009):

$$h_e = \frac{3 + \alpha_{nth}}{2} h_{syn} \tag{3.1}$$

where α_{nth} is the nonthermal spectral index, which for IC 10 is 0.55 (Chyży *et al.* 2003).

h_{syn} for IC 10 was calculated by fitting two-component exponential disk models (thin and thick disks, see e.g. Dumke *et al.* 1995) to the slices of the object's radio emission, obtained by averaging radio map in 3× beam size (of 19", 229 pc) stripes oriented perpendicularly to the main axis of the galaxy taken from HyperLeda database and then corrected for inclination. The results for 1.43 GHz and 4.86 GHz data are given in Table 3.4 and in figures 3.14 and 3.15. Note that the derived scale heights of the thin disk are just upper limits, due to finite resolution of observations. Such a beam smearing effect is marginal in case of the thick disk. It was not always possible to obtain a physical fit for the data; in these cases only one component (thick) disk was fitted and presented in Table 3.4.

The obtained (upper limits of) scale heights of thick disk at 1.43 GHz (Table 3.4) are only slightly smaller than the average value of 1.7 kpc found for NGC 253 at the same frequency (Heesen *et al.* 2009). This is quite surprising as IC 10 is a dwarf galaxy, several times smaller than NGC 253. While at 4.86 GHz the model fits are of lower quality, also here similar conclusion can be drawn. This result indicates that similar generation and propagation processes are at work in dwarf and large galaxies.

In estimating a bulk speed of CR electrons, I assumed that these particles lose their energy only through synchrotron radiation, so $t_e = t_{syn}$. This implicates that the derived values of v should be treated only as a lower limit. The t_{syn} is given by the following formula (e.g. Heesen *et al.* 2009):

$$\frac{t_{syn}}{yr} = 8.352 \times 10^9 \left(\frac{E}{GeV}\right)^{-1} \left(\frac{B}{\mu G}\right)^{-2} \tag{3.2}$$

where B is the strength of total magnetic field (see Sec. 3.4.1) and E (energy of the relativistic particles), which can be calculated with:

$$\frac{E}{GeV} = \left(\frac{\nu}{16.1\,MHz}\right)^{0.5} \left(\frac{B}{\mu G}\right)^{-0.5} \tag{3.3}$$

here, ν is the frequency of observations.

Having the average h_e (taken from the measurements of h_{syn}[2]) and t_e, it was finally possible to compute the sought-after bulk speed of CR electrons; the results are given in Table 3.5. The estimated speeds are considerably larger than the escape velocity (of 40 km s^{-1}) and show plausibility of galactic scale winds in IC 10[3].

Galactic winds are considered as one of the mechanisms to form large-scale X-shaped magnetic fields found in edge-on spiral galaxies (Brandenburg *et al.* 1993; Ferriére & Terral 2014). In IC 10, possibly some fragments of such an extraplanar structure are observed (Sec. 3.4.3),

---

[2]The most outlying values (Table 3.4) were discarded.

[3]Note that the speed at 4.86 GHz was estimated from a limited number of useful fits of disk models to the slices.
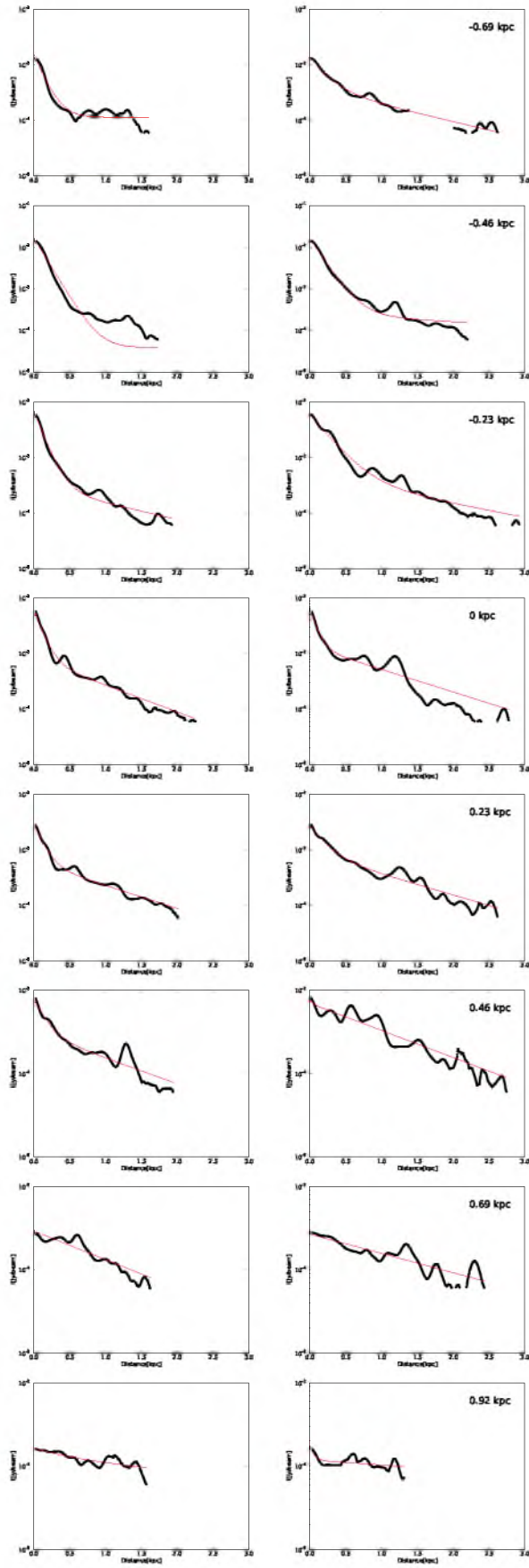
Figure 3.14: 1.43 GHz radio emission slices of IC 10 with fitted two or one disk models (see text and Table 3.4 for details). The images on the left (right) side present slices for the northern (southern) part of the galaxy.
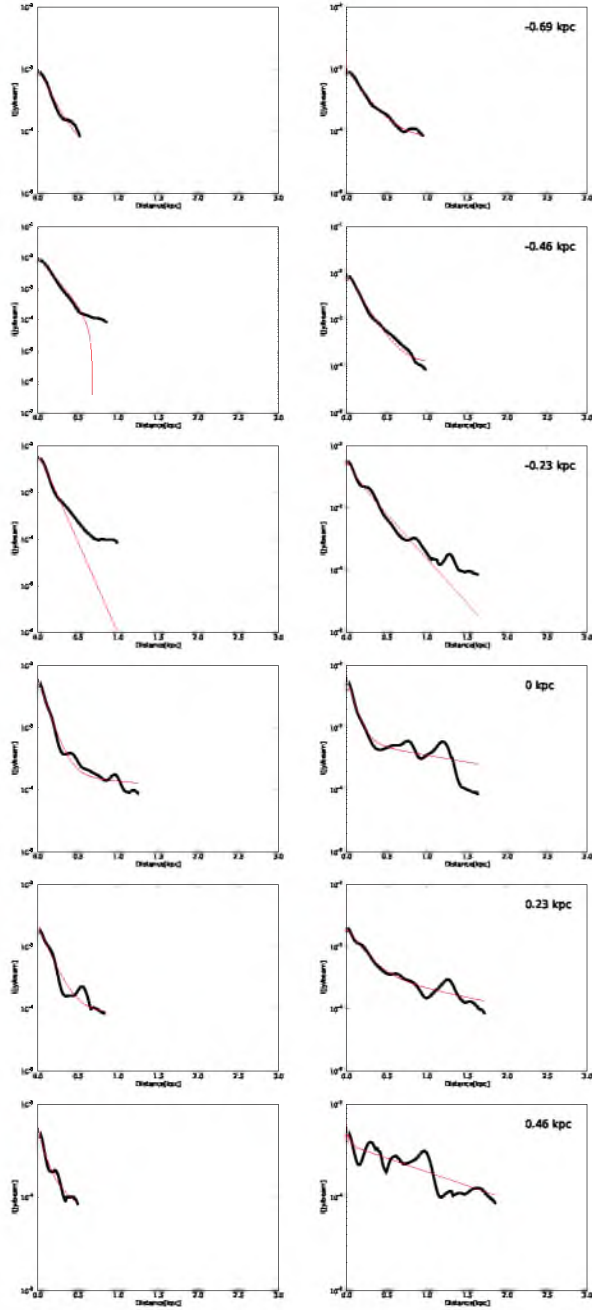
Figure 3.15: 4.86 GHz radio emission slices of IC 10 with fitted two or one disk models (see text and Table 3.4 for details). The images on the left (right) side present slices for the northern (southern) part of the galaxy.

Table 3.4: Synchrotron scale heights for IC 10

Distance from galaxy center kpc	Scaleheight of thin disk kpc		Scaleheight of thick disk kpc	
	North	South	North	South
1.43 GHz				
-0.69	0.14	0.21	n/a	1.41
-0.46	0.15	0.17	n/a	4.02
-0.23	0.13	0.26	1.45	1.72
0	0.11	0.09	0.90	1.07
0.23	0.12	0.19	1.05	1.15
0.46	0.15	0.03	1.40	1.33
0.69	n/a	n/a	1.26	1.87
0.92	0.37	0.06	4.20	7.58
4.86 GHz				
-0.69	0.17	0.22	n/a	n/a
-0.46	0.15	0.15	n/a	n/a
-0.23	0.11	0.09	0.02	0.30
0	0.11	0.09	4.01	1.95
0.23	0.14	0.19	n/a	1.64
0.46	0.09	0.03	0.82	1.48

Table 3.5: Bulk speed of CRs in IC 10

Frequency GHz	Bulk speed km s^{-1}	
	North	South
1.43	120	142
4.86	150	309

indicating that the galactic winds can indeed play an important role in forming this particular field morphology.

Galactic-scale winds are also considered as a crucial mechanism enabling galaxies to magnetize intergalactic medium (e.g. Beck & Wielebinski 2013). For a long time it has been believed that the dwarf galaxies which actively form massive stars, like IC 10, should be the most efficient IGM's magnetic field providers (Kronberg et al. 1999). However, some recent investigations indicate that this may not be the case (Chyży et al. 2011, see Sec. 2.4.6). The results of sensitive radio observations presented in section 3.3 show that IC 10, similarly to NGC 2976, actually supports the conclusions of Chyży et al. (2011) as its strong total power and polarized emission are definitely less extensive than 5 kpc. It should be noted, as in the case of NGC 2976, that the conclusions presented here are based only on the radio continuum observations. When one would take into account the extension of HI emission, assuming that the volume it fills is also magnetized, the picture showing efficiency of IC 10 as an IGM magnetizer would dramatically change. However, in this case other (external) processes, like gravitational

interactions, have to be taken into consideration.

3.5 Conclusions

I present multi-frequency (1.43 GHz, 4.86 GHz and 8.46 GHz) VLA and Effelsberg observations of IC 10, the nearest starbursting dwarf galaxy. The main conclusions are as follows:

- Sensitive VLA observations at 1.43 GHz reveal a large radio envelope of IC 10, extending up to 1.5 kpc from the galactic centre, thus almost two times further than the main optical body of the galaxy. The envelope is not seen at higher frequencies (4.86 GHz and 8.46 GHz), suggesting substantial aging of CR electrons, actually confirmed by gradual steepening of the spectral index with distance from the galactic disk.

- As compared to the total radio emission, the polarized emission of IC 10 at 4.86 GHz and 8.46 GHz is more clumpy, with the most pronounced polarized blob at the SE edge of the disk, corresponding to the strong total-power region named "superbubble" by Yang & Skillman (1993). At 1.43 GHz, the polarized signal covers not only the entire galaxy but also its surroundings. I conclude from the low galactic latitude of the object (-3.3^o) that this emission is mainly the Milky Way's foreground signal, not related to IC 10. So strong foreground polarized emission has not been found in any external galaxy before and may portend difficulties in obtaining and interpreting polarized signals from galaxies observed at extremely low radio frequencies, now starting to be covered by the LOFAR instrument.

- The distribution of separated nonthermal emission shows an N-S asymmetry, likely due a smaller number of HII regions and thus CRs acceleration sites in the northern part. In the southern part of the disk, where large star-forming complex is observed in Hα emission, the degree of polarization is low and Faraday depolarization is high, which indicates less-ordered magnetic fields, with more turbulent motions as well as more field tangling.

- Despite the small size and mass of IC 10, magnetic fields are strong in this object with the mean strength of about 14 μG, similar to that found in massive spiral galaxies. The fields are mostly random, with field regularity of 0.17 ± 0.07 and strength of the ordered component $B_{ord} = 2.3 \pm 0.7 \mu$G. Such fields can be produced by a small-scale MHD dynamo sustained by the intensive phase of star formation visible in Hα emission spread over the entire galactic disk.

- The distribution of rotation measures between 4.86 GHz and 8.46 GHz reveals some regions with unidirectional magnetic fields that can originate from large-scale dynamo process. As the contribution of the Milky Way foreground RM is not known, further investigation to confirm this conclusion is needed, which requires spectro-polarimetric data and application of the rotation measure synthesis method. The calculated dynamo number for IC 10 is supercritical and does not exclude an action of the large-scale dynamo. However, due to galactic slow rotation, the process of generation of the regular field in the object is probably relatively long (of about 800-1700 Myr, according to MHD simulations).

- On the largest scales, the apparent B-vectors of the polarized intensity exhibit a global X-shape morphology of magnetic fields, which is often observed in the spiral galaxies with high SFR seen edge-on. No such structures have been observed in dwarf galaxies

so far. An X-shaped magnetic field structure in spirals can be brought about by a galactic large-scale dynamo acting in the halo or by a large-scale wind blowing outward from the galactic disk. Some evidence for galactic winds has been actually found in IC 10.

- The performed analysis of slices of radio emission across the object's major axis at 1.43 GHz and 4.86 GHz indicates that the scale height of the thick disks of IC 10 is similar to NGC 253 and other more massive spiral galaxies. Along with the estimated synchrotron radiative times of CR electrons, this implies the bulk speed of CRs of 150-300 km s^{-1}, which is much larger than the gas escape velocity, which leads to the conclusion that galactic-scale magnetized winds in this object are quite plausible and that they can shape the magnetic field morphology as well as the extensive radio envelope. Moreover, the magnetized plasma spread out of the galaxy can also seed the intergalactic medium (up to about 5 kpc distance) with random and ordered magnetic fields.

- The magnetic fields within the disk are mostly parallel to the galactic plane, except for the eastern part, at the location of the superbubble, where magnetic fields are roughly perpendicular to the major axis and have the same orientations as the prominent dust lane that can be seen in optical images. This may reveal some external process, as infalling gas or past tidal interactions, resulting in a polarized emission enhanced by compression and ordering of magnetic fields.

The dwarf galaxies are generally regarded as the simplest stellar systems. IC 10 testifies that this may not be true. The radio picture of this object is a complex one, manifesting features found previously only in massive spiral galaxies, which ISM properties are strongly affected by density waves. Therefore, this dwarf object is important for our understanding of generation and evolution of magnetic fields in galaxies as well as for realistic modelling of the ISM.

Chapter 4

M81

4.1 Introduction

One of the most fundamental problems of galactic astrophysics is to determine and account for the presence of large-scale magnetic structures within galactic disks, as well as their relation to the different components of the interstellar medium (ISM) and the galaxy evolution. According to the mean-field dynamo theory, the geometry of magnetic fields in galactic disks can be described with respect to the azimuthal angle ϕ as a decomposition of the field strength into Fourier modes (m): $B = \Sigma_m B_m \exp(im\phi)$ (e.g. Beck *et al.* 1996). The first (axisymmetric) mode $(m = 0)$ is most readily excited (e.g. Shukurov 2004), therefore it should dominate in galactic disks (Fig. 4.1). This actually agrees with the magnetic field structure observed in the nearby galaxies (Beck *et al.* 1996; Braun *et al.* 2010). One exception is M 81, which is the only external galaxy to show an indication of bisymmetric magnetic field. Using the radio polarimetric data at 6 and 21 cm, Krause *et al.* (1989b) claimed that the distribution of Faraday rotation measure (RM) intrinsic to the galaxy is consistent with the bisymmetric (BSS) dominant $(m = 1)$ magnetic field, i.e. with field reversals (Fig. 4.2).

The *exceptional case of M 81* suggests that either the interpretation of existing radio data was misleading or that our knowledge of the dynamo theory is still far from complete. The need to obtain a more accurate picture of M 81's magnetism was already recognized long ago (Shukurov 2005).

Recently, a powerful method enabling one to properly compute Faraday rotation from the diffuse polarized emission was introduced – the RM Synthesis (Brentjens & de Bruyn 2005), requiring multi-channel radio polarimetric observations (see, Sec. 1.3.3). It solves the problem of $n\pi$ ambiguity and allows the separation of polarized structures in Faraday depth, originating from different regions along the line of sight. This helps to determine different physical processes that underlie magnetic field in the different regions as well as opens up perspectives
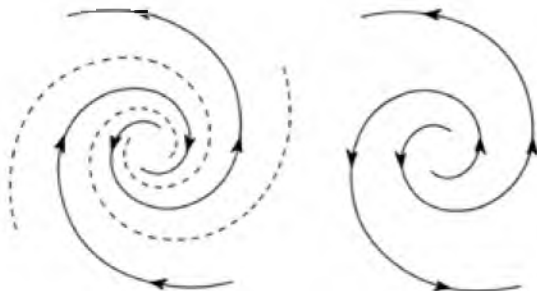
Figure 4.1: Sketch showing bisymmetric and axisymmetric configuration of dynamo-generated magnetic fields and reversals of magnetic fields in the former case (i.e. opposite signs of field directions in adjacent spiral arms). The sketch comes from Krause *et al.* (1989a)
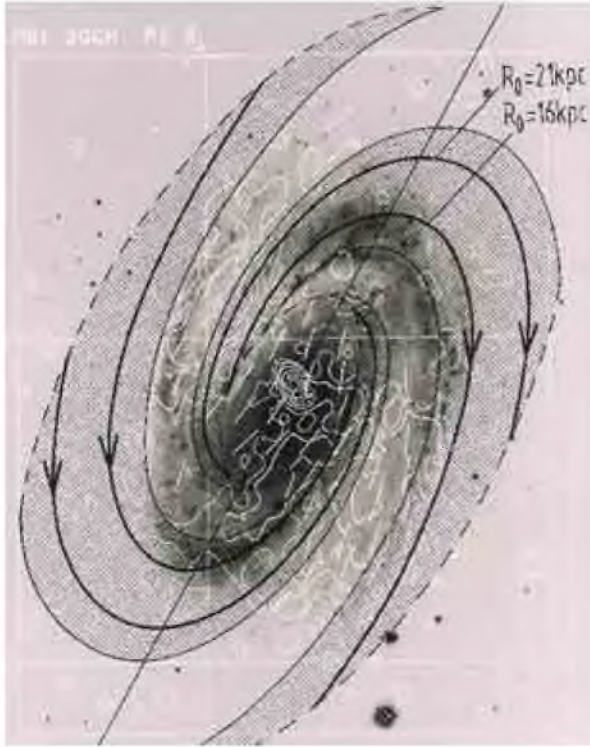
Figure 4.2: Model of bisymmetrical magnetic field structure for M 81 as suggested by Krause *et al.* (1989b) overlaid on the optical image of the galaxy and the polarized emission at 1400 MHz (in contours).

for understanding cosmic magnetic fields on galactic and intergalactic scales. RM Synthesis was implemented successfully in processing polarimetric observations of nearby galaxies at frequencies from 1300 to 1760 MHz (Heald *et al.* 2009, Braun *et al.* 2010). Their study reveals the fact that polarized emission emerges not only from the star-forming galactic disks, but also from above and below the disk. Thus, the simplistic assumption made by Krause *et al.* (1989b) that the observed azimuthal modulation of RM is caused only by the disk component could be actually not sufficient.

M 81 is not an easy object for radio observations due to a number of factors. The most relevant one is the proximity of M 82 galaxy, which is a relatively bright source in the radio domain. The other factor is its low surface radio brightness, which requires using the most sensitive instruments and sophisticated methods of data calibration. In the next sections, I am going to present new observations of M 81 from the JVLA (Karl G. Jansky Very Large Array)[1] and WSRT[2] projects. I aim to combine the capabilities of the novel RM Synthesis method and the state-of-the-art spectral capabilities of the interferometers in order to provide a better picture of magnetism in M 81.

4.2 Observations and data reduction

4.2.1 JVLA

M 81 was observed for almost 7 hours (divided into two observational runs) with the JVLA in its C configuration at L band (1.0 - 2.0 GHz). The band was divided in 16 sub-bands, each possessing 64 (1 MHz wide) spectral channels. The observations were performed in the full

---

[1]The National Radio Astronomy Observatory is a facility of the National Science Foundation operated under cooperative agreement by Associated Universities, Inc.

[2]The Westerbork Synthesis Radio Telescope is operated by ASTRON (Netherlands Institute for Radio Astronomy) with support from the Netherlands Foundation for Scientific Research (NWO).

Table 4.1: Parameters of the JVLA observations of M 81

Project number	12A-369
Observing band	L(1.0 – 2.0 GHz)
Configuration	C
Date of observations	12-Apr-24 00:00:34 – 12-Apr-24 03:29:57
	12-Apr-24 23:26:55 – 12-Apr-25 02:56:20
Total on source time[hrs.]	4.8
Number of sub-bands	16
Number of frequency channels/sub-band	64
Width of single frequency channel[MHz]	1
r.m.s.[μJy/beam] σ_I	13μJy/beam

polarization mode, following the standard for this instrument observational procedure that involves alternate scanning of target and phase calibrator (every 30 minutes). As a phase calibrator, J0841+7053 was chosen, whereas as an amplitude and polarization angle calibrator, the source 3C 138 (0521+166) was used. Furthermore, I observed a polarization leakage-term calibrator J0319+4130, which was chosen basing on the JVLA polarization observational guide. In order to be able to check the calibration quality, observations of 3C 147(J0542+4951) were performed - this source is known to possess a low polarization level. The details are given in the Table 4.1.

In the first stage of data reduction, the observations were preliminarily evaluated and not-working antennas were removed. Then an initial bandpass calibration was performed following automatic flagging of the most affected by RFI sub-bands with usage of AOFlagger (Offringa *et al.* 2010, Offringa *et al.* 2012). Unfortunately, a large fraction of data (about 20-30%) collected in the frame of this spectral band turned out to be unusable, because of RFI. Among them, two out of 16 sub-bands (no. 3 and 9 counting from 0) were completely discarded from the further analysis. For each usable sub-band, a separate flagging strategy was worked out. Just in case of any remaining RFI, additional flagging was performed using CASA package. A few sub-bands, weakly affected by RFI, were flagged manually.

Calibration was performed for each observing run separately with CASA package mostly, according to the "Supernova Remnant 3C 391: 6cm Polarimetry and Continuum Imaging, Mosaicking" tutorial of reduction of JVLA polarimetric data. In first stage, the flux-scale for 3C 138 and 3C 147 was fixed for each spectral channel according to the standard scale of Perley & Butler (2013). Then, prior to the bandpass calibration (B-term) initial phase, only electronic gain solutions (G-term) were obtained for the calibration sources. These solutions were used in the bandpass calibration. The bandpass gains obtained for both calibrators agreed well and were used to obtain electronic gains for all the calibration sources (including the phase and leakage calibrators). In the next stage, a polarization calibration was performed, starting from obtaining solutions for the frequency-dependent polarization-leakage (between R and L receptors, Df-term). For this purpose, I used three of the calibration sources: the phase calibrator which was observed on the paralactic angle range of nearly of 60 degrees, the leakage-term calibrator, and 3C 147. The solutions obtained from these sources were then compared and they turned out to be in a very good agreement. The solutions obtained for the phase calibrator were applied to the data. As a final polarization calibration step, the frequency dependent polarization angle (phase difference between R and L receptors for reference antenna, the Xf-term)
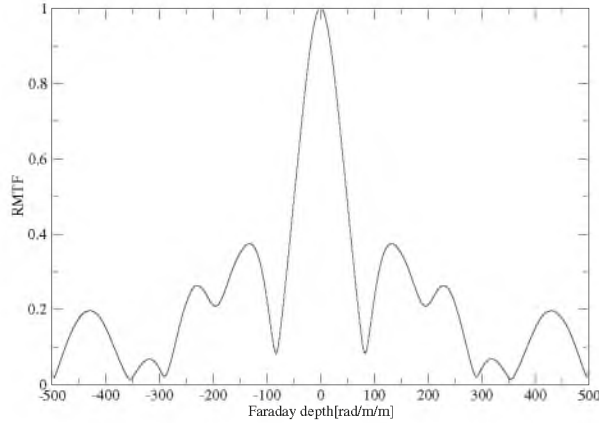
Figure 4.3: Shape of rotation measure transfer function obtained for the frequency coverage of the L band of the JVLA observations.

corrections were obtained. For this purpose I used source 3C 138, for which phase differences and polarization degrees measured in a wide range of frequencies were known (Rick Perley, priv. comm., this information is also implemented in the RLDIF task of the AIPS package). These values were then linearly interpolated to the central frequencies of each sub-band.

After the initial calibration using the calibration sources, the data from the both observing runs were concatenated and self-calibrated in phase-only. However, prior to the self-calibration, peeling of the M 82 had to be performed. M 82 strongly disrupted the primary beam area for most of the sub-bands (in which it was clearly visible in one of the side-lobes), which prevented obtaining a reliable model for M 81. For this purpose, I prepared a dedicated CASA script. The peeling procedure involved the following steps: obtaining a Stokes I-only model of the whole field of view and subtracting it from the UV-plane, except for the disturbing source (M 82); obtaining and applying to the data its electronic gain solutions; subtraction of the interfering source from the UV-plane; inversing the obtained gains and applying them back to the data. In the final step, the model of the field of view was Fourier-transformed and added to the UV-plane. The described peeling procedure enabled me to improve quality of the Stokes I maps. Unfortunately, a similar strategy was not possible to be applied to the Q and U Stokes parameters, because in this case the dominant effect (in addition to the directional electronic gains) is related to the off-axis polarization leakage (Steve Myers and Miriam Krauss, priv. comm.).

As a final calibration step, one phase-only self-calibration was performed for each sub-band supplied with its own Stokes-I model for the UV-range limited by the flux contained in this model. The final imaging was made by applying different strategies for the Stokes I, Q and U. The total power map (Stokes I) was imaged using the whole available data set with the Briggs robust weighting set to 0.5 (giving an optimal compromise between the sensitivity to the extended structure and the level of the artifacts due to nearby background sources). For the imaging, I used a wide-field technique with the 512 w-projection planes, estimated according to the formula given in the CASA cookbook, two Taylor coefficients aimed to model the sky frequency dependence and the multi-spatial scales (Rau & Cornwell 2011). As a result of using more than one Taylor coefficient, I also obtained a spectral index distribution map for the entire field of view.

The Stokes I map was cleaned in the fly's-eye specified clean-boxes down to the $1-2\,\sigma$ noise level. Stokes Q and U imaging were cleaned on a per-channel basis in the clean-boxes obtained for one central sub-band. The wide-field technique was also used for them. It should be noted that for imaging of all the Stokes parameters, I used only the good-quality spectral channels filtered out on the basis of the Stokes I data cube obtained prior to the final imaging as well as quality of the frequency-based calibrator solutions (bandpass, leakage-term, polarization

Table 4.2: Parameters of the WSRT observations of M 81

RT9-RTA	Start Obs. Date	Stop Obs. Date
36	23/03/2010 14:48:15	24/03/2010 04:03:15
48	24/03/2010 14:44:25	25/03/2010 03:59:15
60	25/03/2010 14:59:05	26/03/2010 03:55:15
72	08/04/2010 13:45:25	09/04/2010 03:00:15
84	07/04/2010 13:49:15	08/04/2010 03:04:15
84	05/04/2011 13:58:05	06/04/2011 03:13:05
96	06/04/2010 13:53:15	07/04/2010 03:08:05
maxishort	17/11/2010 23:04:35	18/11/2010 06:42:55

angle). The obtained Q and U data cubes in a function of frequency were then used as an input for the RM Synthesis software (written by the author) applying the natural weighting of frequency channels (see Appendix B for details). The data cubes obtained in this way in Faraday domain were then cleaned with the algorithm given by Heald *et al.* (2009), which was also implemented in the author's RM Synthesis software. The frequency coverage obtained in these observations resulted in the rotation-measure transfer function (RMTF) shown in the figure 4.3. The resolution is about $52\,\mathrm{rad\,m^{-2}}$, while the highest observable Faraday depth is about $7.7 \times 10^5\,\mathrm{rad}\ ^{-2}$. This seems to be one of the highest resolutions obtained to date in the Faraday space for a nearby galaxy. What is also important, the used frequency setup permitted to obtain sensitivity to the extended structures in the Faraday space up to about $140\,\mathrm{rad\,m^{-2}}$. Thus with these data it is possible to see their internal details. For the sake of comparison, the sensitivity to the extended Faraday sources obtained in the WSRT-SINGS survey (Heald *et al.* 2009) was $110\,\mathrm{rad\,m^{-2}}$, while the resolution was $140\,\mathrm{rad\,m^{-2}}$.

4.2.2 WSRT

M 81 was also observed in 85 cm band[3] with the WSRT interferometer (project no. R10A/020). The array consists of 14 dishes, where ten of them (labeled RT0-9) have fixed positions, and the remaining four (RTA-RTD) are movable. The observations were performed in 6×12 configuration mode, in which the distance between RT9 and RTA was changed in constant 12-meter intervals (Table 4.2). The data collection in the 84-meter configuration had to be repeated as a significant part of the original run was unusable due to hardware problems. Moreover, as the observations were conducted partly during daytime, they were affected by strong solar interferences. Unfortunately, it was not possible to properly calibrate this effect (see below) and the affected data had to be discarded. In order to complement at least partly for the missing uv coverage, an additional observing run in the "maxishort[4]" configuration was scheduled and performed.

The whole band, ranging from 310 MHz – 380 MHz, was divided into 8 sub-bands of 10 MHz width. Each of the sub-bands consisted 128 frequency channels, containing full (XX, XY, YX, YY) polarization information. As a flux, bandpass, electric gain, and polarization leakage, the calibrator sources 3C 295 and 3C 147, which are known to be unpolarized in this

---

[3]Also known as 92 cm for historical reasons.

[4]See, http://www.astron.nl/radio-observatory/astronomers/wsrt-guide-observations/wsrt-guide-observations for details.

frequency range, were used. At the beginning of each observing run 3C 147 was observed, and at the end 3C 295. These two calibrators were supported by additional two sources DA 240 and 3C 303, used for calibration of polarization angles. At such low frequencies, the ionosphere can severely impact polarization calibration and its contribution needs to be estimated. It is known that the electron density in ionosphere can change during an observing run (e.g. Brentjens 2008). In order to trace these changes, the DA 240 was additionally observed twice during each 12 hours observing session.

For purpose of this thesis, I reduced one of the eight available frequency bands (band no. 6, starting from 0, 320-328 MHz). Calibration and imaging of data was performed within the CASA package in the similar way as that presented by de Bruyn & Brentjens (2005), Brentjens (2008) and Pizzo et al. (2011). In the first stage of data reduction, the quality of observations was evaluated. Then RFI-affected data were flagged with AOFlagger software (Offringa et al. 2010, Offringa et al. 2012). In the next step, a standard calibration using the mentioned above calibrators was performed. The unpolarized sources 3C 295 and 3C 147 were used to obtain B, G, and Df (frequency dependent) Jones calibration tables, which were subsequently transferred to the rest of observed sources (i.e. polarized calibrators DA 240, 3C 303 as well as M 81). In the next step, an X(frequency independent) Jones calibration table (describing phase difference between X and Y receptors) was obtained from DA 240 and 3C 303 and then finally transferred to M 81. Each of these steps were applied separately to all the observing configurations.

After calibrating all the runs, they were then concatenated in the UV plane domain and self-calibrated. The self-calibration was performed separately for each frequency channel equipped with its own IQUV model. It included three phase-only self-calibration steps and then the final amplitude and phase step.

Finally, the neighbour galaxy M 82 was peeled with BBS[5] (again per channel basis). After the peeling procedure, M 82 was added back to the data. Imaging of Stokes I parameter was performed for the good-quality channels only with usage of multi-frequency algorithm. The final r.m.s. noise level obtained for the Stokes I is 0.5 mJy/beam for resolution of 49.6" × 47.3".

The Stokes Q and U were imaged for each channel with Briggs robust weighting of 0.25. Having Q and U data cubes, I performed a synthesis of rotation measure for them, obtaining real and imaginary parts of polarized intensity in Faraday depth domain sampled from -500 to +500 rad m^{-2} every 2.5 rad m^{-2}. The available frequency coverage resulted in Faraday resolution of about 84 rad m^{-2} and maximum observable Faraday depth of about 2200 rad m^{-2}. The obtained RMTF function is shown in figure 4.4.

4.3 Results

4.3.1 Low-frequency total power radio emission from M 81

In the figure 4.5 the L band total power radio map of M 81 is superimposed on the optical image in blue light. The radio emission coming from the spiral arms and the central part of the galaxy is visible. Through the next sections of this chapter, the following convention will be used concerning the M 81; the spiral arm that ends in the north will be described as the eastern-arm and the other one as the western-arm, (such conventions were also adopted by Krause et al. 1989b). The radio emission of both the spiral arms extends to nearly the same distance from

---

[5]BBS is a part of software dedicated for the LOFAR telescope, see http://www.astron.nl/radio-observatory/lofar/lofar-imaging-cookbook
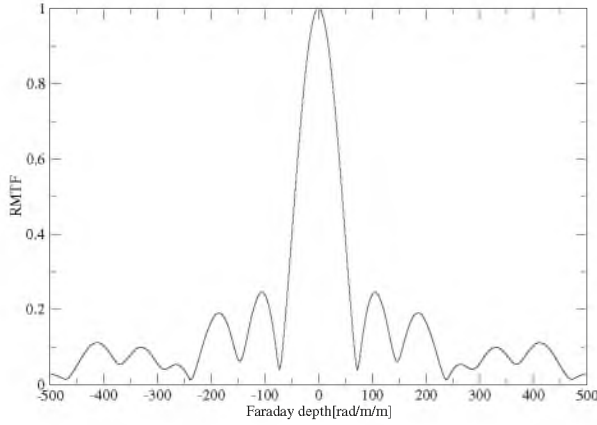
Figure 4.4: Shape of rotation measure transfer function obtained for the frequency coverage of the sub-band no.6 of 92 cm band of the WSRT observations.

the centre. However, there is a very weak and diffuse emission visible in an ending part of the eastern-arm (approximately at 2σ noise level). The brightest emission in the radio as well as the optical light coincides with the central region of the object, where a Seyfert-type nucleus resides. With the linear resolution available for the L band map (of about $0.3\,\mathrm{kpc} \times 0.2\,\mathrm{kpc}$), an internal structure of the nucleus can be resolved (it will be described in a more detailed manner in the section 4.3.2). Around the nucleus, there is no radio emission. This radio emission-free valley extends to the north and south from the central region, which was already noted by Beck *et al.* (1985) and Krause *et al.* (1989b) and is typical for the early-type spiral galaxies. This observational fact is not surprising as this part of the object is nearly void of HII regions (Kaufman *et al.* 1987, see also Fig. 4.6). It should be noted that the negative contours observed in this place are due to missing short spacings and possible deconvolution errors. The missing spacings also cause that the total flux of $72 \pm 2\,\mathrm{mJy}$ (not including nucleus) measured for the object is lower than values discussed in Beck *et al.* (1985).

In the figure 4.6, the radio map is superimposed on the Hα image. Comparison of both the images reveals that the brightest parts of the spiral arms traced by HII regions are closely followed by the total-power emission. Only in the internal part of the western arm more diffuse-like radiation can be observed.

In the figure 4.7, the WSRT total power map (of resolution of 49.6" $\times$ 47.3") at 324 MHz is presented. The radio emission that can be seen in this map follows the spiral arms and is more diffusive than that in the L band data. The brightest radio radiation is related to the central part of the galaxy. What is interesting, the observed total power emission (with the sensitivity of $0.5\,\mathrm{mJy/beam}$) of M 81 at 324 MHz does not extend further than that at 1.4 GHz. This implies that its magnetic field and relativistic electrons are closely related to the massive spiral arms. On the other hand, the sensitivity of current data is not sufficient to cover the low-brightness emission. The same can be suspected from the measurement of total-power flux integrated over the whole object at this frequency (not including its nucleus and background source located at R.A.(J2000.0):09^h 55^m 25.64^s, Dec.(J2000.0):69° $10'$ $07.0"$) which is $450 \pm 28\,\mathrm{mJy}$. This value seems to be too low when compared with the global spectrum of Beck *et al.* (1985).

With the excellent field of view of the WSRT at frequency of 324 MHz, it was possible to map the central part of M 81 galaxy group (including M 81, M 82, and NGC 3077) within a single pointing (Fig. 4.8). All the three brightest galaxies were detected in the total-power emission. The radio emission of M 82 while detected at a high confidence level, seems to be distorted due to some calibration errors and cannot be studied further. The emission from NGC 3077 is detected only from its central part. In the presented data, NGC 2976, located at the boundary of the field of view, can be seen as well (not shown in the figure 4.8). With the available sensitivity. there are no signatures of diffuse emission residing between the galaxies

71

Figure 4.5: Total-power contours of M 81 (natural weighting) at 1.52 GHz superimposed on the DSS blue image. The contour levels are (-5, -3, 3, 5, 8, 12, 20, 35, 65, 150, 250, 400, 700, 1500, 4000) $\times$ 13μJy/beam. The map resolution is 16.5" $\times$ 12.7" HPBW (beam shape is indicated by a green dot in the bottom-left corner of the image).

Figure 4.6: Total-power contours of M 81 (natural weighting) at 1.52 GHz superimposed on the Hα image (Hoopes *et al.* 2011). The contour levels are (-5, -3, 3, 5, 8, 12, 20, 35, 65, 150, 250, 400, 700, 1500, 4000) × 13μJy/beam. The map resolution is 16.5" × 12.7" HPBW (beam shape is indicated by a green dot in the bottom-left corner of the image).
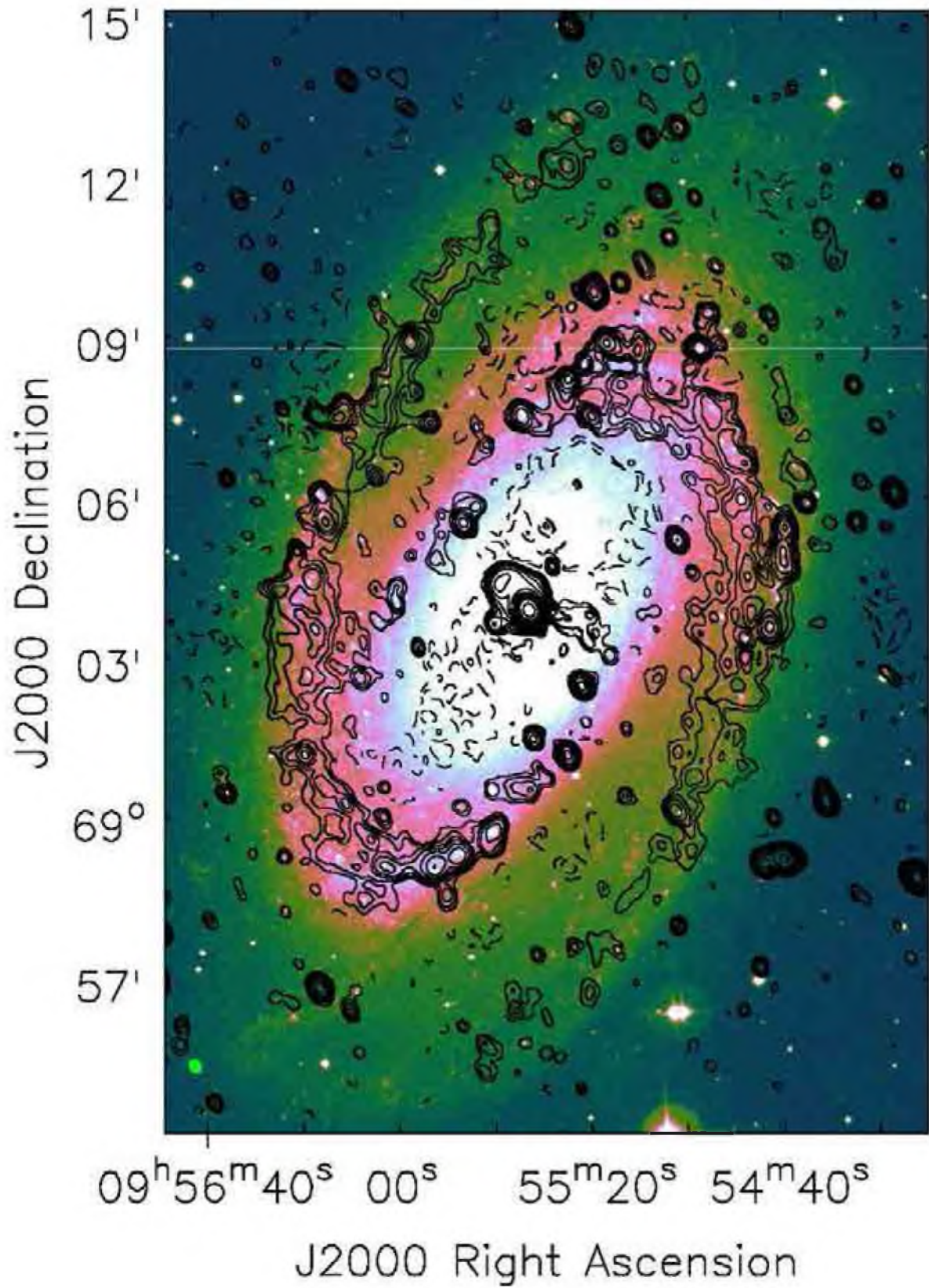

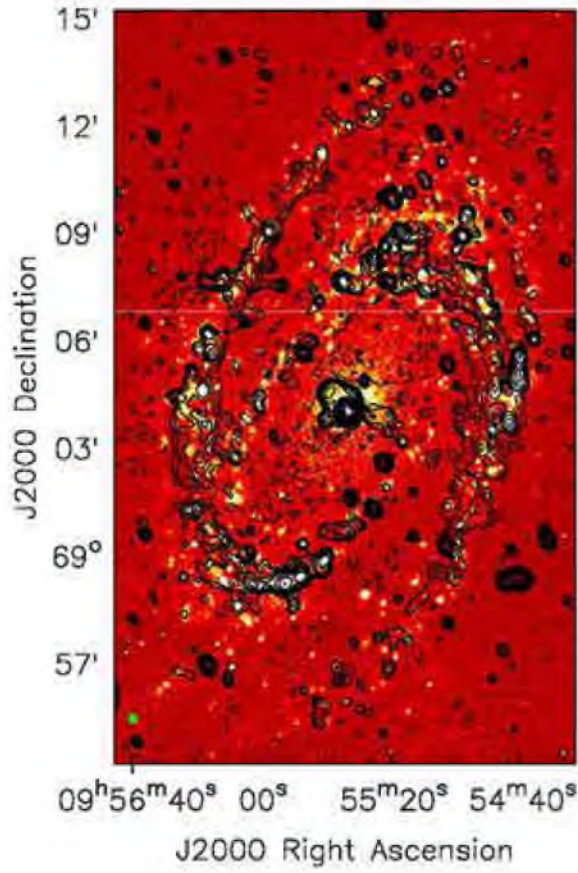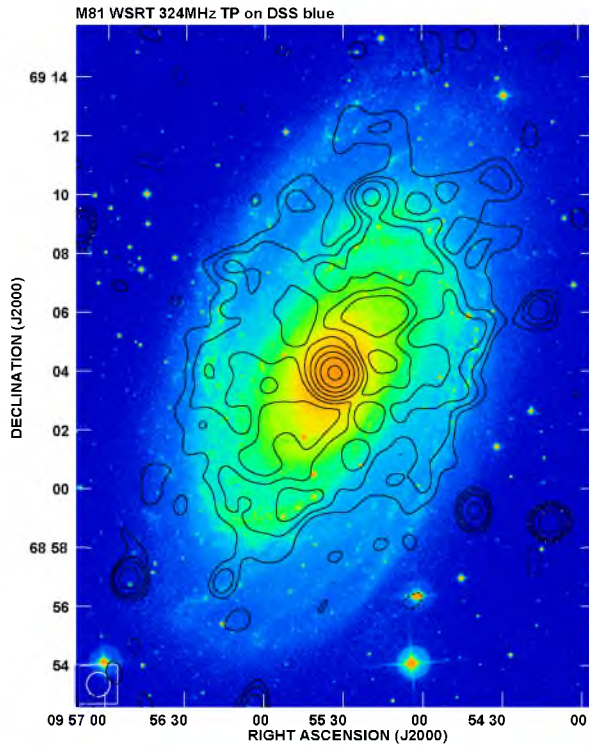Figure 4.7: Total-power contours of M 81 at 324 MHz superimposed on the DSS blue image. The contour levels are (-5, -3, 3, 5, 8, 16, 32, 64, 128) × 0.55mJy/beam. The map resolution is 49.6" × 47.3" HPBW.
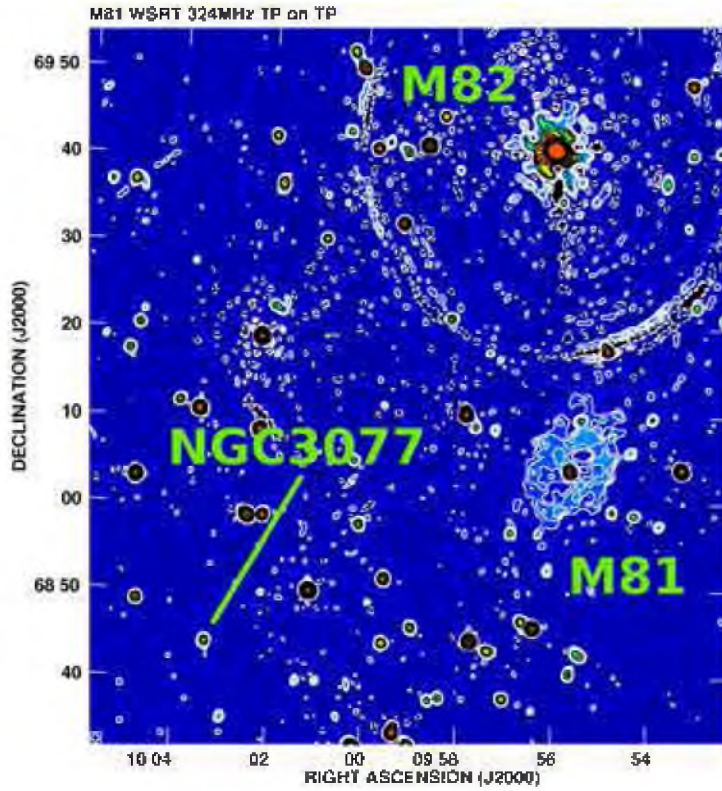
73

Figure 4.8: Total-power contours and colours of the central part of M 81 group at 324 MHz. The contour levels are (-5, -3, 3, 5, 8, 16, 32, 64, 128, 256, 512, 1024) × 0.55mJy/beam. The map resolution is 49.6" × 47.3" HPBW.

of the group as it is observed in HI (Yun *et al.* 1994; Chynoweth *et al.* 2008). This indicates that there is no strong magnetic field and/or relativistic electrons in the space between galaxies. The upper limit of such a magnetic field strength is estimated and analysed in section 4.4.1.

4.3.2 Nuclear region

In the central part of M 81, there is an active galactic nuclei (AGN, likely mini-Seyfert 1; e.g. Kaufman *et al.* 1996). Along with Cen A, this is the closest AGN (e.g. Bartel *et al.* 1995). The JVLA L-band data (imaged with uniform weighting), possessing resolution of 9.5" × 6.7" reveal an internal structure of the core (Fig. 4.9), which consists of two main parts, a bright centre and a characteristic arc located to the NE direction. In the barely resolved centre, there can be seen an extension in the western direction; this is the most likely a radio filament identified by Kaufman *et al.* (1996).

In between the centre and the arc, there are visible two radio bridges in the western and eastern parts of the map. Similar bridges were observed by Kaufman *et al.* but at the higher frequency of 5 GHz. At the frequency of 1.4 GHz, the authors were able to discern just a single bridge located between those mentioned above. The question arises, what could underlie the observed differences in morphology of the bridges? As the size of the whole galaxy centre shown here is of order of 1 kpc, it is rather not possible that any physical process is responsible for changing the observed bridges morphology as it can be estimated that light would need more than 3000 years to travel this distance. There was observed a time variability of the flux of the source but it was strongly related to its central, brightest part, where most likely a jet resides (e.g. Marti-Vidal *et al.* 2011b). However, there is no information about changes in morphology of diffuse structures of M 81's nucleus. Further observations could help to resolve this issue.
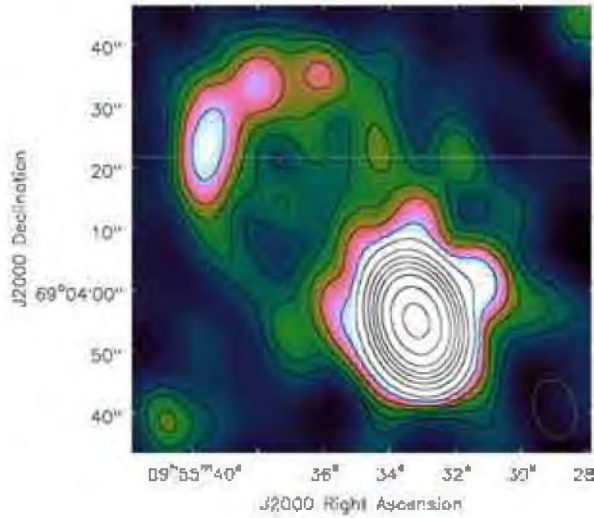
74

Figure 4.9: Total-power radio emission at 1.52 GHz (uniform weighting) of the nuclear region of M 81. The contours levels are (-5, -3, 3, 5, 8, 12, 20, 35, 80, 150, 250, 400, 700, 1500, 3000) × 25μJy/beam. The map resolution is 9.5" × 6.7" HPBW, position angle of the beam is 17.3 degrees.

4.3.3 Supernova SN1993J

M 81 harbours the famous SN1993J supernova. The supernova was discovered on 28.91 March 1993 (Ripero *et al.* 1993) and is one of the most energetic ones as well as the closest supernova of the previous century (e.g. Bartel *et al.* 2000). It can be clearly discerned in our L-band JVLA data (see, Fig. 4.5, 4.6).

One of the most important observed features of supernovae are their light curves. Such a multi-frequency radio light curve for SN1993J can be found e.g. in Weiler *et al.* (2007), covering the SN age in time range from 3.1 to 4929.64 days from explosion. My new data increase this period to 6967 days. The measured L-band flux of the supernova is 1.19 ± 0.12 mJy. Using the literature available data points (from Weiler *et al.* 2007) and the new measurement, an updated radio light curve in 20 cm band for SN1993J was constructed (Fig. 4.10).

Radio light curves of supernovae are expected to rise at the beginning in the phase of external (free-free and/or synchrotron) absorption. After reaching the maximum of the flux, they decrease gradually, remaining in the optically thin regime (e.g. Bartel *et al.* 2002). As it can be seen, the new measurement from the JVLA data extends considerably the flux decaying trend of the supernova SN1993J.

The decline rate of the light curve steepens around ~3100 day from the explosion and can be described by an exponent with an e-folding time of 1100 days (Weiler *et al.* 2007). The exponential flux density decay was explained as an effect of expanding shock in changing (dropping) density of circumstellar medium (CSM; Weiler *et al.* 2007). However, this was questioned by Marti-Vidal *et al.* (2011a), who argued that even a strong drop in density of CSM cannot account for the observations. They concluded that with a negligible density of circumstellar medium, radiative-cooling effects are needed to model the late (after 3100 days) radio light curve of the supernova. Alternatively, in the case of non-negligible density of the CSM also a finite mean lifetime of relativistic electrons and their escape from the radiating region are required. The fact that the new JVLA measurement follows the trend marked by the previous data without increasing the flux decay suggests that for SN1993J, a non-negligible CSM density as well as a relatively long mean lifetime of relativistic electrons (as modeled by Marti-Vidal *et al.* 2011a) are the case.
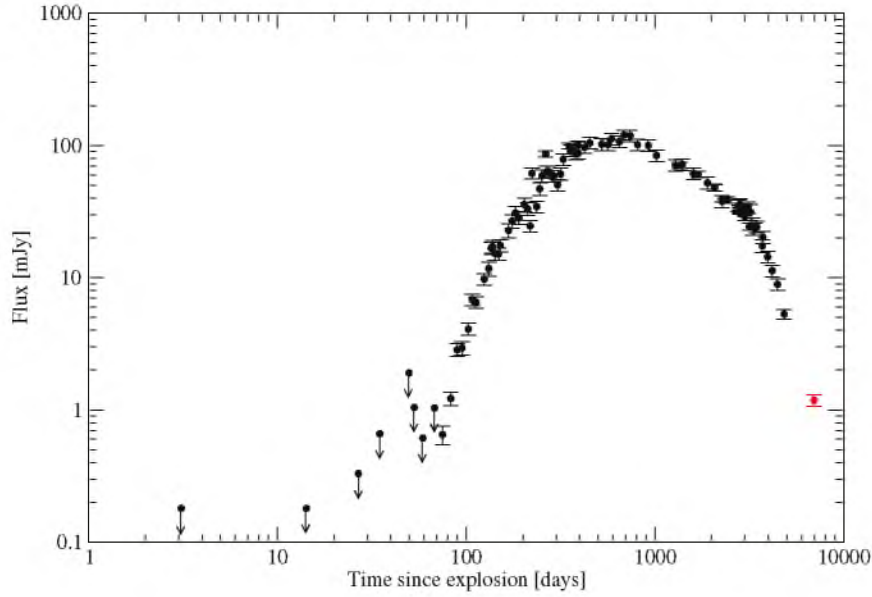
75

Figure 4.10: Radio light curve for SN1993J. Black data points were taken form Weiler *et al.* (2007) (arrows indicate the upper flux limit). The red point shows the new measurement after 6967 days since explosion (see text for details).

4.3.4 RM Synthesis

Thanks to rotation measure synthesis technique (Sec. 1.3.3), it is possible to obtain a distribution of polarized intensity as a function of Faraday depth. For the purposes of analysis presented in this chapter, the original Q and U data cubes from the L band data were convolved to the spatial resolution of 40" to increase the signal-to-noise ratio of the polarized signal. In the figure 4.11, I present two distinct Faraday depths for which polarized signal from M 81 was detected. The brightest diffuse intensity is observed at Faraday depth of about -30 rad m^{-2}. Its distribution is divided along major axis into south-western and north-eastern parts of the galaxy. In the former the intensity is brighter than in the latter. A similar asymmetry in the observed distribution of polarized intensity along the major axis was also reported by Krause *et al.* (1989b).

The opposite situation can be observed at the Faraday depth of around of +17.5 rad m^{-2}. Here, the north-eastern part of the galaxy is brighter, while its western side is nearly void of polarized emission. Such a value of Faraday depth (of +17.5 rad m^{-2}) was not earlier seen for M 81 (see Krause *et al.* work). Both the values of Faraday depths are of the same order of magnitude as these studied by Braun *et al.* (2010) and suggest that the medium responsible for Faraday rotation fills relatively small part of the total line of sight.

The best way to characterize a polarized emission along a given line of sight is to obtain its Faraday spectrum (Sec. 1.3.3). The distribution of the polarized signal visible at +17.5 rad m^{-2} was divided into three separate regions (Fig. 4.12), then for each of the regions an average Faraday spectrum was computed across the entire sampled range of Faraday depths. The results are shown in the figure 4.12. For the region number 1, the dominant component of polarized signal with the centre at the depth of about -20 rad m^{-2} is broader than the width of the restoring beam (which is an equivalent of a point-like source). There also seems to be an additional component of signal shifted towards the positive values of rotation measure. In the averaged Faraday spectrum of the region 2, the broadening is even more enhanced. Here, the second Faraday component (besides the maximum located at about -20 rad m^{-2}) is nearly of the same magnitude as the main one. Its position can be roughly estimated as +20 rad m^{-2} (note that the peak shifted most to the right is probably not real). In the region 3 located in the south-western part of the galaxy, only a single point-like structure of Faraday spectrum is observed. However, it has possibly an additional low amplitude (when compared to the main peak) com-
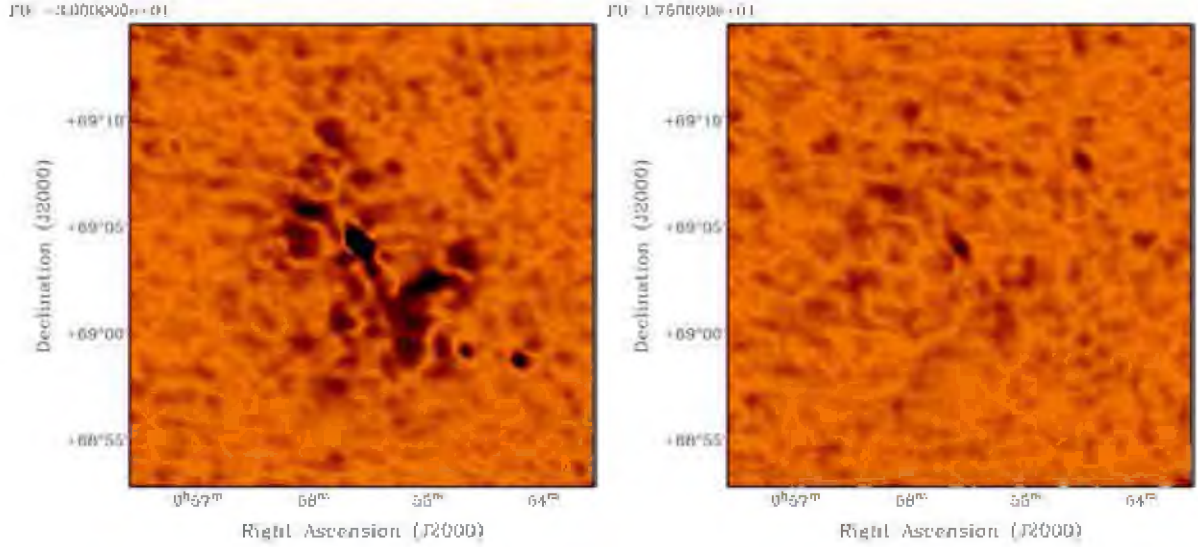
Figure 4.11: Particular Faraday depths (-30 and +17.5 rad m^{-2}) from L band data for which a polarized emission of M 81 is detected. The resolution is 40" × 40". Both maps are shown in the same intensity scale.

ponent located at the positive Faraday depths. Such double peaked/extended structures were already detected in the central regions of a number of spiral galaxies observed in a frame of the WSRT-SINGS survey (Heald *et al.* 2009). Furthermore, in this survey, also well-separated (by about 200 rad m^{-2}) disk polarized emissions at three distinct depths were seen in NGC 628, NGC 5194 and NGC 6946 (Braun *et al.* 2010). Braun *et al.* interpreted these observations as an emission coming from two spatially separated regions located at the near and far sides of the galactic mid-plane. The radiation from the further side was much weaker and had larger absolute values of Faraday depths than the main component coming from the side of disk closer to the observer, which had a Faraday depth of an order of tens rad m^{-2}. The only two Faraday components detected in M 81 to possess low (absolute) values of Faraday depths could suggest that they come from the same (closer to the observer) side of the galaxy.

In order to obtain polarized intensity and B-vectors distributions in M 81, the position of Faraday depth related to the maximum of PI signal along a particular line of sight was determined, which provided a distribution of maximum Faraday depths (see below). Note that this is not a classical RM map as spectra along some lines of sight, may not be a single component (or a point-like one). For these particular Faraday depths once again the rotation measure synthesis was performed, resulting in the required maps (Fig. 4.13). The polarized signal detected (mainly at the 3 σ noise level) from the galaxy is located mostly in the interarm regions. This is typical for spiral galaxies (Sec. 1.1). Moreover, some patches of the polarized signal are visible also in the outer parts of the spiral arms. Such a location of polarized intensity (but much more clearly visible) was found by Chyży *et al.* (2007b) for the galaxy NGC 4254. In the nucleus, the emission is very bright and extends from the south-western to north-eastern direction. This structure can be partly connected with the AGN. No polarized emission in the northern and southern part of the object has been detected.

The directions of the observed B-vectors are quite smoothly distributed over the galaxy. In some places, they are perpendicular to the spiral arms, which is most likely due to Faraday effects in the object itself and/or foreground magnetized plasma. It is worth to note that their directions roughly agrees with the directions of B-vectors shown by Krause *et al.* (1989b) at
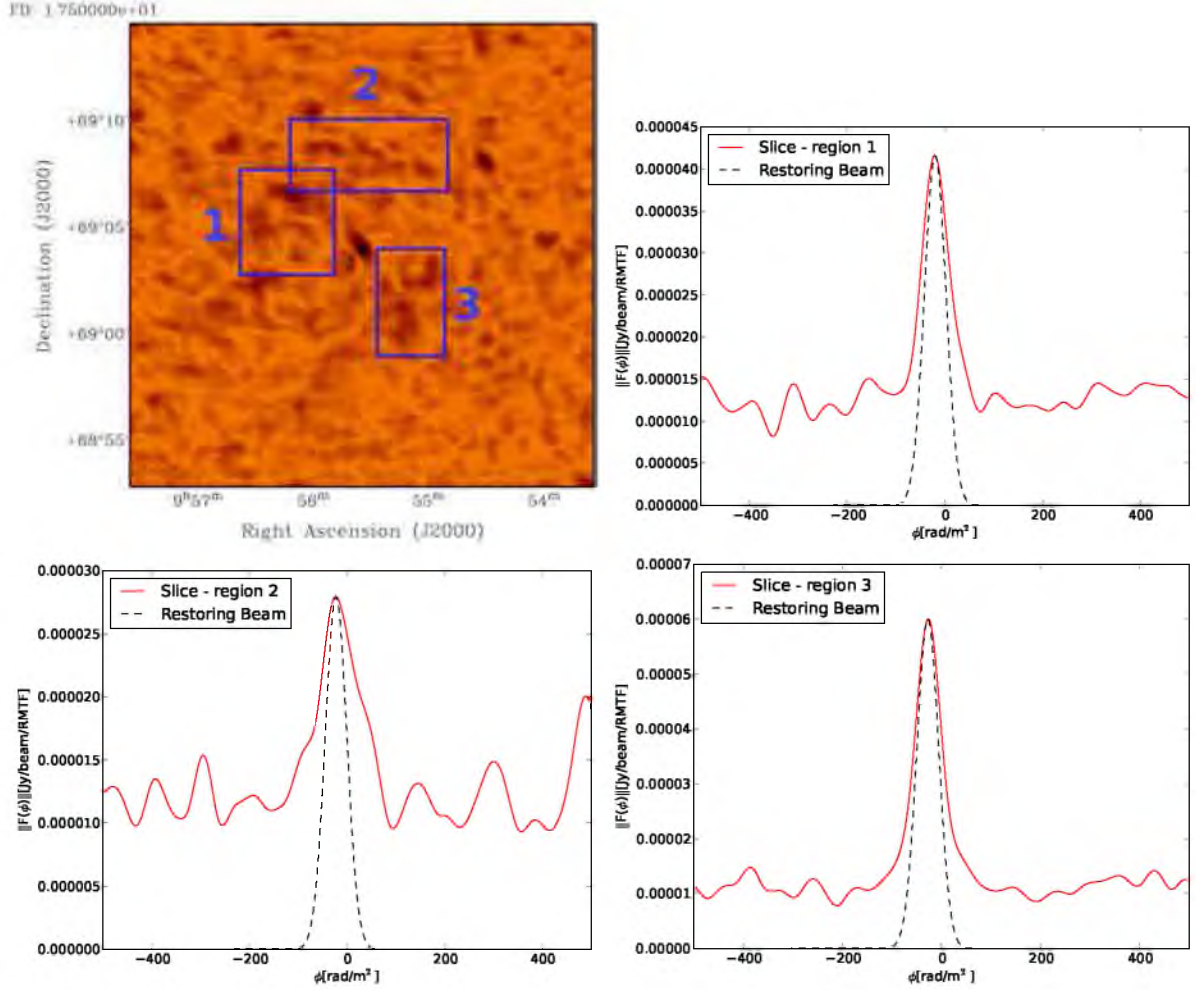
Figure 4.12: Three regions across of M 81 at the Faraday depths of $+17.5\,\mathrm{rad\,m^{-2}}$ for which Faraday spectra (from L band data) averaged in the marked boxes were measured. For each spectrum, a restoring beam scaled and shifted to the largest peak is plotted.

nearly the same frequency as that presented here.

In the maximum Faraday depth map obtained for M 81 (Fig. 4.14) there is a rather noisy distribution of values, which are mostly negative. This indicates that the magnetic field in general is directed away from the observer. The map will be used below to determine a large-scale pattern of magnetic field of the galaxy. Having distribution of maximum Faraday depths and assuming that they are (in most of the regions where PI emission was detected) single and point-like, the true directions of magnetic fields can be obtained (Fig. 4.15). They are generally aligned with the optical spiral arms (especially in the southern part), as it was already shown by Krause *et al.* (1989b), which is typically observed for spiral galaxies (e.g. Beck & Wielebinski 2013).

The RM Synthesis was also performed for the WSRT data (Sec. 4.2.2). The input Q and U cubes were convolved to the resolution of 150" to increase a signal-to-noise ratio. Scanning along Faraday axis through the resulting RM cube of resolution of $84\,\mathrm{rad\,m^{-2}}$ reveals only a single point-like component localized around a depth of $-20\,\mathrm{rad\,m^{-2}}$.

In the figure 4.17, a map of PI distribution with resolution of 150" from WSRT data is presented, which was obtained in a similar way as the distribution in L band shown in figure 4.13. The map covers a huge area of the central part of the M 81 group. The most noticeable

Figure 4.13: Polarized intensity (corrected for the primary beam) contours and B-vectors of M 81 (Briggs Robust weighting of 0.5) in L band obtained for Faraday depths for which maximum polarized signal could be detected (see text), superimposed on the DSS blue image. The contour levels are $(3, 5, 8, 16, 32) \times 20\mu$Jy/beam. The map resolution is 40" $\times$ 40" HPBW.

Figure 4.14: Maximum Faraday depth map of M 81 (in rad m^{-2}; see text for details). The map resolution is 40" $\times$ 40".
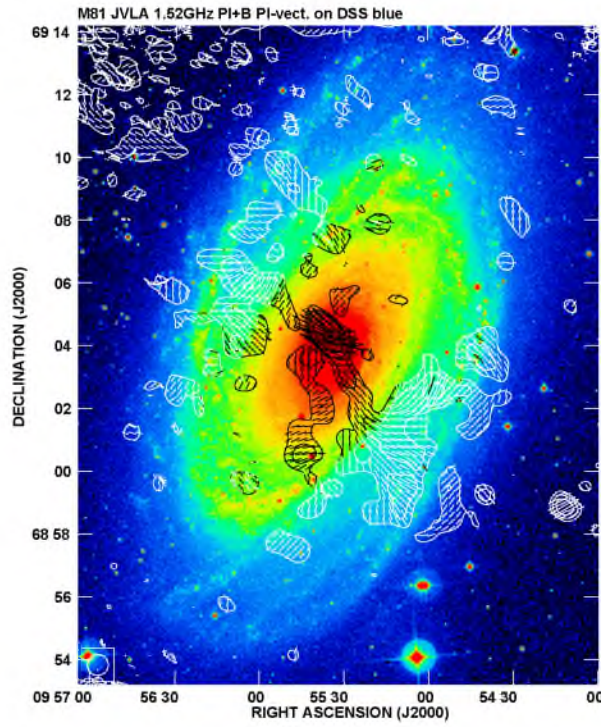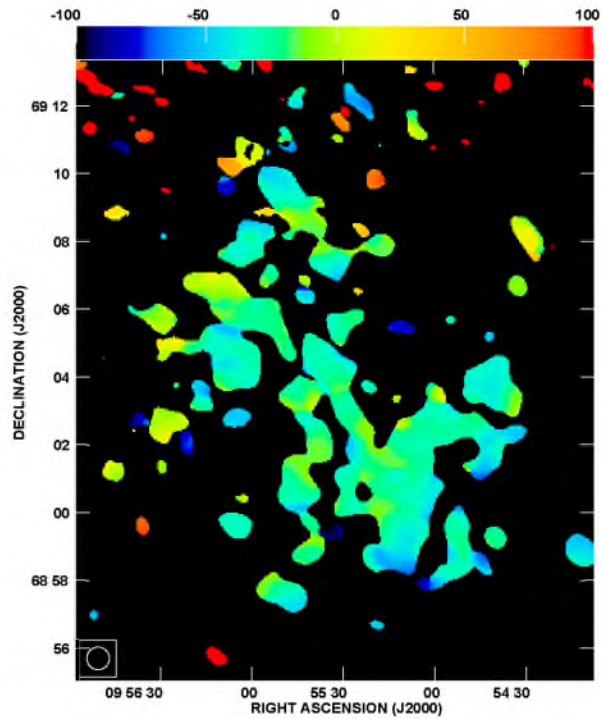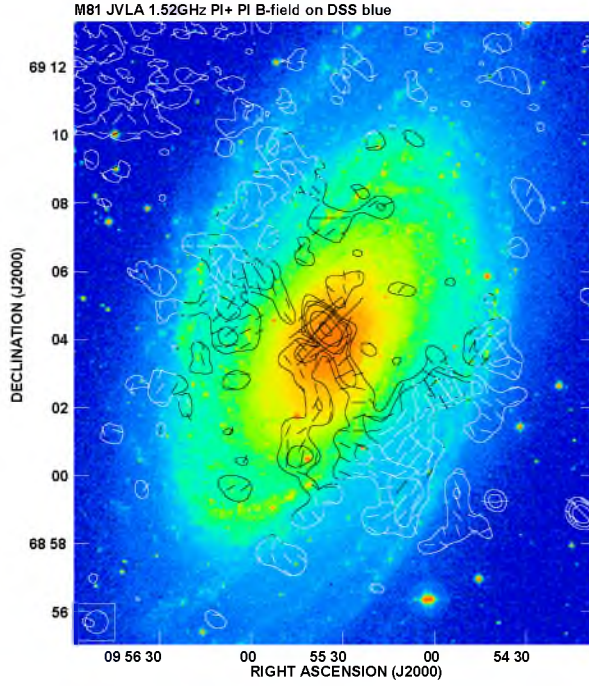
79

Figure 4.15: Polarized intensity (corrected for the primary beam) contours and B field vectors of M 81 (Briggs Robust weighting of 0.5) in L band superimposed on the DSS blue image. The contour levels are (3, 5, 8, 16, 32) × 20μJy/beam. The map resolution is 40" × 40" HPBW.

is a strong diffuse polarized emission filling the whole field of view of the instrument, which can suggest that the polarized signal might be related to the magnetic field of the Milky Way, instead of the M 81 group. As it was pointed out above, most of the detected PI comes from the Faraday depth of about -20 rad m^{-2}. This relatively low value additionally points to the Milky Way's origin of the signal, as similar detections of strong polarized emission from the Galaxy at this frequency are common (e.g. de Bruyn & Brentjens 2005; Brentjens 2008; Pizzo *et al.* 2011).

As I have shown, for the galaxy IC 10, the Milky Way PI signal can be detected even at frequency as high as 1.43 GHz (Sec. 3.3.2). In the case of M 81, the Milky Way emission was not observed directly in 1-2 GHz frequency band, which can be explained by the fact that the object is located much further (galactic latitude of about + 40°) from the Galaxy plane than IC 10. Lower frequency observations are needed to see lower-energy electrons and weaker magnetic fields of the Galaxy in the direction of M 81.

A more detailed comparison of the polarized and total power distributions in the WSRT data reveals that there can be also some PI signal related directly to M 81 (Fig. 4.17, 4.18). This signal is in fact the brightest diffuse polarized structure to be seen in the available field of view. The maximum of this emission corresponds well with the interarm region of the object (Fig. 4.17, 4.18). Such a localization of PI emission, in the interarm space, is characteristic for the observations of nearby spiral galaxies (Beck & Wielebinski 2013). Furthermore, the rest of this bright diffuse polarized structure also corresponds with the object's disk, which can suggest that this emission is at least partly related to the galaxy and not to the Milky Way. A better resolution in the Faraday space is needed to confirm the above hypothesis.

4.4 Discussion

4.4.1 Strength of magnetic field within and around M 81

Observations of the M 81 galaxy in the low-frequency band of 324 MHz provide a great opportunity to see directly its non-thermal emission. At such frequencies, contribution from the
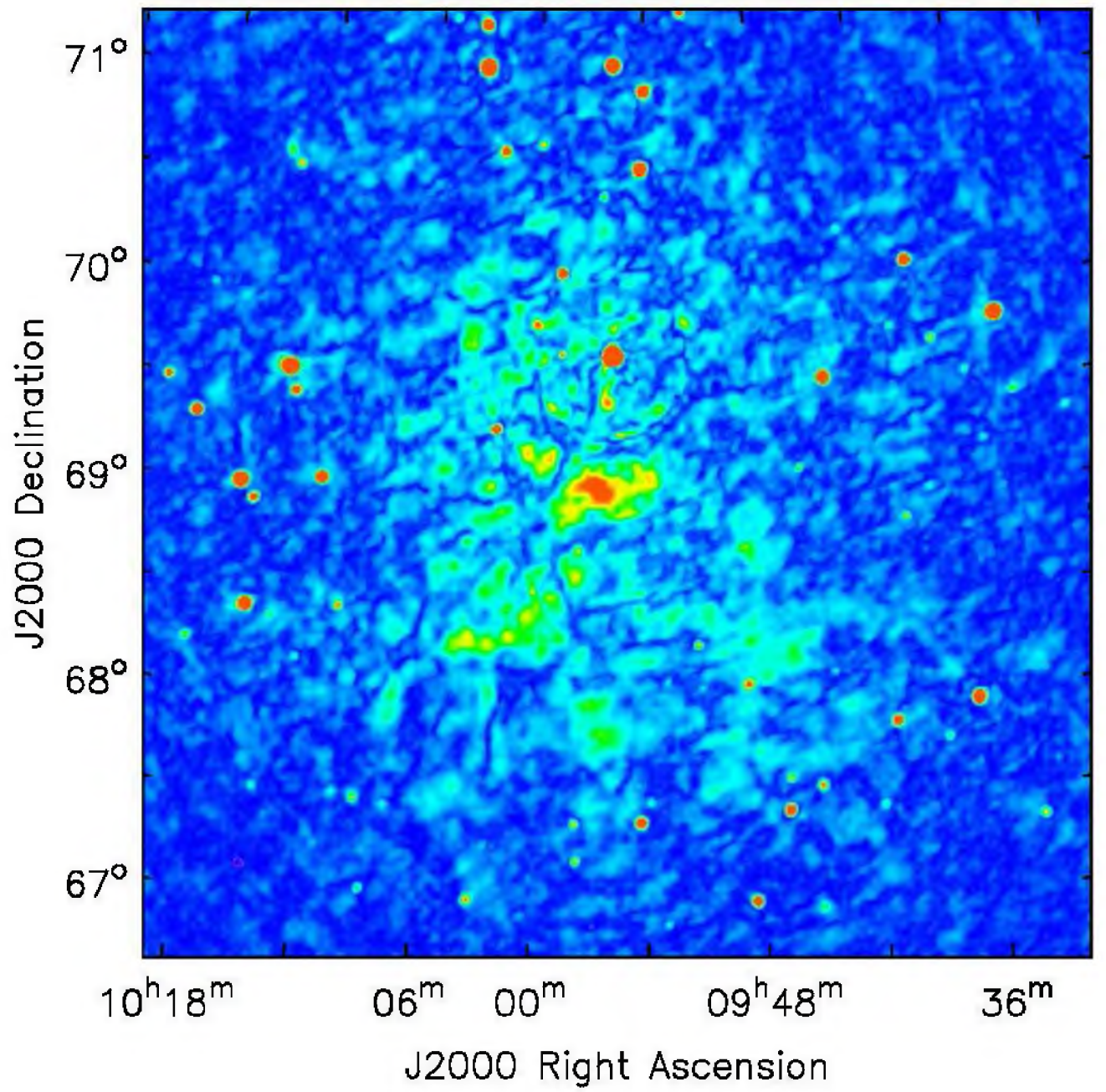
Figure 4.16: Polarized intensity map at around (see text) 324 MHz for M 81 and its neighbour-hood.
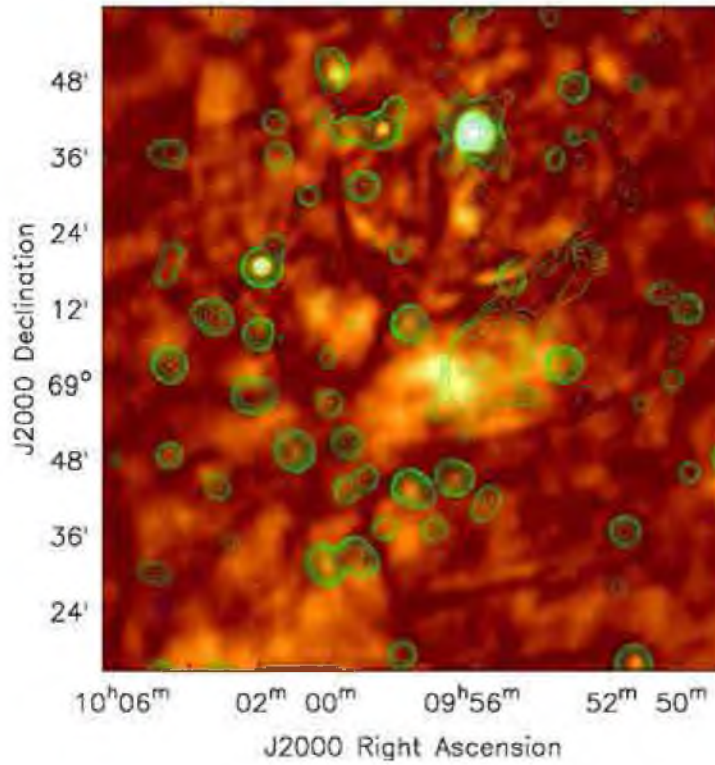
Figure 4.17: Total-power map of M 81 at 324 MHz superimposed on the PI map. Countor levels are (-5, -3, 3, 5, 8, 16, 32, 64, 128, 256, 512, 1024, 2048, 4096) × 1.5 mJy/beam. The maps resolution is 150".
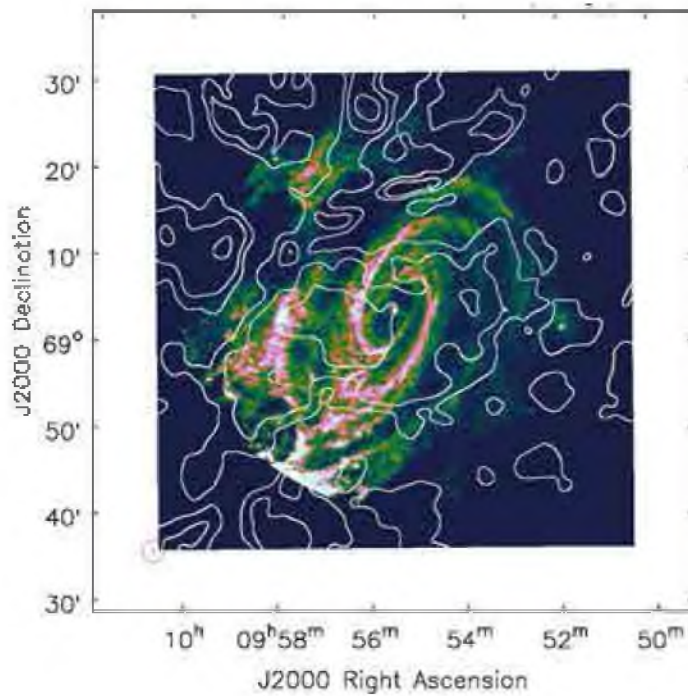
Figure 4.18: Polarized intensity map of M 81 at around (see text) 324 MHz superimposed on HI map (from THINGS survey; Walter *et al.* 2008). Contour levels are (3, 5, 8, 16, 32, 64, 128) × 0.55 mJy/beam. The PI map resolution is 150".

thermal emission is negligible (cf. Krause *et al.* 1989b), thus the magnetic field strength (cf. Sec. 1.3.1) can be determined directly from the observed radio radiation. In calculating the mean total magnetic field, the disk thickness was assumed to be 1 kpc and then corrected for inclination angle given in LEDA database. The non-thermal spectral index of 0.77 ± 0.12 was taken from Beck *et al.* (1985). The measurements of non-thermal radio brightness were performed within the the galaxy (not including nucleus and the background source, see Sec. 4.3.1) determined by the 3 σ noise level (of about 0.5 mJy/beam). Following the same assumption as for NGC 2976 and IC 10 (Sec. 2.4.2 and 3.4.3), according to the formulae given by Beck & Krause (2005), I obtained the average total magnetic field strength $B_{tot} = 6.0 \pm 1.6 \mu G$. Within uncertainties, this value is in an agreement with the field strengths obtained from the high-frequency observations of Beck *et al.* (1985) and Krause *et al.* (1989b). Such a relatively weak magnetic field was also found in M 31, which is another early-type galaxy with a moderate star formation rate (Beck & Wielebinski 2013). The weakness of the M 81's magnetic field is not obvious, if one keeps in mind that this is an interacting object (e.g. Yun *et al.* 1994), where more enhanced B_{tot} are expected. However, Drzazga *et al.* (2011) have shown that only in the advanced stages of galaxy interactions a small-scale dynamo is more efficient, leading to stronger total fields.

One long-standing problem is also that of existence of IGM magnetic fields in groups of galaxies (e.g. Nikiel-Wroczyński *et al.* 2013b). In the WSRT data covering most of the area of the central part of the M 81 group, there is no direct detection of radio emission, thus it is possible to estimate just an upper limit of magnetic field strength in the group. Under the same conditions as above but assuming a non-thermal spectral index of 0.8 and a thickness of region where magnetic field resides of 100 kpc (which is an order of magnitude of distances between central galaxies), the upper limit of magnetic field strength is 1.7 μG. As a detection limit of radio emission, I assumed a total-power brightness of 2.5 × r.m.s. noise level. If one would assume a thickness of 200 kpc, the field strength would be <1.4 μG. Otherwise, in the case of much older CR electrons, e.g. 1.3, one would obtain a field of <2.1 μG. So, under the above considerations, a reasonable value of the upper limit of magnetic field strength in the central part of the M 81 group can be set to about 2 μG.

A similar field limit was estimated recently for the Leo Triplet group, where also no diffuse radio emission was detected (Nikiel-Wroczyński *et al.* 2013b). It seems that with the currently available data, there is a chance to directly observe any magnetic field in between galaxies for compact galaxy groups only. An example can be Stephan's Quintet, where the field has the strength comparable to that observed in the normal galaxies (Nikiel-Wroczyński *et al.* 2013a). Observations at much lower frequencies (e.g. with LOFAR telescope) are needed to directly detect such a weak magnetic field as this estimated above for the M 81 group.

4.4.2 Magnetic field structure

The only way to recognize Fourier modes in large-scale magnetic field structure of galaxies is to determine variations of their rotation measures with azimuthal angle. This method applied to the RM map between 6 and 21 cm enabled Krause *et al.* (1989b) to discern the dominating bisymmetric field morphology in M 81 (Sec. 4.1). Here, this classical approach will be used to the maximum Faraday-depth map, which resembles a rotation measure distribution under some assumptions (cf. Sec. 4.3.4). In the figure 4.19, the azimuthal distribution of the averaged Faraday depths measured in 30 degrees-wide sectors are shown. Sector 0 represents the starting point localized along the major axis of the galaxy in its northern part. All the measurements, corrected for position and inclination angles (from LEDA database), were performed in the
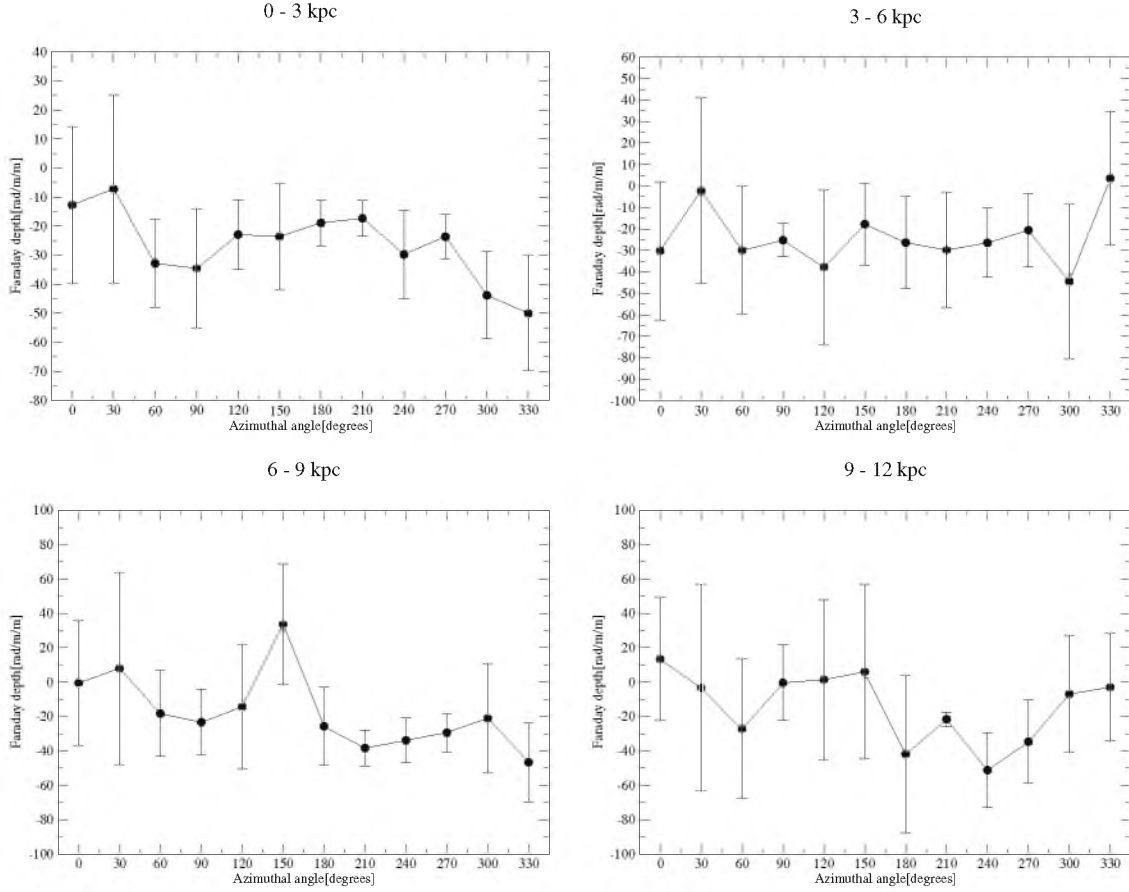
Figure 4.19: Measurements of maximum Faraday depth versus azimuthal angle for M 81 in the following four radius ranges: 0-3 kpc, 3-6 kpc, 6-9 kpc and 9-12 kpc (see text for details).

sectors going from the northern to the eastern directions in four of the following ranges of galactic radius: 0-3, 3-6, 6-9, 9-12 kpc.

For the BSS structure of magnetic field, one would expect a double sinusoid in the distribution of Faraday depths (RMs) vs. azimuthal angle (e.g. Krause *et al.* 1989b). Moreover, according to the numerical simulations of Moss *et al.* (1993), the BSS field should dominate in the outer parts of the object. However, no clear signatures of such a distribution can be seen in the data presented. There is also no visible single-period sinusoid, expected for axisymmetric structure of magnetic field. Such a pattern is the most commonly observed one in the spiral galaxies (Braun *et al.* 2010) and it was also recognized for the LMC (Gaensler *et al.* 2005). This result could indicate that in M 81, there is no dominating Fourier mode in the magnetic field morphology or that the signal-to-noise ratio is too low for it to be recognized. In the presented L band data, there is much less diffusive polarized emission detected than in the Krause *et al.* (1989b) work.

In order to increase S/N ratio of the original Q and U data cubes, I convolved them to the resolution of 150" (i.e. resolution of RM distribution map presented by Krause *et al.* 1989b). Then the RM Synthesis and the whole analysis[6] were repeated for these data (not shown here),

---

[6]These data were not corrected for the primary beam attenuation. Furthermore, during the RM Synthesis, a uniform (classical) weighting was used. Both the restraints are due to the relatively large angular size of the object with respect to the field of view of the instrument.

Table 4.3: Maximum Faraday depths of polarized background sources around M 81

R.A.(J2000.0) "h:m:s"	Dec.(J2000.0) "d:m:s"	Faraday Depth rad m^{-2}	Single component and pointlike?
09 57 47.96	+69 10 36.9	-25.0	yes
09 54 45.30	+69 17 43.0	-15.0	yes
09 53 10.49	+69 03 56.7	-37.5	no
09 54 11.93	+68 58 50.0	-45.0	no
09 56 22.46	+68 46 00.9	-32.5	no

but still no clear signatures of dominating dynamo mode could be seen.

The lack of clear signatures of dominating dynamo mode in the presented data could also be accounted for by some physical processes, among others, the fact that in the L band dispersion function, determined for M 81, multiple point-like or extended components are likely present (Sec. 4.3.4). This indicates that along the line of sight there can be multiple Faraday thin or a Faraday thick regions of emission, where the radio-emitting plasma is mixed with that responsible for Faraday rotation. Such a multi-component distributions of Faraday dispersion functions were found for the the brightest galaxies (NGC 628, NGC 5194, NGC 6946) of the WSRT-SINGS survey. However, in contradiction to M 81, they clearly indicated a dominating axisymmetric magnetic field geometry (Braun *et al.* 2010). In the case of M 81, the dispersion functions along the particular line of sight do not indicate any single dynamo mode. This can be due to a more complicated morphology of the field in the object than in the other spirals observed to date (cf. Sec. 4.3.4).

It needs to be recalled that M 81 resides in the centre of the galaxy group, where signatures of gravitational interactions are well visible (e.g. Yun *et al.* 1994; Chynoweth *et al.* 2008). It is known that tidal interactions seriously modify structures of magnetic fields in galaxies (Chyży & Beck 2004; Drzazga *et al.* 2011). Thus, no detection of clear signatures of any particular field morphology in M 81 can indicate that the interactions introduced perturbations to the regular magnetic field component. Such perturbations or disruptions of large-scale magnetic field patterns are commonly observed in interacting galaxies (e.g. Beck & Wielebinski 2013). More sensitive data in a wider range of frequencies are needed to better understand the complicated case of magnetic field in M 81.

It is also possible that the unclear picture of magnetic field morphology in M 81 is caused by a complex contribution to the Faraday rotation from the Milky Way. Krause *et al.* (1989b) estimated the foreground RM of -9 ± 5 rad m^{-2}. They assumed that this value is constant across the entire M 81. However, the results of the section 4.3.4 show that it may be not the case, as the presented low-frequency data reveal a rather highly non-uniform distribution of polarized emission. One may suspect that a similar situation will occur also for the component of magnetic field parallel to line of sight and thus for Faraday rotation. Furthermore, the Faraday spectra obtained for five background sources in L band data (Table 4.3) reveal that the Faraday depths of maximum of polarized signal are lower than the value given by Krause *et al.*. Some of these sources show multiple components or extended spectra, which can further point to the complicated Milky Way contribution to RM towards the object. The low-frequency LOFAR observations of M 81 field and its excellent resolution in Faraday depth (of about 1 rad m^{-2}) can provide crucial clues about the Milky Way magnetic field in this region of the sky.

4.5 Conclusions

Deep spectro-polarimetric radio observations of M 81 with JVLA and WSRT in L and 92 cm bands (respectively) were performed. The main conclusions are as follows:

- The high-resolution L band JVLA observations of M 81 show that its total power emission is closely related to the giant HII regions. There is no diffuse emission observed within this object except for the internal part of the western arm.

- The rotation measure synthesis performed for the galaxy, using the JVLA data, reveals that mostly in the north and north-eastern part of the object, likely at least two components (or one extended component) of Faraday dispersion function are visible. With the available data sensitivity, it is not possible to confirm that the topology of magnetic field in the galaxy is of BSS type.

- The low-frequency polarimetric data in 92 cm band from the WSRT for galaxy M 81 reveal a total-power emission closely related to its optical disk with an extension similar to that observed at higher frequencies (in L band). The RM Synthesis applied to the data reveals a bright polarized emission component coming from the Milky Way. Perhaps there is also some PI signal to be observed from M 81, but a higher resolution in Faraday domain is needed to confirm this.

- The mean total magnetic field estimated for the object is $6.0\mu G$, which is in agreement with the values reported previously by Beck *et al.* (1985) and Krause *et al.* (1989b).

- There is no detection of radio emission coming from the intergalactic space of the central part of the M 81 group. The upper limit of magnetic field estimated for this region is $2\,\mu G$, which is similar to estimations made by Nikiel-Wroczyński *et al.* (2013b) for the Leo Triplet group.

- The morphology of L band radio emission obtained for the nucleus of M 81 resembles that to be seen in the previous observations of Kaufman *et al.* (1996), except for the bridges connecting the central part and the arc.

- I detected the famous supernovae SN1993J in M 81 in the L band JVLA data. Its radio flux added to the light curve available from the literature follows the trend determined by the previous observations. This supports the model of shape of light curve simulated by Marti-Vidal *et al.* (2011a) with long mean lifetime of relativistic electrons.

Chapter 5

Summary and Conclusions

I performed a data reduction, followed by a detailed analysis, of radio polarimetric observations from VLA, Effelsberg, WSRT and JVLA instruments for three galaxies NGC 2976, IC 10 and M 81, of interest from the point of view of their magnetic field morphology. These observations were supplemented with the re-reduced data for the sub-sample of six (including NGC 2976) galaxies from the WSRT-SINGS survey (Heald *et al.* 2009). A significant part of the analysis was based on the novel technique of RM Synthesis.

Each of these three galaxies, in contrast to the WSRT-SINGS objects, reveals a distinct influence of galactic-scale winds or tidal/ram pressure interactions on the magnetic field structure. In particular, the field morphology discovered in NGC 2976 involves a southern polarized ridge and a northern extension. These structures seem not to due to just a pure large-scale dynamo process (possibly CR-driven) at work in this object, as indicated by the RM data and dynamo number calculations. Instead, the field of NGC 2976 is modified by past gravitational interactions and possibly also by a ram pressure inside the M 81 galaxy group environment. The estimates of total $(7\,\mu G)$ and ordered $(3\,\mu G)$ magnetic field strengths as well as field regularity (0.46), similar to those observed in spirals, show that tidally generated magnetized gas flows can further enhance dynamo action in the object.

In IC 10, an extended radio envelope far off the stellar disk, is detected at 1.43 GHz in the total-power emission. In turn, the polarized emission reveals an unexpected X-shaped morphology of magnetic field, observed so far only in the spiral galaxies. Both these findings suggest a presence of galactic wind in this object, which is confirmed by the calculated bulk speed of CRs of about 150-300 km s^{-1}, much higher than its escape velocity (of about 40 km s^{-1}). More questionable is an action of large-scale dynamo in IC 10. The available RM data and the estimations of dynamo number do not allow to make any conclusive judgment here. The strong magnetic field of about $14\,\mu G$ estimated for the object, comparable to that in bright spirals, can be due to an effective action of small-scale dynamo only. Also in IC 10, similarly like in NGC 2976, some of magnetic field structure (in the southern part of the object) can be a consequence of ordered gas flows.

The configuration of magnetic field in M 81 seems to be a complicated one. This is manifested mostly in the northern and north-eastern part of the object where multiple (or a single extended one) components in Faraday spectrum are observed. With the sensitivity of available data it was not possible to confirm that the magnetic field of the object is dominated by the BSS dynamo mode. The fields' morphology in M 81 can be due the interactions between the galaxy and other central galaxies of the M 81 group in the past.

To summarize, it can be concluded from the studies performed in this thesis that the galactic winds have a crucial influence on the formation of large-scale structure of magnetic field in

dwarf galaxies as it was shown for IC 10. The same applies to the tidal interactions (and ram pressure), which influence can lead to formation of an unusual field morphology (a polarized ridge) out of the star-forming disk, not following any observed ISM component as in the case of NGC 2976. The gravitational interactions can cause also disturbances in the dynamo modes as it takes possibly place in M 81.

I also found that IC 10 and NGC 2976 are apparently good candidates for the IGM magnetization. Despite their different linear sizes (though both are much smaller than spiral galaxies), they are able to provide ordered (perhaps also regular) magnetic field into the intergalactic space (up to a distance of about 5 kpc). The plasma ejected by galactic wind from IC 10 and by gravitational interactions from NGC 2976 gives us some insight into the processes that are thought to be common in the early Universe. M 81 as weakly interacting with other galaxies of the central part of the group does not possess any distinct signs of pulling out magnetic field into the IGM, which indicates that the galaxies in early stages of interactions are not significant IGM magnetizers.

A new weighting scheme for RM Synthesis algorithm was proposed and investigated. It consists in including information about the quality of data in individual frequency channels. Application of this new weighting to the simulated data as well as to the observed ones results in an improvement of the signal-to-noise ratio in the Faraday depth space. Its only drawback is a slight increase of width of the main lobe of RMTF.

There is a number of fundamental problems of galactic magnetism yet to be resolved. From what we know today, it seems that the domain of polarimetric observations of nearby galaxies falls in frequencies higher than 1 GHz. Observations at such frequencies are currently possible with the new generation of spectro-polarimetric instruments like JVLA and in the near future, SKA, which will allow to perform the rotation measure synthesis in a wide wavelength range, as shown for M 81. Thus we will be able to solve problems in determining magnetic field structure of galaxies as those encountered in the 1.43 GHz observations of IC 10. On the other hand, the studies of weak magnetic fields, as those estimated for the central part of the M 81 galaxy group, require observations at much lower frequencies than 1 GHz. Such a possibility has been now created by LOFAR – the radio interferometer located across Europe.

Appendix A

Re-analysis of the subsample of WSRT-SINGS galaxies

In this appendix, I present the procedures and results of re-imaging WSRT data for the sub-sample of galaxies from the WSRT-SINGS polarimetric survey[1] (Heald *et al.* 2009; see Sec. 2.1). The calibrated WSRT-SINGS polarimetric uv data in the 18 cm and 22 cm bands (for details see Heald *et al.* 2009) were re-imaged by applying the Miriad software with usage of the Briggs robust weighting of 1.0. The Q and U frequency data cubes obtained in this way (not corrected for the primary beam attenuation, except for NGC 2976) were convolved to the resolutions given in Table A.1, providing a high sensitivity to extended radio structures. Then for the Q and U data cubes RM Synthesis was performed (for NGC 2976 the new weighting scheme was used, see Appendix B for details).

The resolution in the Faraday depth obtained for a frequency coverage of the WSRT-SINGS survey is about 144 rad m^{-2}, whereas the sensitivity for extended structures (for which 50% of polarized flux can be recovered) is about 110 rad m^{-2}. The maximum Faraday depth that could be sampled in the Faraday domain is about 1.7×10^5 rad m^{-2}. As no polarized emission at such high depths is expected, the Faraday domain was sampled within a range from -500 to +500 rad m^{-2} every 2.5 rad m^{-2}. As the RMTF shows a high level of side-lobes (of about 80%, cf. Sec. B.4) due to the gap in frequency coverage between 18 cm and 22 cm data bands, the RM cleaning method (Heald *et al.* 2009) had to be used. With this algorithm, the Q(ϕ) and U(ϕ) cubes were cleaned down to the 1-sigma noise level and then restored with a Gaussian beam of the same width as the main RMTF lobe. After cleaning Q and U data cubes, I calculated for the

---

[1] The results for NGC 2976 are described in section 2.3.5.

Table A.1: Basic properties of the WSRT-SINGS data for the studied galaxies

Name	Beam [" × "]	r.m.s.(PI) [μJy/beam]	No. of freq. chan. used for RM Synthesis
NGC 2976	48.6 × 45.0	25	702
NGC 0925	81.5 × 45.0	35	770
NGC 2403	49.5 × 45.0	30	765
NGC 3198	63.0 × 45.0	30	765
NGC 4559	95.9 × 45.0	25	658
NGC 5033	75.6 × 45.0	25	766

Figure A.1: Contours and B-vectors of polarized intensity of NGC 0925 from the WSRT-SINGS data superimposed on the DSS blue image. The contour levels are $(3, 5) \times 35\mu$Jy/beam. The vector of 10" length corresponds to the polarized intensity of about $31.3 \,\mu$Jy/beam. The map resolution is 81.5" $\times$ 45.0" HPBW.
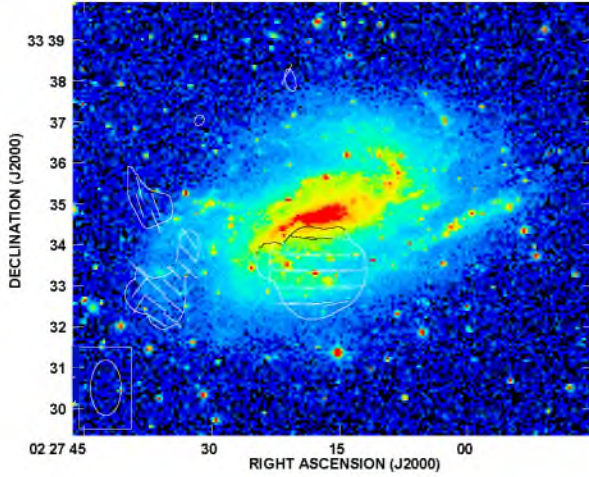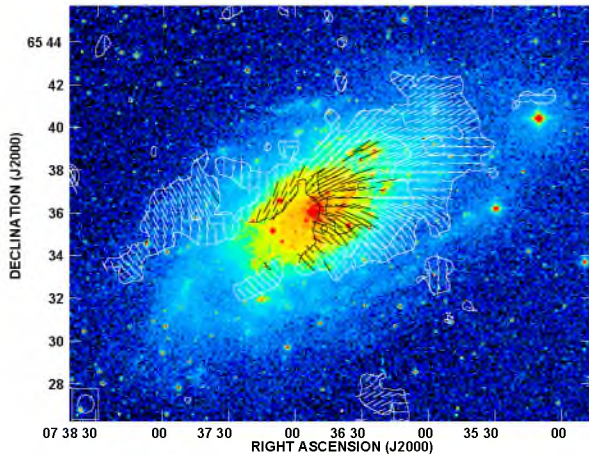

Figure A.2: Contours and B-vectors of polarized intensity of NGC 2403 from the WSRT-SINGS data superimposed on the DSS blue image. The contour levels are $(3, 5) \times 30\mu$Jy/beam. The vector of 10" length corresponds to the polarized intensity of about $31.3 \,\mu$Jy/beam. The map resolution is 49.5" $\times$ 45.0" HPBW.

studied objects the PI (not corrected for the positive bias), B-vectors, maximum Faraday depth and magnetic field vector distribution maps in the same way as described for M 81 in section 4.3.4. Below I present results obtained for each of the five WSRT-SINGS galaxies. Table A.1 provides a summary of the observations.

A.1 NGC 0925

NGC 0925 is a late-type galaxy with weak spiral arms and a bar (e.g. Pisano *et al.* 2000). The re-imaged WSRT-SINGS data do not reveal nearly any polarized signal for this object (Fig. A.1). This is quite surprising as the galaxy shows a quite high SFR of about 2.4 M$_\odot$ / yr (Table 2.1) and rotation velocity of about 120 km s^{-1} (de Blok *et al.* 2008), which should create good conditions for a large-scale dynamo.

A.2 NGC 2403

NGC 2403 is a SABcd-type galaxy (Table 2.1), compared often to M 33. There are no signatures of tidal interactions within this object, despite the fact that it is located in the NGC 2403 galaxy group (Chynoweth *et al.* 2009). In the WSRT-SINGS data, a substantial amount of a low-level (3σ) polarized emission is detected (Fig. A.2). As it can be seen, PI is characteristically located mostly in the western part of the galaxy's disk. The opposite side of the object
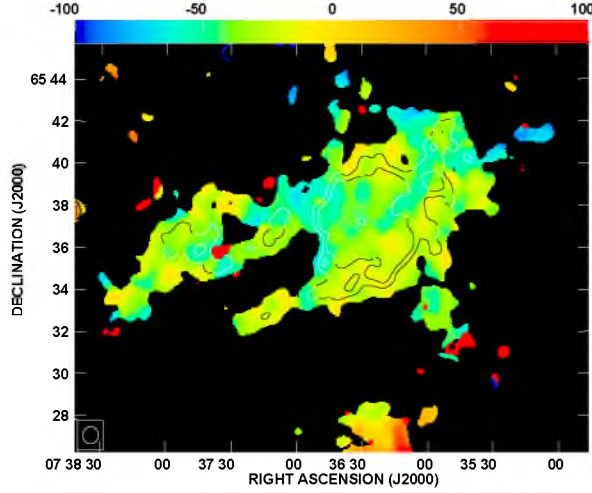
Figure A.3: Distribution of Faraday depths (in rad m^{-2}) for the maximum of polarized intensity signal for NGC 2403. The contour levels representing the polarized intensity are: (4, 5) × 30 μJy/beam. The map resolution is 49.5" × 45.0" HPBW.
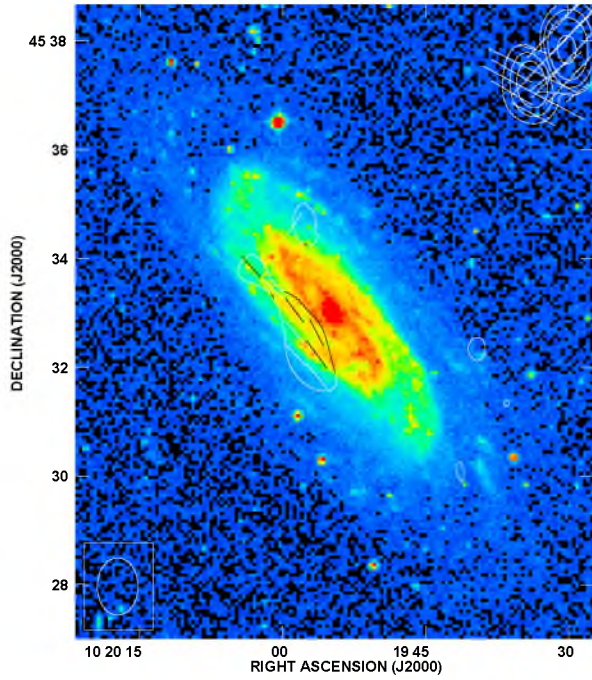

Figure A.4: Contours and B-vectors of polarized intensity of NGC 3198 from the WSRT-SINGS data superimposed on the DSS blue image. The contour levels are (3, 5, 8) × 30μJy/beam. The vector of 10" length corresponds to the polarized intensity of about 31.3 μJy/beam. The map resolution is 63.0" × 45.0" HPBW.

(coincident with the receding part of the major axis) is nearly void of polarized emission. This is in agreement with the model of magnetic field proposed by Braun *et al.* (2010). The orientations of magnetic field vectors form a spiral (Fig. 2.18c). This can also indicate the large-scale dynamo origin of the field of NGC 2403. There is just a single emission component in the Faraday spectrum of this galaxy. The map of the maximum Faraday depth distribution for this object shows mostly negative values (Fig. A.3). The RM of the Milky Way in direction of the galaxy is +11 ± 30 rad m^{-2} (Heald *et al.* 2009), indicating that the Faraday depths related directly to NGC 2403 are relatively low – like for the other WSRT-SINGS galaxies (Heald *et al.* 2009). This can be accounted for by a spatially thin layer of the magnetoionic medium, which causes the Faraday rotation of polarized vectors (Braun *et al.* 2010; cf. Sec. 4.3.4).

A.3 NGC 3198

NGC 3198 is a late-type galaxy with quite well-defined optical spiral arms. It belongs to the group of five galaxies but the tidal parameter indicates that it is not in a stage of interaction with
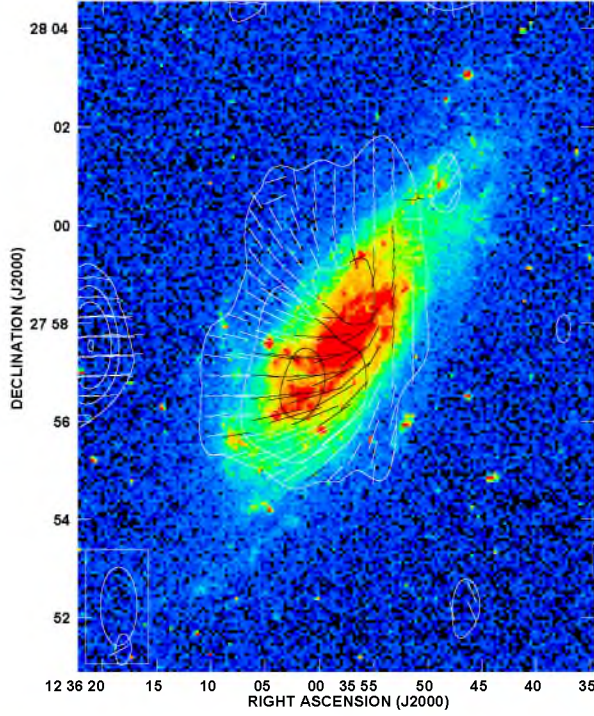
Figure A.5: Contours and B-vectors of polarized intensity of NGC 4559 from the WSRT-SINGS data superimposed on the DSS blue image. The contour levels are (3, 5, 8, 16) × 25μJy/beam. The vector of 10" length corresponds to the polarized intensity of about 31.3 μJy/beam. The map resolution is 95.9" × 45.0" HPBW.

the other groups members (Thilker *et al.* 2007). In this object, similarly like in NGC 0925, no strong polarized emission is detected (Fig. A.4) with the available sensitivity of 30μJy/beam (Table A.1). There is only some low-brightness (3σ) PI blob in the eastern part of the galaxy; however, it is difficult to judge if it is real or not. With the re-analysed data I do not confirm the possible detection of the nucleus indicated by Heald *et al.* (2009) in NGC 3198.

A.4 NGC 4559

NGC 4559 is a member of the Coma I galaxy group (Thilker *et al.* 2007). For this object, I detected a strong polarized emission located mostly in its south-eastern part (Fig. A.5). The opposite side of the galaxy, coincident with the receding major axis, shows a much weaker PI, which is in agreement with the model of Braun *et al.* (2010). NGC 4559 is an only object in the presented sample for which any extraplanar polarized emission is detected. It is located in the north-eastern part of the galaxy and has radially oriented magnetic field vectors (Fig. 2.18e). There is only a single Faraday component detected for this galaxy. The maximum Faraday depth distribution is quite smooth in NGC 4559 (Fig. A.6) and it is characterized by small values ranging from about -30 to +30 rad m^{-2}.

A.5 NGC 5033

NGC 5033 is a galaxy with well-defined spiral arms, containing a Seyfert nucleus in its centre (Ho *et al.* 1997). The polarized emission from the object is closely related to its optical disk (Fig. A.7). The orientations of magnetic field vectors form a spiral structure (Fig. 2.18f). There is no clear asymmetry in distribution of polarized emission along the major axis in this galaxy, which indicates a possible deviation of this object from the model of magnetic field morphology proposed by Braun *et al.* (2010). In the Faraday domain, there is just a single component. The distribution of maximum Faraday depths for the object (Fig. A.8) is a smooth one, which leads
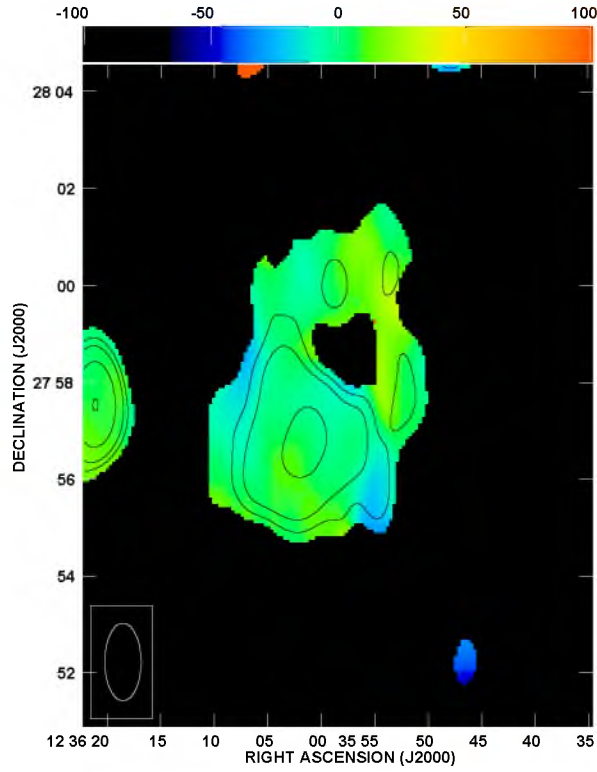
Figure A.6: Distribution of Faraday depths (in rad m^{-2}) for the maximum of polarized intensity signal for NGC 4559. The contour levels representing the polarized intensity are: (4, 5, 8, 16) × 25μJy/beam. The map resolution is 95.9" × 45.0" HPBW.
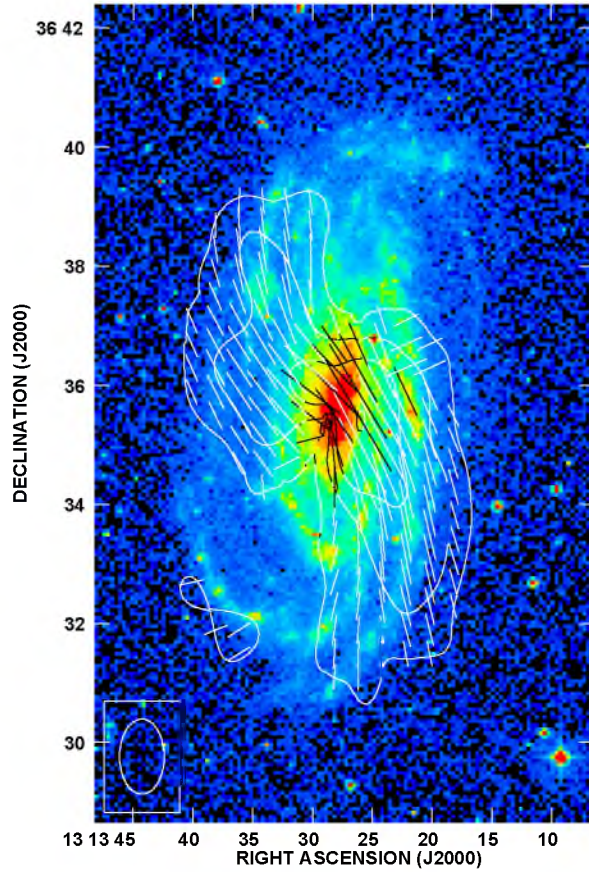

Figure A.7: Contours and B-vectors of polarized intensity of NGC 5033 from the WSRT-SINGS data superimposed on the DSS blue image. The contour levels are (3, 5, 8) × 25μJy/beam. The vector of 10" length corresponds to the polarized intensity of about 31.3 μJy/beam. The map resolution is 75.6" × 45.0" HPBW.
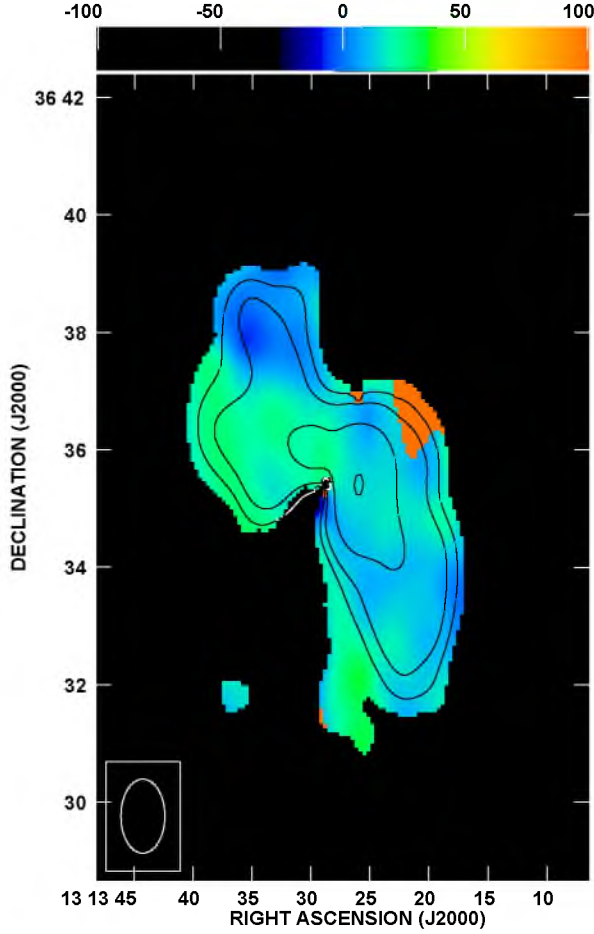
93

Figure A.8: Distribution of Faraday depths (in rad m^{-2}) for the maximum of polarized intensity signal for NGC 5033. The contour levels representing the polarized intensity are: (4, 5, 8) $\times$ 25μJy/beam. The map resolution is 75.6" $\times$ 45.0" HPBW.

to the conclusion that there is regular (large-scale dynamo generated) magnetic field in this galaxy.

Summarizing, the re-imaging of the WSRT-SINGS data for the sample of six objects (including NGC 2976) permitted to detect much more polarized emission in four of them (NGC 2976, NGC 2403, NGC 4559 and NGC 5033) than in the original work of Heald *et al.* (2009). For the other two galaxies (NGC 0925 and NGC 3198) nearly no polarized emission, except for some low-brightness PI blobs, is observed. Generally, for the four galaxies for which PI signal is seen a single component Faraday spectra are found. Furthermore, two of these galaxies (NGC 2403 and NGC 4559) show distinct asymmetries in distributions of polarized intensities, predicted by the model of magnetic field morphology proposed by Braun *et al.* (2010).

Appendix B

Application of radio interferometry weighting to RM Synthesis

Processing spectro-polarimetric data using RM Synthesis involves application of frequency channels weighting. The method currently used (I will call it the "classic" weighting scheme) consists in assigning weights of 1 to all the observed frequency channels and 0 to the others.

Obtaining the highest possible resolution in the Faraday domain requires observations in a wide spectral band (cf. Sec. 1.3.3). An example of this can be found in the WSRT-SINGS survey (Heald *et al.* 2009), where data were collected in the 18 and 22 cm bands simultaneously. As only the weights of 1.0 or 0.0 are assigned to the particular frequency channels according to the classic weighting, it is highly desirable to obtain a uniform r.m.s. sensitivity across the observed band. However, in practice, it can be difficult to meet this criterion, which was the case also for the mentioned survey (cf. Fig. B.8). Furthermore, sensitivities of individual channels wihin a single frequency band can considerably differ. This is often due to problems related to RFI or calibration errors. Thus, treating all (usable) frequency channels in the same way by assigning them the same weights of 1.0 seems not to be the most adequate solution. In this appendix, I present a novel approach to weighting data in rotation measure synthesis, which permits to take into account the individual channel sensitivities.

B.1   Introduction to the new weighting scheme

The rotation measure synthesis is similar to the radio interferometry (Brentjens & de Bruyn 2005; cf. Sec. 1.3.3). Therefore, one can try to write a formula for the RM Synthesis weight of j-th frequency channel in a similar way as for the single visibility data point in imaging aperture synthesis observations (e.g. Briggs *et al.* 1999):

$$w_j(\lambda_j^2) = \frac{R_j(\lambda_j^2)T_j(\lambda_j^2)D_j(\lambda_j^2)}{max(R_j(\lambda_j^2)T_j(\lambda_j^2)D_j(\lambda_j^2))} \tag{B.1}$$

In radio interferometry these three elements (of imaging weight) are defined as follows: R_j describes reliability of a given visibility (it is related to the data quality), T_j is a tapering function (related to the position of a given data point in the uv-plane) and D_j is a density weighting function. The last coefficient can be used to compensate a non-uniform distribution of data points in the uv-plane (for more details, see Briggs *et al.* 1999).

95

In RM Synthesis, we can apply similar weighting strategy and assume that R_j will describe a quality of an individual data point (i.e. Q and U Stokes parameters for a given frequency channel). I propose to approximate R_j by the following formula:

$$R_j(\lambda_j^2) = \frac{1}{\sigma_Q^2(\lambda_j^2) + \sigma_U^2(\lambda_j^2)} \qquad \text{(B.2)}$$

where, $\sigma_Q(\lambda_j^2)$ and $\sigma_U(\lambda_j^2)$ are the r.m.s. noise levels measured for a particular Q and U frequency channels, respectively. I have chosen $1/\sigma^2$ weighting, as it is widely used in statistical analysis and radio-interferometry (e.g. Briggs 1995, Briggs et al. 1999). Substituting $T_j = D_j = 1$ in formula B.1 gives an equivalent of the so-called natural weighting of uv data points in aperture synthesis.

It is possible to go further in analogy between interferometry and synthesis of rotation measure. One can realize that similarly as in the uv-plane, the data points along λ^2 axis are spaced non-uniformly. This is because the modern correlators provide equally spaced channels in frequency, not in wavelength. Thus we can set again analogically to the interferometry (Briggs et al. 1999):

$$D_j(\lambda_j^2) = \frac{1}{N_s(\lambda_j^2)} \qquad \text{(B.3)}$$

obtaining in this way an equivalent of uniform weighting. In the above equation N_s describes a number of data points around a given channel within an interval of width s, which can be chosen arbitrarily.

And finally, we are left with the tapering function $T_j(\lambda_j^2)$. Its application to rotation measure synthesis was already investigated by Heald et al. (2009). They used to their data a Gaussian tapering with $\sigma = \frac{1}{2}(\lambda_{max}^2 - \lambda_{min}^2)$. For the sake of simplicity, in all the further calculations I assumed $T_j(\lambda_j^2) = 1$. Below I present simulations of the observations with the new weighting strategy.

B.2   Simulations

In order to test the new concept, I performed simple simulations of observations with the natural and the uniform weighting in the λ^2 domain.

B.2.1   A natural weighting

In the simulations, I modelled three the following sources in the Faraday depth domain[1] (see, Fig. B.4): a pointlike source located at Faraday depth of -10 rad m^{-2} with flux of 10 Jy, a source extending from +30 to +50 rad m^{-2} with total flux of 40 Jy, and a source extending from +90 to +100 rad m^{-2} with the total flux of 30 Jy. These three sources (in the Faraday depth domain) are seen as a single pointlike source in the sky plane.

For these sources, I simulated the spectro-polarimetric observations with the frequency setup similar to that used in the WSRT-SINGS survey (see, Heald et al. 2009). Thus, I obtained two frequency bands (18 cm and 22 cm) with 512 frequency channels each. To simulate some diversity in quality of the data channels (caused e.g. by RFI), I increased noise levels in some

---

[1]Properties of the sources are exactly the same as in the Appendix B of Brentjens & de Bruyn (2005).
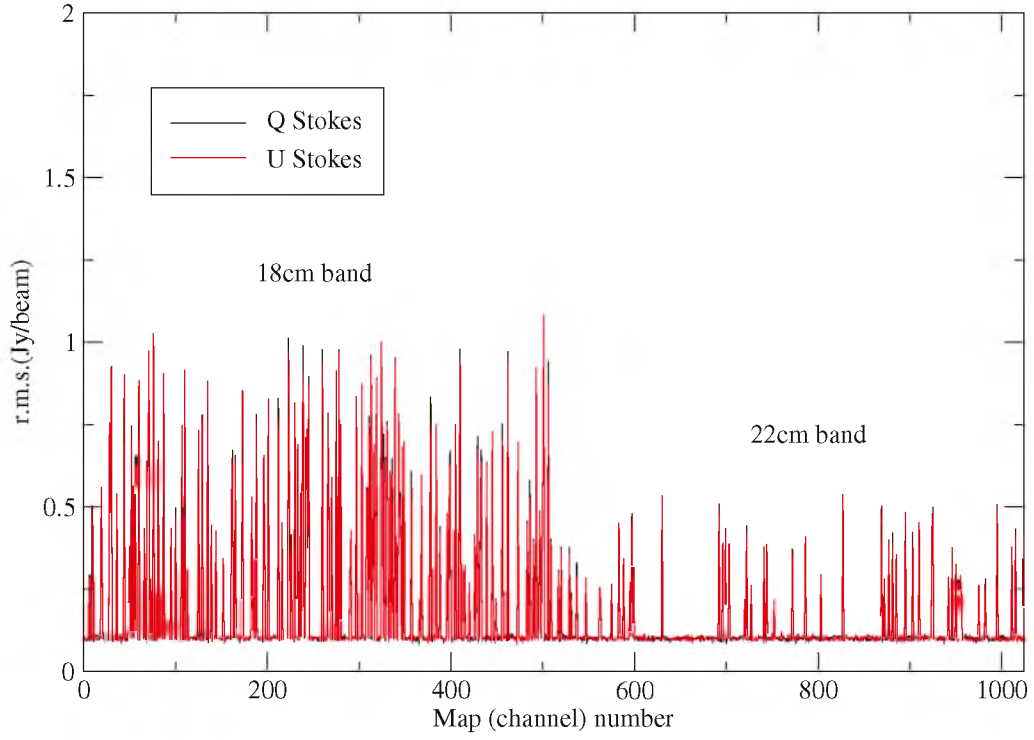
Figure B.1: R.m.s. noise levels measured in an off-source polygon region versus frequency channel (map) number for Q and U Stokes parameters. The measurements were performed for the simulated data.
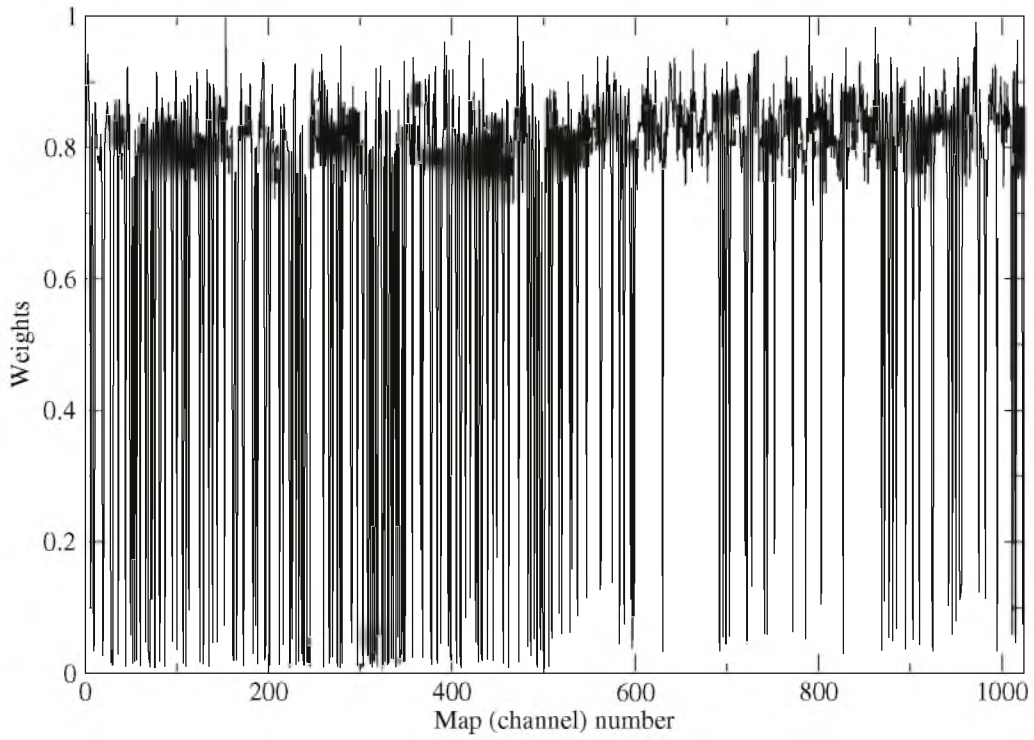

Figure B.2: Weights computed for the simulated data according to formulas B.1 and B.2 assuming $T_j = D_j = 1$ versus frequency channel (map) numbers.
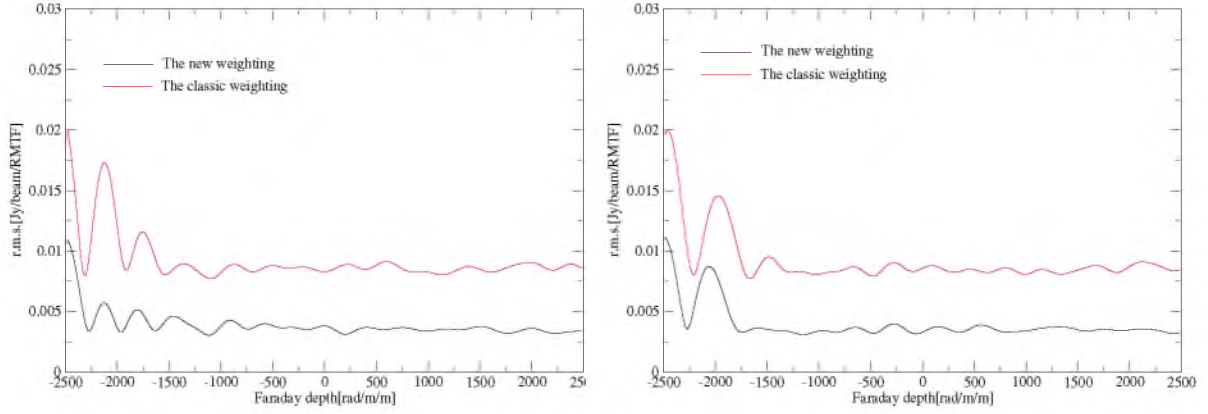
Figure B.3: R.m.s. noise levels for real (left) and imaginary (right) parts of the Faraday dispersion function. The measurements were performed in the same region as for the maps in the frequency domain.

of them. In particular, I increased noise from 2 to 10 times (randomly set) the standard value of 0.1 Jy/beam in 30% of the randomly chosen maps of the 18 cm band. Similarly, in the second band (22 cm) a 10% of maps have 2 to 5 times higher r.m.s. values. For the data cubes simulated in this way (R.A., Dec., frequency), the noise levels were measured in the off-source region and regarded as representative for the entire channel maps (Fig. B.1). From these measurements, the channel weights were computed according to the formulas B.1 and B.2, assuming $T_j = D_j$ = 1 (Fig. B.2). For the data and weights so prepared, RM Synthesis was performed using the software written by the author.

I measured noise levels in the real and imaginary parts of the obtained Faraday dispersion function (R.A., Dec., Faraday depth data cubes, Fig. B.3). A comparison of these results with the analogical results calculated with classic $(0 - 1)$ weighting shows that the r.m.s. values in the new approach are systematically lower. At the same time, the Faraday spectra obtained for the simulated sources (Fig. B.4) remain approximately the same for both the weightings (as expected). This implies that the net result of applying the new weighting is an increase of the signal-to-noise ratio. For these particular simulated data, the increase is about 2 times (the r.m.s. value is 2 times lower). Note that some small differences to be seen in the presented Faraday spectrum are due to the slightly different shapes of RMTFs obtained with both the weightings (Fig. B.5). In fact, one would expect a wider main lobe of the RMTF calculated with the new approach, similarly as for radio interferometry. This side effect is not visible for this particular setup, while quite distinct in the case of the real data shown below (Sec. B.3). A similar approach to the data weighting as that presented here was independently considered by Heald (2008) but few details were provided there.

B.2.2   A uniform weighting

In order to further explore an application of radio interferometric weighting to the RM Synthesis, I also simulated the case of the uniform weighting scheme. For simulations presented here, the same setup as above was used. For simplicity's sake, an assumption was made that all the data channels have exactly the same quality. The weights in this section were computed according to the formulas B.1 and B.3 taking $R_j = T_j = 1$ (Fig. B.6). In the simulations, I chose arbitrarily a cell size (s) in which data points were counted of about 1.17×10^{-3} m^2.

Like in radio interferometry, one could expect that with an application of the uniform
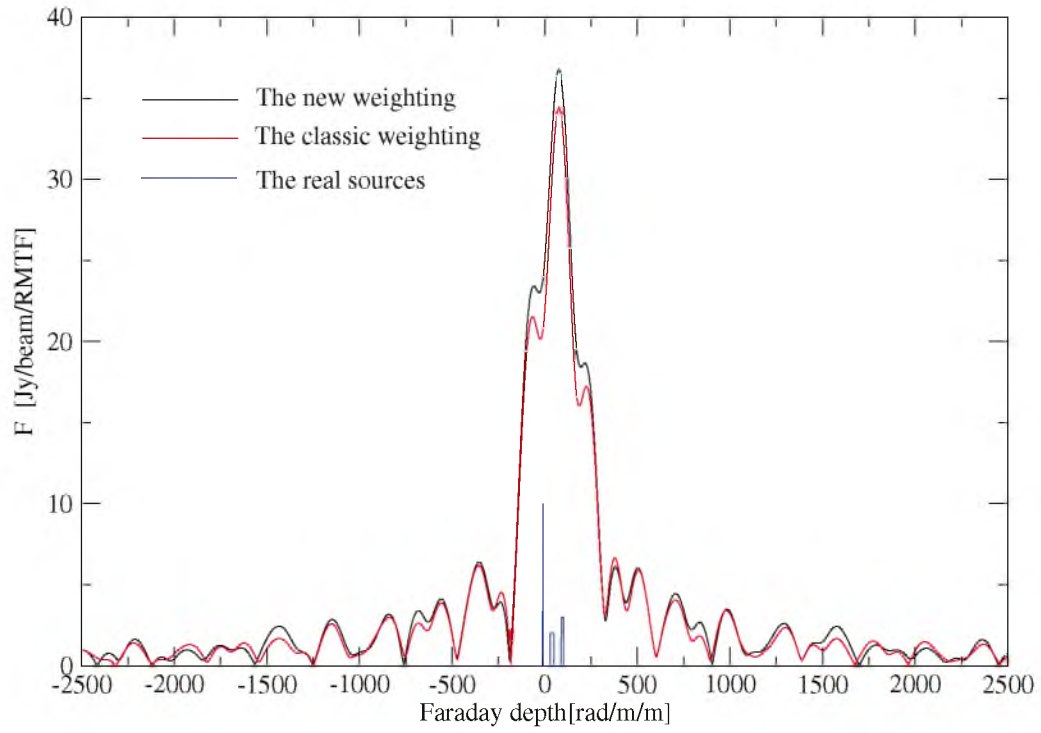
Figure B.4: Faraday spectra obtained with the new (black) and the classic weighting (red) for the given sources (blue).
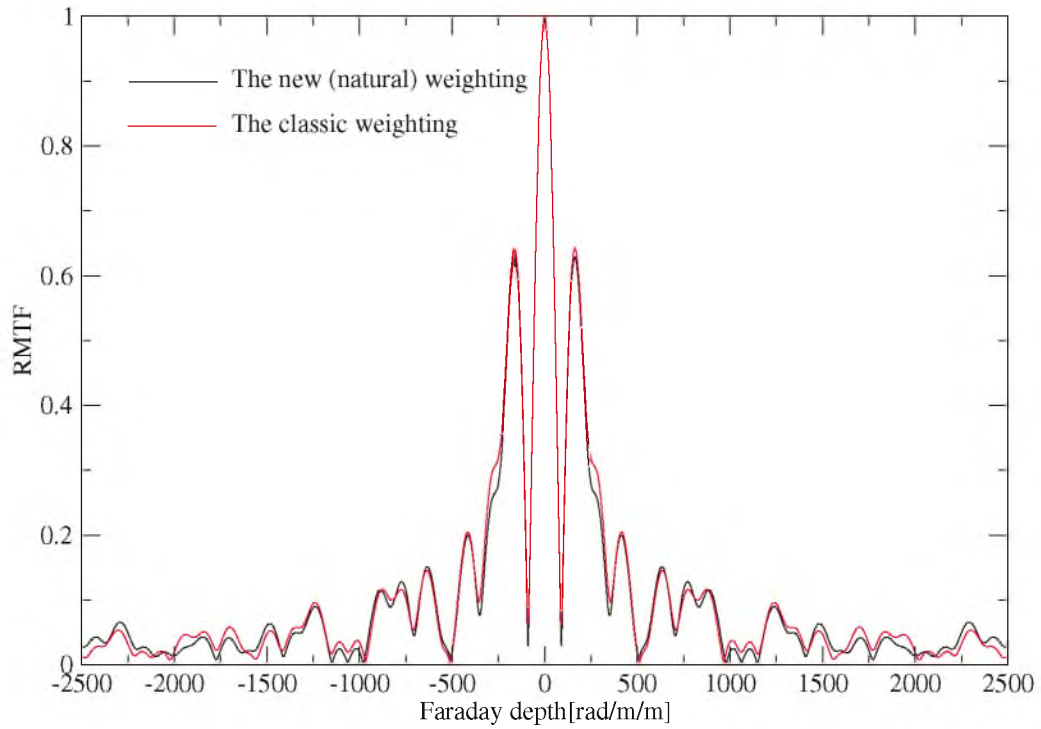

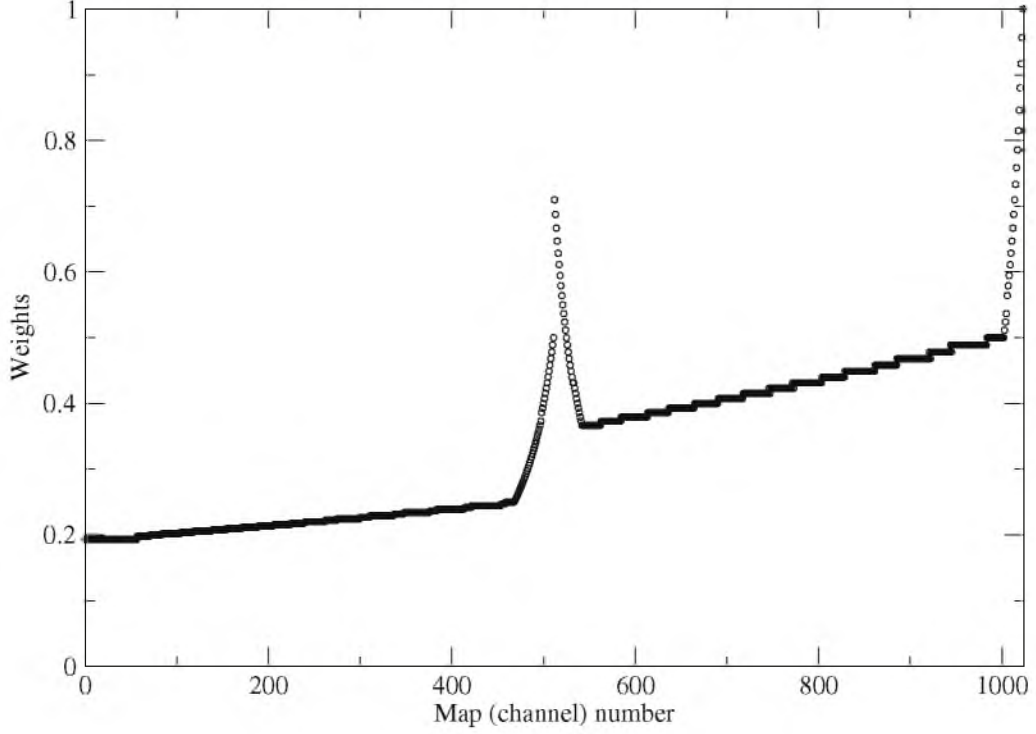Figure B.5: RMTF for the new (natural) and the classic weighting.

Figure B.6: Weights computed for the simulated data according to the formulas B.1 and B.3 assuming $R_j = T_j = 1$ versus frequency channel (map) numbers. Note that the high weights on the boundaries of spectral bands are due a smaller total density of the data points in these regions.

weighting the best resolution will be obtained. Figure B.7, presenting the uniformly and the classically weighted RMTFs shows that this is not true. Actually, there is no noticeable difference in the obtained beams. The same applies to the r.m.s. noise values measured for the real and imaginary parts of the Faraday dispersion function. Likely this is due to the fact that in the λ^2 domain, as opposed to the uv-plane, there is not so pronounced a difference in the local density of measurements.

B.3   Application of the new weighting scheme to the real data

In order to show how the proposed new weighting scheme in RM Synthesis works in practice, I re-analysed WSRT-SINGS data for galaxy NGC 2976. For comparison purposes, the dataset was processed in two ways. In the first approach the classic weighting was applied with values 0 and 1. The second approach was based on the natural weighting (see above). Before applying RM Synthesis, the data for this galaxy were re-imaged and convolved to a resolution of about 45" (see, Sec. 2.3.5 and Appendix A for a detailed description).

In figure B.8, the r.m.s. noise levels measured for particular Q and U Stokes parameters channel maps are presented. They were computed in a polygon area which was free of polarized emission and as close as possible to the phase centre. The latter criterion is important to minimize influence of a primary beam's attenuation (which is frequency-dependent) on the obtained noise measurements. As it can be seen, the noise level of 18 cm frequency band is about 2 times higher than that of 22 cm band. Moreover, some channels in both bands have a noise level much higher than the average (for the particular band). This shows the need for correcting
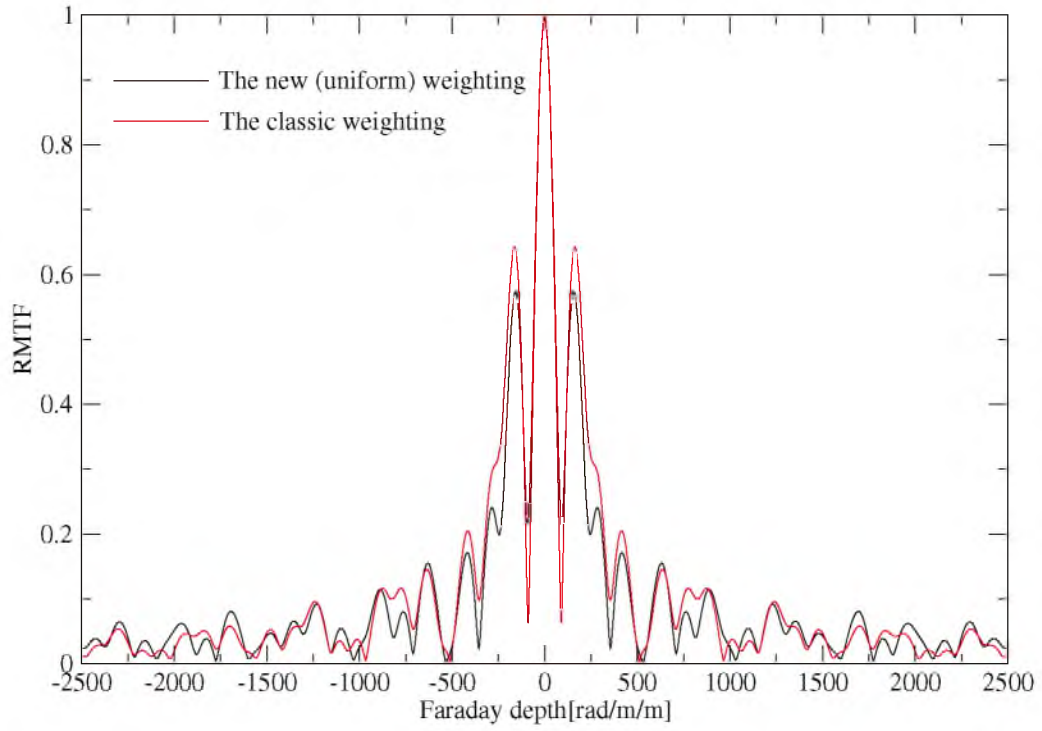
100

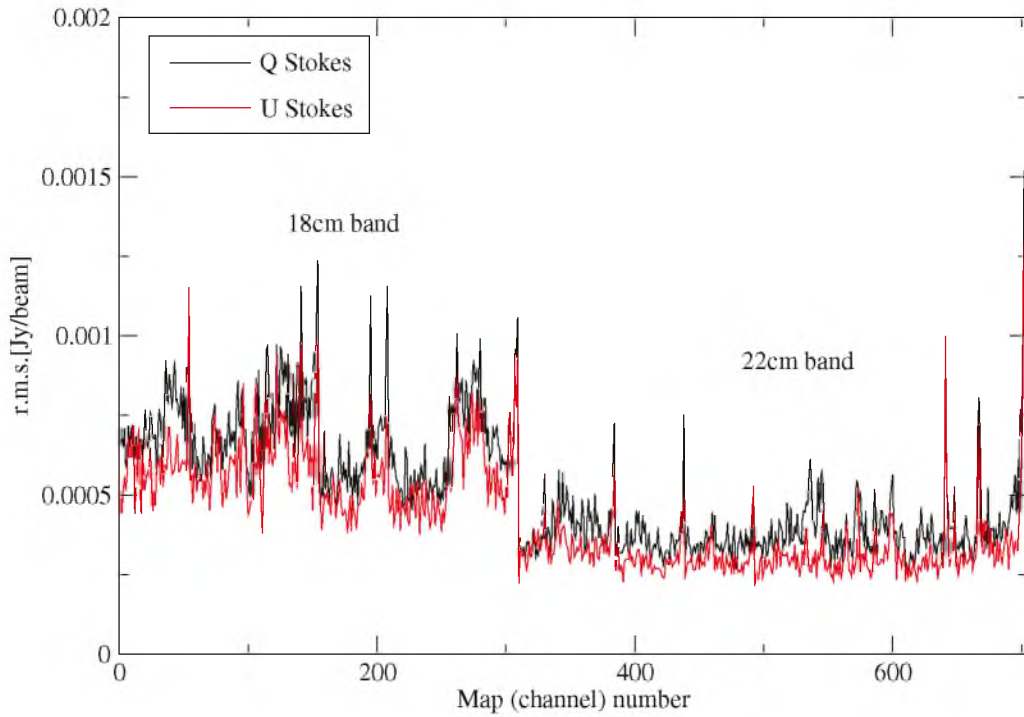Figure B.7: RMTF for the new (uniform) and the classic weighting.

Figure B.8: R.m.s. measured in an off-source polygon region versus frequency channel (map) number for Q and U Stokes parameters. The measurements were performed for NGC 2976 WSRT-SINGS data.
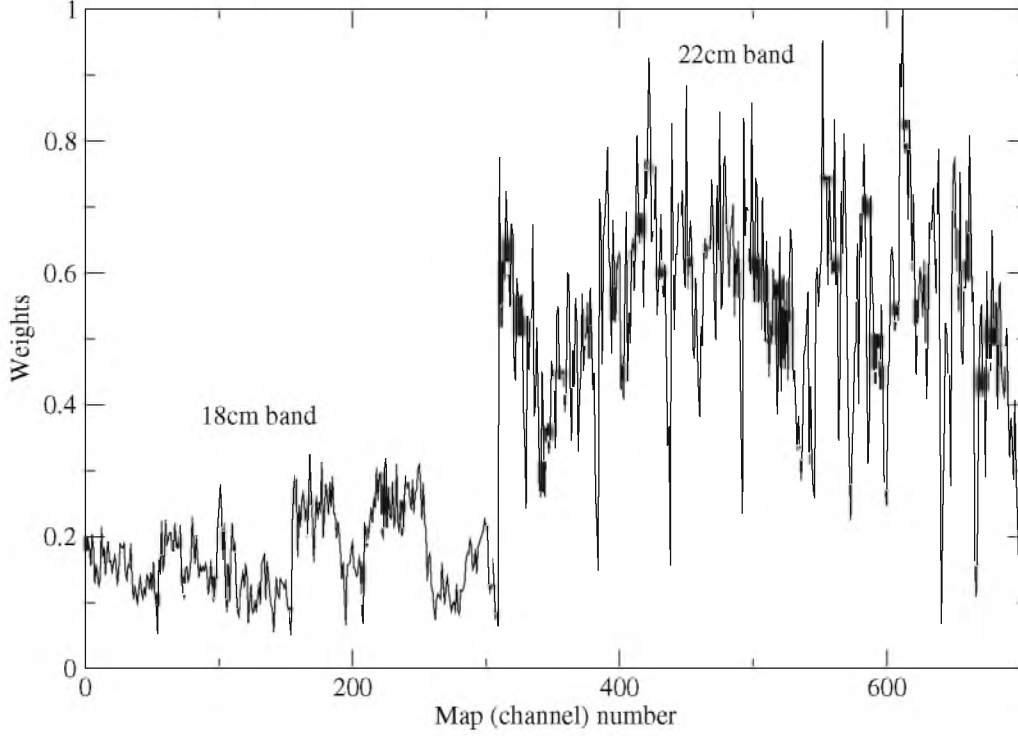
Figure B.9: Weights computed according to formulas B.1 and B.2 assuming $T_j = D_j = 1$ versus map (channel) numbers.

this effect in order to obtain the highest possible sensitivity for the Faraday dispersion function.

Having measured the noise levels, it was possible to calculate the weights according to the formulas B.1 and B.2 (Fig. B.9). It is worth to note that in 18 cm band the weights are very low when compared to the 22 cm band. In the next step, RM Synthesis was performed including the weights obtained. The results of applying the new weighting scheme and the classic one are compared in figures B.10 and B.11, where distributions of polarized emission and B-vectors are shown. In figure B.10, the contour levels (the same for both the images) were drawn for the r.m.s. measured for the classically calculated PI map. As it can be seen, there are less artifacts in the map obtained using the new weighting strategy. In fact, the noise level measured for this map is about 25μJy/beam, while for the map obtained in the classic way, it is about 30μJy/beam. Thus, due to taking into account the appropriate weights for each frequency channel, it was possible to reduce noise level in the resulting PI map by about 20%. In figure B.11, the same polarized intensity maps as in figure B.10 are shown but this time the contours are drawn at the noise level (of 25 μJy/beam) appropriate for the polarized intensity map obtained using the new weighting. By comparing both images, right and left one, it can be noticed that some previously unseen structures in PI have been revealed with the new method.

B.4   Strong and weak points of the new weighting scheme

Increasing sensitivity of the Faraday dispersion function is the main advantage of the new weighting scheme. In this method, the best quality channels have the highest weights while the poorest ones are underweighted. It can be easily understood by recalling the fact that the rotation measure synthesis is based on the Fourier transform, which in turn uses sine and cosine functions for a signal's sampling. The energy contained in these functions is infinite, because
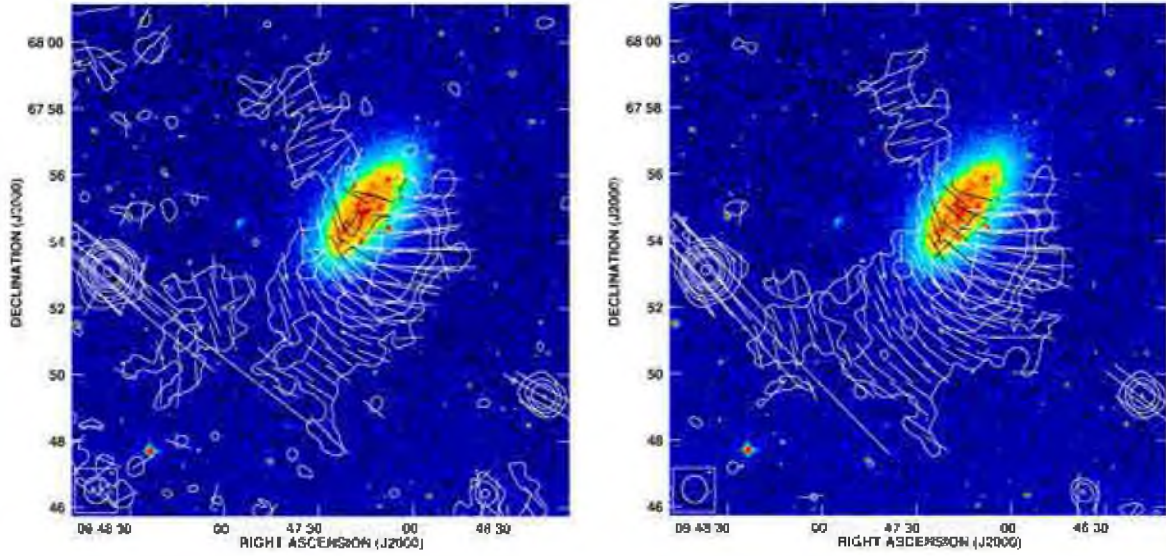
Figure B.10: Left: Polarized intensity contours and B-vectors (obtained with the classic weighting) for NGC 2976 (WSRT-SINGS data) overlaid onto the DSS blue image. Right: Polarized intensity contours and B-vectors (obtained with the new weighting) for NGC 2976 (WSRT-SINGS data) overlaid onto the DSS blue image. For both the images contours levels are: (3, 5, 8, 16, 24, 32, 64, 128) $\times$ 30μJy/beam. The beam size is 48.6" $\times$ 45.0" HPBW.

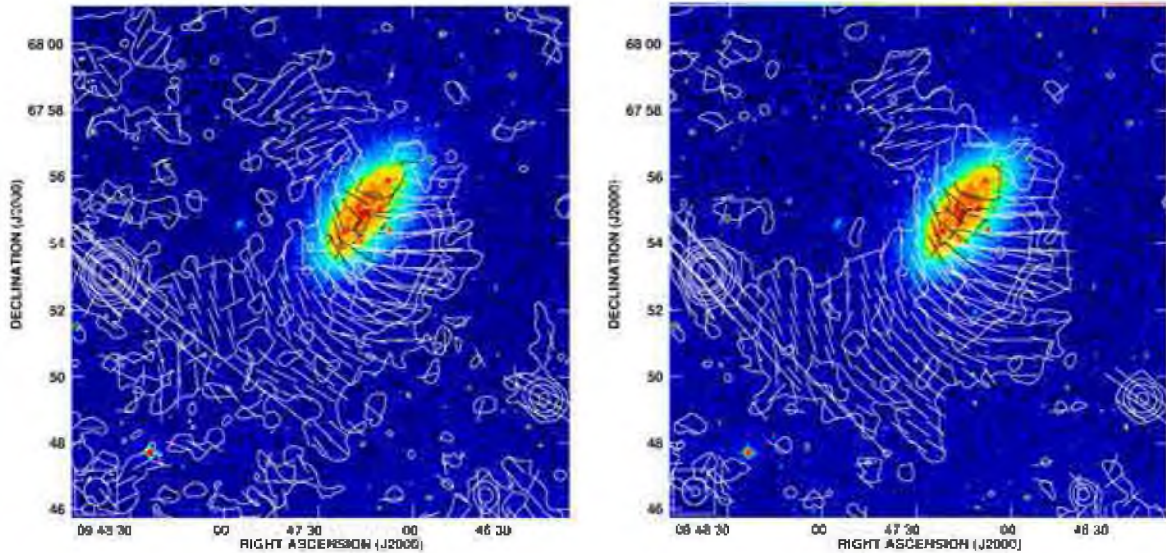Figure B.11: Left: Polarized intensity contours and B-vectors (obtained with the classic weighting) for NGC 2976 (WSRT-SINGS data) overlaid onto the DSS blue image. Right: Polarized intensity contours and B-vectors (obtained with the new weighting) for NGC 2976 (WSRT-SINGS data) overlaid onto the DSS blue image. For both the images contours levels are: (3, 5, 8, 16, 24, 32, 64, 128) $\times$ 25μJy/beam. The beam size is 48.6" $\times$ 45.0" HPBW.
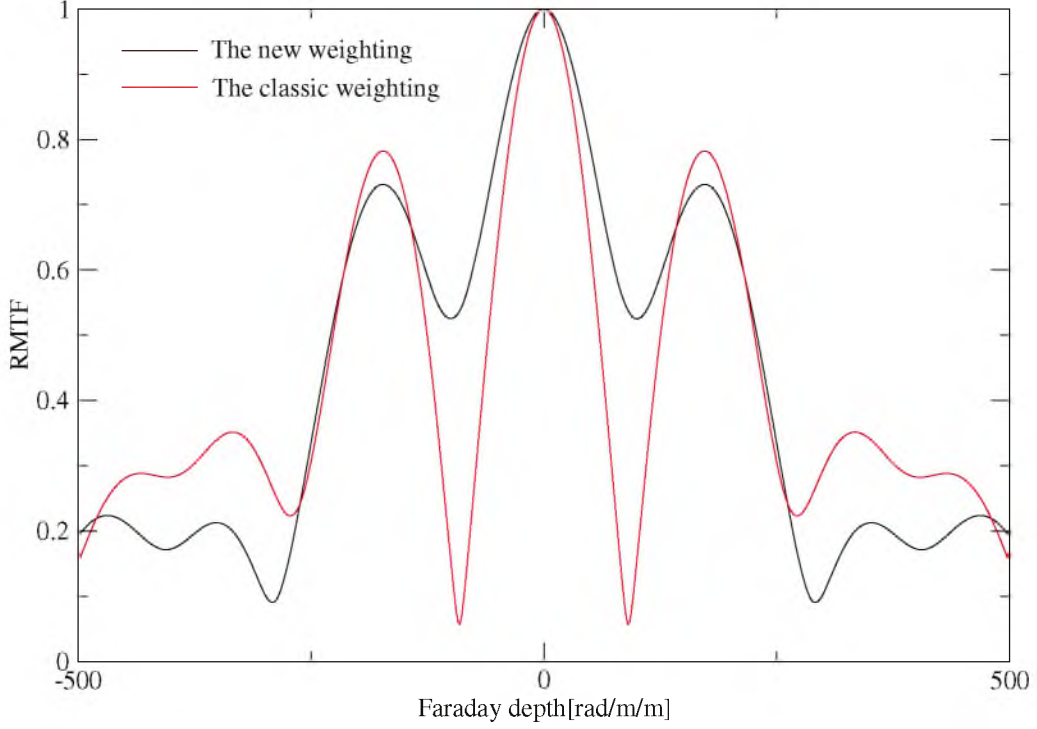
103

Figure B.12: RMTF for RM Synthesis performed for WSRT-SINGS data of NGC 2976 with the new and the classic weighting schemes.

they are not limited to any particular λ^2. Thus the channels which are less sensitive than the others will limit sensitivity of the resulting power spectrum (the Faraday dispersion function). In the case when we underweight such poor-quality channels, we will also automatically limit the contribution of the high level of noise associated with them (and usually also some imaging artifacts) to the Faraday dispersion function. I would like to note here that some factor which could contribute to the reduction of noise level in our data could be due to the fact that the particular dataset channels that were assigned higher weights (22 cm) had also a greater field of view.

Apart from sensitivity, the new weighting affects also the shape of the rotation measure transfer function. In figure B.12 both RMTFs, those obtained with the classic and the new weighting are presented. The latter shows a reduced level of side lobes (which is desirable), but at the same time the width of its main lobe is increased about 1.5 times when compared to the former one (which is not desirable). This can be accounted by the fact that in applying the new weighting, the long λ^2 were overweighted as compared to the shorter ones.

It is also worth to note that the directions of B-vectors on images (Fig. B.10, B.11) obtained with both methods differ by some small amount. This is due the fact that the mean weighted λ^2 for which directions of B-vectors are computed is not the same in both approaches.

Summarizing, in this appendix it was shown that the simple method of minimizing of effects of differing sensitivities across frequency channels (or spectral bands) results in a considerable (about 20% for the NGC 2976 from WSRT-SINGS dataset) increase of sensitivity of the Faraday dispersion function. The new weighting can also help to improve the shape of RMTF, which is of fundamental importance for the RM Synthesis experiments.

Bibliography

Andrecut, M. 2013, MNRAS, 430, 15

Andrecut, M., Stil, J.M. & Taylor, A.R. 2012, AJ, 143, 33

Appleton, P.N., Davies, R.D. & Stephenson, R.J. 1981, MNRAS, 195, 327

Appleton, P.N. & van der Hulst, J.M. 1988, MNRAS, 234, 957

Arshakian, T. G., Beck, R., Krause, M. & Sokoloff, D. 2009, A&A, 494, 21

Bartel, N., Bietenholz, M.F. & Rupen, M.P. 1995, Proc. Natl. Acad. Sci. USA, 92, 11374

Bartel, N., Bietenholz, M.F., Rupen, M.P., et al. 2000, Science, 287, 112

Bartel, N., Bietenholz, M.F., Rupen, M.P., et al. 2002, ApJ, 581, 404

Beck, R., Krause, M. & Klein, U. 1985, A&A, 152, 237

Beck, R., Brandenburg, A., Moss, D., Shukurov, A. & Sokoloff, D. 1996, ARA&A, 34, 155

Beck, R. 2005, in: Cosmic Magnetic Fields, Lecture Notes in Physics (Berlin: Springer), R. Wielebinski & R. Beck (eds.), 664, 41

Beck, R., & Krause, M. 2005, AN, 326, 414

Beck, R. 2007, A&A, 470, 539

Beck, R. 2009, Ap&SS, 320, 77

Beck, R., Frick, P., Stepanov, R. & Sokoloff, D. 2012, A&A, 543, 113

Beck, R. & Wielebinski, R. 2013, in Planets, Stars and Stellar Systems Vol. 5, eds. D.T. Oswalt, G. Gilmore, Springer, Dordrecht, 2013, p.641

Brandenburg, A., Donner, K.J., Moss, D., et al. 1993, A&A, 271, 36

Brandenburg, A. & Subramanian, K. 2005, PhysRev, 417, 1

Braun, R., Heald, G., & Beck, R. 2010, A&A, 514, 42

Brentjens, M.A., de Bruyn, A.G. 2005, A&A, 441, 1217

Brentjens, M.A. 2008, A&A, 489, 69

Briggs, D.S. 1995, High Fidelity Deconvolution of Moderately Resolved Sources, Ph.D. Thesis,

Briggs, D.S., Schwab, F.R. & Sramek, R.A. 1999, in: Synthesis Imaging in Radio Astronomy II ASP Conference Series, G.B. Taylor, C.L. Carilli & R.A. Perley (eds.), 180, 127

Bronkalla, W., Notni, P. & Mutter, A.A.-R. 1992, AN, 313, 1

Bureau, M. & Carignan, C. 2002, AJ, 123, 1316

Calzetti, D., Kennicutt, R. C., Engelbracht, C. W., et al. 2007, ApJ, 666, 870

Chynoweth, K.M., Langston, G.I., Yun, M.S., et al. 2008, AJ, 135, 1983

Chynoweth, K.M., Langston, G.I., Holley-Bockelmann, K. & Lockman, F.J. 2009, AJ, 138, 287

Chyży, K.T., Beck, R., Kohle, S., Klein, U., & Urbanik, M. 2000, A&A, 355, 128

Chyży, K.T., Knapik, J., Bomans, D. J., et al. 2003, A&A, 405, 513

Chyży, K. T., & Beck, R. 2004, A&A, 417, 541

Chyży, K.T., Bomans, D.J., Krause, M., et al. 2007a, A&A, 462, 933

Chyży, K.T., Ehle, M., & Beck, R. 2007b, A&A, 474, 415

Chyży, K.T. 2008, A&A, 482, 755

Chyy, K.T. & Buta, R.J. 2008, ApJ, 677, L17

Chyży, K. T., Weżgowiec,M., Beck, R., & Bomans, D. 2011, A&A, 529, A94

Condon, J.J. 1987, ApJS, 65, 485

Dale, D.A., Cohen, S.A., Johnson, L.C., et al. 2009, ApJ, 703, 517

de Blok, W.J.G, Walter, F., Brinks, E., et al. 2008, AJ, 136, 2648

de Bruyn, A.G. & Brentjens, M.A. 2005, A&A, 441, 931

De Vaucouleurs, G., De Vaucouleurs, A., Corwin JR., et al. 1991, Third Reference Catalogue Of Bright Galaxies, Version 3.9

Drzazga, R.T., Chyży, K.T., Jurusik, W. & Wiórkiewicz, K. 2011, A&A, 533, 22

de Vaucouleurs, G., de Vaucouleurs, A., Corwin, H. G., Jr., et al. 1991, Third Reference Catalogue of Bright Galaxies (RC3)

Dumke, M., Krause, M., Wielebinski, R. & Klein, U. 1995, A&A, 302, 691

Elstner, D. 2005, in The Magnetized Plasma in Galaxy Evolution, ed. Chyży, Kraków, p.117

Emerson, D.T. & Gräve, R. 1988, A&A, 190, 353

Ferriére, K. & Terral, P. 2014, A&A, 561, 100

Frick, P., Sokoloff, D., Stepanov, R. & Beck, R. 2010, MNRAS, 401, 24

Gaensler, B. M., Haverkorn, M., Staveley-Smith, L., et al. 2005, Sci, 307, 1610

Gallagher, J.S. & Matthews L.D. 2002, in: Modes of star formation, ASP Conf. 285, p.303

Gil de Paz, A., Madore, B.F. & Pevunova, O. 2003, ApJS, 147, 29

Gioia, I. M., Gregorini, L., & Klein, U. 1982, A&A, 116, 164

Gregory, P.C. & Condon, J.J. 1991, ApJS, 75, 1011

Gressel, O., Elstner, D., Ziegler, U., Rudiger, G. 2008, A&A, 486L, 35

Hanasz, M., Wóltański, D. & Kowalik, K. 2009, ApJ, 706, L155

Haslam, C.G.T. 1974, A&AS, 15, 333

Heesen, V., Beck, R., Krause, M. & Dettmar, R.J. 2009, A&A, 494, 563

Heesen, V., Rau, U., Rupen, M.P., Brinks, E. & Hunter, D.A. 2011, ApJ, 739, L23

Heald, G. 2008, in: Cosmic Magnetic Fields: From Planets, to Stars and Galaxies, Proceedings IAU Symposium No. 259, ed. K.G. Strassmeier, A.G. Kosovichev & J.E. Beckman, p.591

Heald, G., Braun, R. & Edmonds, R. 2009, A&A, 503, 409

Ho, L.C., Filippenko, A.V. & Sargent, W.L.W. 1997, ApJS, 112, 315

Hoopes, Ch.G., Walterbos, R.A.M., Bothun, G.D. 2001, ApJ, 559, 878

Hunter, D.A., Ficut-Vicas, D. Ashley, T., et al. 2012, ApJ, 144, 134

Jurusik, W., Drzazga, R.T., Jabłeka, M., et al. 2014, A&A, 567, 134

Karachentsev, I.D., Dolphin, A.E., Geisler, D., et al. 2002, A&A, 383, 125

Karachentsev, I.D. 2005, AJ, 129, 178

Karachentsev, I.D. & Kaisin, S.S. 2007, AJ, 133, 1883

Kaufman, M., Bash, F.N., Kennicutt, Jr.R.C. & Hodge, P.W. 1987, ApJ, 319, 61

Kaufman, M., Bash, F.N., Crane, P.C. & Jacoby, G.H. 1996, AJ, 112, 1021

Kennicutt, Jr.R.C., Armus, L., Bendo, G., et al. 2003, PASP, 115, 928

Kennicutt, R. C., Lee, J. C.,Funes, S. J. et al. 2008, Apj, 178, 247

Kennicutt, R.C. & Evans, N.J. 2012, ARA&A, 50, 531

Kepley, A. A., Mühle, S., Everett, J., et al. 2010, ApJ, 712, 536

Kepley, A. A., Zweibel, E.G., Wilcots, E.M., Johnson, K.E. & Robishaw, T. 2011, ApJ, 736, 139

Kim, W.-T., Ostriker, E.C. & Stone, J.M. 2002, ApJ, 581, 1080

Knapen, J. H., de Jong, R. S., Stedman, S., & Bramich, D.M. 2003, MNRAS, 344, 527

Knapen, J. H., Stedman, S., Bramich, D.M., Folkes, S. F., & Bradley, T. R. 2004, A&A, 426, 1135

Knapik, J., Soida, M., Dettmar, R.-J., Beck, R. & Urbanik, M. 2000, A&A, 362, 910

Krause, M., Hummel, E. & Beck, R. 1989a, A&A, 217, 4

Krause, M., Beck, R. & Hummel, E. 1989b, A&A, 217, 17

Kronberg, P.P., Lesch, H., & Hopp, U. 1999, ApJ, 511, 56

Kulpa-Dybeł, K., Otmianowska-Mazur, K., Kulesza-Żydzik, B., et al. 2011, ApJ, 733, L18

Li, F., Brown, S., Cornwell, T.J. & de Hoog, F. 2011, A&A, 531, 126

Lozinskaya, T.A. & Moiseev, A.V. 2007, MNRAS, 381, 26

Johnston-Hollitt, M., Hollitt, C. P., & Ekers, R. D. 2004, The Magnetized Interstellar Medium, ed. B. Uyaniker et al. (Katlenburg: Copernicus), 13

Mao, S. A., Gaensler, B. M., Stanimirović, S. et al. 2008, ApJ, 688, 1029

Mao, S.A., McClure-Griffiths, N.M., Gaensler, B.M., et al. 2012, ApJ, 759, 25

Marti-Vidal, I., Marcaide, J.M., Alberdi, A., et al. 2011a, A&A, 526, 143

Marti-Vidal, I., Marcaide, J.M., Alberdi, A., et al. 2011b, A&A, 533, 111

Massey, P. & Holmes, S. 2002, ApJ, 580, L35

Mateo, M. 1998, ARA&A, 36, 435

Matthews, L.D. & van Driel, W. 2000, A&ASS, 143, 421

Morsi, H. W., & Reich, W. 1986, A&A, 163, 313

Moss, D., Brandenburg, A., Donner, K.J. & Thomasson, M. 1993, ApJ, 409, 179

Moss, D., Sokoloff, D., Beck, R. & Krause, M. 2010, A&A, 512, 61

Murphy, E.J., Kenney, J.D.P., Helou, G., Chung, A., & Howell, J.H. 2009, ApJ, 694, 1435

Neronov, A. & Semikoz, D. V. 2009, arXiv:0910.1920

Nidever, D.L., Ashley, T., Slater, C.T., et al. 2013, ApJ, 779, 15

Niklas, S. 1995, PhD thesis, University of Bonn

Niklas, S., Klein, U., Braine, J., Wielebinski, R. 1995, A&AS, 114, 21

Niklas, S., Klein, U. & Wielebinski, R. 1997, 322, 19

Nikiel-Wroczyński, B., M. Soida, M., Urbanik, M., et al. 2013a, MNRAS, 435, 149

Nikiel-Wroczyński, B., M. Soida, M., Urbanik, M., et al. 2013b, A&A, 553, 4

Offringa, A.R., de Bruyn, A.G., Biehl, M., et al. 2010, MNRAS, 405, 155

Offringa, A.R., van de Gronde, J.J. & Roerdink, J.B.T.M. 2012, A&A, 539, 95

Otmianowska-Mazur, K. & Vollmer, B. 2003, A&A, 402, 879

Parker, E.N. 2007, Conversations on Electr. and Magn. Fields in the Cosmos, Princeton Univ. Press

Perley, R.A. & Butler, B.J. 2013, ApJS, 204, 19

Pisano, D.J., Wilcots, E.M. & Elmegreen, B.G. 2000, AJ, 120, 763

Pizzo, R.F., de Bruyn, A.G., Bernardi, G. & Brentjens, M.A. 2011, A&A, 525, 104

Rau, U. & Cornwell, T.J. 2011, A&A, 532, 71

Richer, M.G., Bullejos, A. Borissova, J., et al. 2001, A&A, 370, 34

Ripero, J., Garcia, F. Rodriguez, D. et al. 1993, IAU Circ, 5731,

Sanna, N., Bono, G., Stetson, P.B. et al. 2008, ApJ, 688, L69

Sault R.J., Teuben P.J. & Wright M.C.H. 1995 in Astronomical Data Analysis Software and Systems IV, ed. R. Shaw, H.E. Payne, J.J.E. Hayes, ASP Conference Series, 77, 433

Segalovitz, A., Shane, W.W. & de Bruyn, A.G. 1976, Nature, 264, 222

Shukurov, A. 2004, arXiv:astro-ph/0411739v1

Shukurov, A. 2005, Lect. Notes Phys., 664, 113

Shukurov, A. 2007, in Mathematical Aspects of NaturalDynamos, ed. E.Dormy & A. M. Soward (Boca Raton, FL: CRC Press), 313

Siejkowski, H. 2012 PhD thesis, Jagiellonian University, Kraków

Simon, J.D., Bolatto, A.D., Leroy, A. & Blitz, L. 2003, ApJ, 596, 957

Sokoloff, D.D., Bykov, A.A., Shukurov, A., et al. 1998, MNRAS, 299, 189

Soida, M., Beck, R., Urbanik, M. & Braine, J. 2002, A&A, 394, 47

Soida, M., Otmianowska-Mazur, K., Chyży, K.T., Vollmer, B. 2006, A&A, 458, 727

Soida, M., Krause, M., Dettmar, R.J. & Urbanik, M. 2011, A&A, 531, 127

Spekkens, K. & Sellwood, J.A. 2007, ApJ, 664, 204

Stanimirović, S. 2002, in Single-Dish Radio Astronomy Techniques and Applications, ed. Stanimirović et al., 278

Stil, J.M. & Israel, F.P. 2002a, A&A, 389, 29

Stil, J.M. & Israel, F.P. 2002b, A&A, 389, 42

Thilker, D.A., Bianchi, L., Meurer, G., et al. 2007, ApJS, 173, 538

Tüllmann R., Dettmar, R.-J., Soida, M., Urbanik, M. & Rossa, J. 2000, A&A, 364, L36

Veilleux, S., Cecil, G. & Bland-Hawthorn, J. 2005, ARA&A, 43, 769

Vollmer, B., Beck, R., Kenney, J.D.P., van Gorkom, J.H. 2004, AJ, 127, 3375

Vollmer, B., Soida, M., Chung, A., et al. 2008, A&A, 483, 89

Vollmer, B., Soida, M., Chung, A., et al. 2010, A&A, 512, 36

Vollmer, B., Soida, M., Beck, R., et al. 2013, A&A, 553, 116

Walter, F. Brinks, E., de Blok, W.J.G., et al. 2008, AJ, 136, 2563

Weiler, K.W., Williams, Ch.L., Panagia, N., et al. 2007, ApJ, 671, 1959

Widrow, L. M. 2002, Rev. of Mod. Phys., 74, 775

Wilcots, E.M. & Miller, B.W. 1998, AJ, 116, 2363

Williams, B.F., Dalcanton, J.J, Stilp, A., et al. 2010, ApJ, 709, 135

Yang, H. & Skillman, E.D. 1993, AJ, 106, 1448

Yun, M.S., Ho, P.T.P. & Lo, K.Y. 1994, Nature, 372, 530

Zeldovich, Ya.B., Ruzmaikin, A.A. & Sokoloff, D.D. 1990, The Almighty Chance, Singapore, World Sci.